

# Transforming Diagnosis through Advanced Machine Learning and Data Analytics

Qingyuan Liu<sup>1</sup>

<sup>1</sup>Department of Computing, The Hong Kong Polytechnic University, Hong Kong SAR, China

## Abstract

Fragmented hospital silos and strict privacy rules often leave medical AI models staring at small, uneven, mismatched tabular cohorts, so models trained directly on those data tend to wobble when moved between sites. Here we sketch *PANDA* (Pretrained Adaptation Network with Domain Alignment)—a cross-hospital setup that leans on a pre-trained tabular foundation model, keeps the feature budget lean, and folds in unsupervised domain adaptation, even if calling it a framework is arguably generous. *PANDA* uses a TabPFN-style Transformer encoder meta-trained on millions of synthetic tables; that pretraining appears to capture higher-order interactions that tuned gradient-boosting ensembles often miss when samples are scarce. A cross-cohort RFE step uses the foundation model to identify eight biomarkers that stay predictive across both hospitals, cutting data-collection demands and stabilizing interpretation. To ease distribution gaps, we add TCA to the training loop so source and target cohorts land in a shared latent space. This mix-foundation-model representations, RFE-filtered features, and TCA—seems to reduce covariate shift and keep those eight variables useful even when each site ranks them differently. On two lung-nodule cohorts (295 training, 190 external), *PANDA* lifts AUC and sensitivity over supervised and non-adaptive baselines, hinting that pairing foundation-model priors with statistical alignment may improve generalization in small, cross-domain medical tasks.

INSERT\_TOC\_HERE

# 1 Introduction

Early and accurate prediction of pulmonary nodule malignancy remains central to lung cancer screening, yet decision support tools routinely fail once they leave the academic centers in which they were developed. Classical risk scores such as the Mayo Clinic, Veterans Affairs, Brock (PanCan), PKUPH, and Li models achieve internal AUCs of 0.80–0.94 by fitting logistic regressions to carefully curated cohorts, but their performance often falls to 0.60–0.75 when applied to community-screening sites, Asian hospitals, or solitary-nodule subgroups [1, 2, 3, 4, 5, 6, 7]. Meta-analyses covering more than 80,000 nodules indicate that prevalence shifts, acquisition protocol differences, and distinct background diseases (e.g., tuberculosis versus granulomas) distort learned decision boundaries and render non-adaptive risk calculators unreliable in cross-hospital practice.

In response, the medical AI community has assembled an ecosystem of algorithms that mirrors the broader evolution of structured-data learning. Gradient-boosted decision trees, led by XG-Boost/LightGBM successors, dominate many tabular benchmarks because they tolerate heterogeneous feature scales and missing values and continue to anchor registries such as NLST [8, 9]. Radiomics pipelines engineer thousands of texture descriptors from CT volumes to capture subtle morphologic cues, but their scanner sensitivity and need for harmonization often negate cross-site gains [5, 10]. Neural “deep tabular” architectures—TabNet, TabTransformer, SAINT, FT-Transformer, NODE, and a wave of attention-based variants—extend differentiability to structured data and enable multimodal fusion, yet they require large, well-calibrated cohorts and frequently lag tuned tree ensembles on clinical tabular benchmarks [11, 12, 13, 14, 9]. Foundation-style approaches push further: TabPFN employs synthetic structural-causal priors to deliver hyperparameter-free, small-sample inference; TabPFN-2.5 and drift-resilient variants relax attention bottlenecks and introduce explicit temporal priors; tabular LLMs serialize rows into prompts to borrow reasoning skills from generative models; and recent work explores re-purposing tabular foundation models for graph reasoning and multimodal prompts [15, 16, 17, 18, 19, 20, 21]. Complementary efforts investigate federated optimization and on-device continual learning so that models can absorb new hospital evidence without breaching privacy constraints [22, 23].

Despite this diversity of techniques, cross-hospital transfer remains fragile. Performance degrades because the three dominant pathologies of medical tabular data co-occur: (i) sample scarcity—most nodular cohorts contain only a few hundred labeled patients, limiting the stability of purely supervised training; (ii) distribution shift—label prevalence, scanner kernels, and demographics change the marginal  $P(X)$  and even the conditional  $P(Y | X)$  between hospitals; and (iii) feature heterogeneity—sites log disjoint biomarker panels, measurement units, and coding policies that invalidate naive feature alignment [24, 25, 26]. Domain adaptation research in imaging and wearables demonstrates that adversarial training, optimal transport, and statistical moment matching can recover some performance, but these methods are rarely specialized for structured clinical data, and benchmarks such as TableShift show that off-the-shelf algorithms still incur large out-of-distribution gaps even when in-distribution accuracy is high [22, 27, 28]. Large-scale regulators now regard shift detection and recalibration as core elements of post-market surveillance, underscoring that robustness cannot be an afterthought [24].

Tabular foundation models partially alleviate the sample-size constraint, yet they inherit a closed-world assumption: the context set used during in-context learning is assumed to reflect the same joint distribution as the query samples. When shifts in biomarkers, acquisition settings, or feature schemata emerge, even TabPFN variants can become overconfident because their attention weights are tied to the geometry of the source cohort [21, 18]. Emerging iterations such as TabPFN-2.5 and drift-resilient TabPFN extend context length and incorporate simulated Drifts into the prior, but they remain sensitive to mismatched feature spaces or unlabeled target domains without an explicit alignment step [16, 19]. Consequently, bridging the gap between high internal accuracy and safe cross-site deployment requires combining foundation models with principled unsupervised domain adaptation and feature selection that respect clinical realities.

Pulmonary nodule malignancy prediction is an archetypal stress test for these issues because every stage of the pipeline can drift. Traditional clinical scores (Mayo, VA, Brock, PKUPH, Li) and their LASSO or gradient-boosted successors were derived from carefully curated cohorts with narrow demographic profiles and fixed scanner protocols, so their coefficients silently encode source-specific prevalence, upper-lobe priors, and calcification heuristics [1, 2, 3, 4, 6]. Meta-analyses across Asian screening programs and European cancer centers show that the same score threshold yields widely varying sensitivities (50–90%) once smoking histories, granulomatous disease burdens, or acquisition

kernels change, even before accounting for the fact that benign nodules dominate community-screening cohorts [5, 7]. Radiomics pipelines and 3D CNNs attain strong internal AUCs on NLST and LIDC, yet external validations reveal double-digit declines when voxel spacing, reconstruction kernels, or ethnic mix shift, and shortcut learning can prompt models to rely on hospital-specific artifacts rather than biology [29, 30, 10]. Domain adaptation techniques drawn from imaging—adversarial discriminators, cycle-consistent transfers, and optimal transport—help when both domains share feature schemas, but they rarely address the missing-variable problem or the strict small- $N$  regime of tabular nodular cohorts [22, 28]. Even TableShift, Wild-Time, and BRFSS benchmarks illustrate that strong in-distribution accuracy does not guarantee out-of-distribution reliability and that label shift dominates error budgets unless prevalence-aware sampling or calibration is performed [27, 28].

Three recurring fault lines run through cross-hospital deployments. First, protocol heterogeneity induces covariate shift: radiology departments change reconstruction kernels, slice thicknesses, and iterative denoisers across scanner upgrades, while laboratory information systems switch assay vendors and reference ranges; even BRFSS survey wording drifts across years, warping marginal feature distributions. Second, label prevalence shifts with setting: tertiary oncology centers see far more malignant nodules than community-screening sites, and diabetes rates differ sharply across racial cohorts. Thresholds tuned to one prevalence produce over-biopsy or missed cancers elsewhere, creating safety and regulatory risk. Third, feature mismatches and missingness invalidate naive alignment: hospitals log different biomarker panels, use distinct encodings for smoking status, or drop variables entirely when tests are not ordered. Without schema-aware pruning, models overfit site-specific artifacts or fail on missing columns. These shifts accumulate over time (concept drift), so one-off calibration cannot guarantee safe operation.

The algorithmic landscape mirrors these stresses. Gradient-boosted trees cope with messy scales and missingness but require abundant data to control variance and cannot be fine-tuned across domains without rebuilding from scratch. Deep tabular models offer differentiable representations and multi-modal fusion, yet they are data hungry, sensitive to hyperparameters, and often fail when the effective sample size falls below a few thousand [9, 14]. Tabular foundation models such as TabPFN relax the data requirement through extensive pre-training and in-context learning, but they inherit closed-world assumptions: the context window expects a stable joint distribution and a consistent feature schema. When any of the three fault lines above appear, attention weights focus on non-comparable neighbors, inflating confidence while accuracy erodes [21, 18, 19].

Safety guidance now emphasizes designing for shift rather than reacting to it. Agencies and hospital governance boards increasingly demand evidence that models remain calibrated when equipment, demographics, or policies change [24]. In practice, relying on AUC alone hides threshold failures: a model can preserve rank ordering of patients yet still trigger excessive false positives after prevalence drifts. Cross-hospital nodule tools must therefore expose calibration behavior and maintain sensitivity where early intervention matters most, especially under privacy rules that preclude sharing target labels. These requirements push method design toward unsupervised alignment, feature budget discipline, and explicit handling of prevalence drift.

Taken together, the research gap is stark: tree ensembles and deep tabular networks struggle with small, heterogeneous cohorts; foundation models improve small-sample performance but assume matched domains; and generic domain adaptation rarely accounts for missing features or label drift in clinical tables. A credible solution must (i) retain sample efficiency via strong priors, (ii) discard site-specific signals that cannot transfer, and (iii) align source and target representations without target labels or schema changes.

Pulmonary nodule screening crystallizes these issues. Tuberculosis and pneumoconiosis inflate upper-lobe benign nodules in many Asian cohorts, confounding upper-lobe priors embedded in Western-derived scores; smoking histories differ by region and era; and scanner upgrades alter texture features that radiomics and 3D CNNs depend upon [5, 10, 30]. Thresholds optimized on tertiary centers with high malignancy prevalence overall cancer in community settings, triggering unnecessary biopsies. Conversely, down-tuned thresholds can miss aggressive lesions in high-risk clinics. Similar tensions arise in the BRFSS race-shift task: demographic composition, socioeconomic exposures, and survey-year wording alter the marginal distribution of risk factors, while diabetes prevalence rises from 12.5% (White) to 17.4% (non-White), so fixed operating points misfire. Any method that ignores these shifts risks brittle, non-actionable predictions.

Design constraints follow from these observations. Models must be frugal with labels, avoid depen-

dence on site-specific variables, expose calibration behavior across prevalences, and handle unlabeled target domains where privacy bars cross-site annotations. They must also degrade gracefully when partial feature overlap forces a reduced schema. These constraints shape our approach to pairing pre-trained priors with statistical alignment and minimal, stable feature sets instead of relying on brute-force training.

The broader AI trajectory for tabular healthcare data provides both ingredients and warnings. Tree ensembles remain strong baselines because they tolerate mixed scales and missingness, yet their non-differentiable nature makes them hard to adapt across sites or fuse with other modalities [8, 14]. Deep tabular models (TabNet, TabTransformer, SAINT, FT-Transformer) introduce attention and gating to structured data, but they are data hungry, hyperparameter-sensitive, and vulnerable to batch-statistic or encoding drift when hospitals differ in coding or preprocessing [11, 12, 13, 9]. Tabular foundation models promise sample efficiency via massive synthetic pre-training and in-context learning, yet they still assume aligned schemas and stable covariates; when scanners, assay panels, or demographics shift, attention can anchor on non-comparable neighbors [21, 18, 19]. Tabular large language models serialize rows into prompts and leverage general-purpose reasoning but incur heavy latency and often struggle with the precise numerical reasoning demanded by biomarkers [20]. Across these families, robustness depends less on raw capacity than on respecting feature overlap and shift.

Small-sample, high-dimensional, and imbalanced regimes further amplify brittleness. Pulmonary nodule cohorts rarely exceed a few hundred labeled patients, while radiomics or biomarker panels can contain over a hundred variables; naive inclusion of all features raises variance and encodes site-specific artifacts. Stability-driven feature selection (e.g., RFE on shared features) mitigates this variance and reduces schema mismatch, especially when positive classes are scarce [31]. Class imbalance and prevalence drift also distort thresholds: an operating point tuned on a tertiary center with 60–70% malignancy prevalence over-calls in community screening, while diabetes prevalence jumps between White and non-White cohorts in BRFSS, eroding precision and calibration.

Concrete cross-hospital failures underscore these themes. Meta-analyses of Mayo/VA/Brock successors show AUC reductions of 0.1–0.3 when models are transferred from U.S. academic centers to Asian screening programs, driven by different granuloma burdens, smoking histories, and scanner kernels [5, 7, 6]. Radiomics signatures tuned on sharp-kernel CTs lose discriminatory power on smooth-kernel images unless aggressively harmonized, and even then residual scanner bias can dominate texture features [10]. Cross-year BRFSS surveys alter wording and missingness patterns; features such as self-reported health or smoking show discrete shifts that break models calibrated on earlier years. These cases illustrate that without explicit feature pruning and alignment, both classic and modern models can become confidently wrong.

To demonstrate robustness beyond our private hospital cohorts, we additionally validate on a public cross-domain benchmark (TableShift BRFSS Diabetes) that introduces a race-driven shift (White → non-White) and survey-year drift. This setting mirrors the same combination of covariate, label, and concept shift while operating at national scale, ensuring that the proposed approach addresses both clinical and population-level distribution shifts without changing the chapter structure or adding new modeling components.

Safety and regulation make these failures more than academic. Post-market surveillance guidelines now expect evidence of calibration and drift monitoring when models are deployed across equipment upgrades, demographic mixes, or policy changes [24]. AUC alone cannot certify safe decision support: over-diagnosis from optimistic thresholds causes unnecessary biopsies, while under-diagnosis from prevalence shifts can miss aggressive lesions. Privacy constraints often forbid labeled target data, ruling out supervised recalibration. Any deployable system must therefore assume unlabeled targets, partial feature overlap, and shifting priors, while still exposing confidence and calibration behavior to human overseers.

The shift landscape is multifaceted and worth making explicit. Covariate shift ( $P_s(X) \neq P_t(X)$ ) emerges when scanner kernels, survey wording, or coding changes alter feature distributions; label shift ( $P_s(Y) \neq P_t(Y)$ ) follows from different prevalences across centers, races, or years; concept shift ( $P_s(Y | X) \neq P_t(Y | X)$ ) appears when new clinical guidelines, demographics, or comorbidities change the meaning of a feature vector [24]. Classical ERM optimizes source risk and leaves the divergence term uncontrolled, so even strong in-distribution accuracy fails to upper-bound target error. In practice, the three shifts co-occur: BRFSS race splits bundle covariate drift (lifestyle and socioeconomic factors), label shift (diabetes prevalence), and concept changes (different risk weight

for identical behaviors). Pulmonary nodules exhibit the same mix: granulomatous disease confounds location priors, and protocol upgrades change radiomic textures. These conditions invalidate the implicit closed-world assumptions behind most off-the-shelf models.

Prior attempts to bridge domains reveal recurring limitations. Adversarial discriminators and style-transfer methods from imaging presume shared feature grids and plentiful target data; in tabular medicine, missing columns, mixed data types, and unlabeled targets induce instability or mode collapse [22, 28]. Statistical alignment methods such as MMD and CORAL are more stable but still assume overlapping schemas and can degrade discriminative variance when applied naively. Invariant risk minimization and GroupDRO show promise in vision but routinely underperform tuned GBDTs on tabular benchmarks such as TableShift and Wild-Time [27]. These results motivate combining alignment with strong priors rather than expecting any single robustness mechanism to suffice.

Feature engineering choices matter as much as model class. Clinical tables mix continuous laboratory values, ordinal scores, sparse categorical codes, and structured missingness; simple one-hot encoding expands dimensionality and sparsity, harming small- $N$  generalization. Stability-driven feature pruning, hierarchical encoding of categorical variables, and unit-aware normalization reduce spurious site signatures and focus attention on shared, clinically interpretable signals [31]. Recursive feature elimination across domains further enforces schema overlap, trading a slight drop in ceiling accuracy for substantial gains in portability when hospitals differ.

The same caution extends to emerging tabular large-language-model approaches. Serializing rows into text prompts allows reuse of general reasoning, but tokenizing high-cardinality numerical columns inflates context windows, introduces quantization error, and increases latency; moreover, LLM priors trained on web text do not encode clinical calibration by default [20]. Without explicit calibration or domain alignment, TabLLM-style systems risk confident misclassification when faced with out-of-template lab panels or race-specific prevalence changes.

Regulatory and clinical workflows impose further constraints on deployment. Hospitals require traceable decision rationales, audit logs of model updates, and clear operating thresholds tied to disease prevalence. When labels cannot be shared across sites, calibration transfer must rely on unsupervised statistics or prior knowledge; model updates must avoid catastrophic forgetting of earlier domains while accommodating drift. These practical requirements narrow the design space toward approaches that separate representation learning from alignment and that make minimal assumptions about target supervision or schema completeness.

This study therefore proceeds from a pragmatic stance: it embraces tabular foundation models for their sample efficiency, but surrounds them with schema-aware feature pruning and unlabeled alignment so that attention operates on comparable examples even when hospitals, years, or races differ. The remainder of this manuscript formalizes the cross-domain problem, surveys prior art, and presents PANDA—a pipeline that chains cross-domain RFE, Transfer Component Analysis, and TabPFN inference—to restore calibration and discrimination under realistic deployment constraints.

Across these categories, shortcomings accumulate rather than cancel. Tree ensembles are non-differentiable and brittle in the small-sample regime; modest covariate shifts or low positive fractions push them toward overfitting and preclude gradient-based adaptation or calibration transfer across sites [8, 9]. Deep tabular models introduce differentiable representations but remain data hungry and tuning sensitive, and batch-statistic drift or coding changes can collapse learned embeddings when cohorts span hospitals or survey years [14]. Tabular foundation models improve sample efficiency but retain a closed-world view of the feature schema and marginal distributions: attention seeks nearest neighbors that may be non-comparable once scanners, biomarker panels, or demographic mixes shift, leading to confident but incorrect matches [21, 18]. Adaptation techniques borrowed from imaging—adversarial discriminators, cycle/style transfer, and optimal-transport aligners—assume shared feature grids and label access; they falter when target domains are unlabeled, omit variables entirely, or experience label drift, as documented on TableShift and in medical domain-adaptation surveys [28, 27, 24].

Despite rapid progress in deep tabular modeling, the combination of small-sample regimes, covariate drift, and feature-space mismatch remains largely unsolved in cross-hospital pulmonary nodule prediction. Existing AI methods—tree ensembles, deep tabular networks, and foundation-model variants—usually presume stable schemas or labeled targets, assumptions that rarely hold in real deployments. These gaps motivate a hybrid framework that integrates pre-trained tabular priors, schema-aware feature selection, and unsupervised domain alignment, which we develop in this study.

In cross-hospital pulmonary nodule prediction and BRFSS race-shift diabetes prediction, these gaps become acute: feature sets differ, prevalence drifts, and privacy blocks target labels, so neither trees, deep tabular models, foundation models alone, nor imaging-style domain adaptation offers a complete remedy. Any viable approach must combine strong priors, schema-aware feature pruning, and unlabeled distribution alignment to regain calibration and sensitivity under shift.

Our study therefore targets two representative settings: (i) cross-hospital pulmonary nodule prediction where Cohort A provides labels but Cohort B remains unlabeled, and (ii) the TableShift BRFSS diabetes race-split benchmark where White respondents form the source domain and non-White respondents form the target. Both settings reflect the same deployment realities: privacy constraints, schema mismatch, prevalence drift, and the need for sensitivity at clinically actionable thresholds. They also expose failure modes of purely supervised training and of foundation models without adaptation, offering a stress test for any proposed remedy.

Because HIPAA/GDPR rules forbid sharing labeled target data, supervised domain adaptation and threshold tuning on the target side are infeasible. Methods that assume label access or perfect feature overlap therefore cannot be deployed in these scenarios. Any practical solution must work with source labels only, respect schema intersections, and deliver calibrated probabilities despite prevalence changes. This motivation drives the alignment-heavy, feature-prudent strategy developed here.

Existing AI toolkits each leave gaps relative to these constraints. Tree ensembles cope with mixed scales and missingness but cannot be fine-tuned across domains and quickly overfit when positive cases are rare. Deep tabular models promise differentiable representations and multimodal fusion, yet they require large, clean cohorts and collapse when categorical codes or batch statistics shift. Tabular foundation models address the small- $N$  barrier but assume matched schemas and stable covariates, so attention retrieves misleading neighbors when acquisition protocols change or when hospitals omit variables. Generic domain-adaptation techniques from imaging—adversarial discriminators, style transfer, and optimal transport—presume either shared feature grids or labeled targets; they seldom consider missingness shift, prevalence drift, or unlabeled target domains that dominate clinical deployments. Without explicit feature pruning and alignment, these methods can become overconfident while making non-comparable comparisons across sites.

We therefore introduce *PANDA* (Pretrained Adaptation Network with Domain Alignment), a pragmatic framework that chains three proven ideas. First, TabPFN supplies a strong inductive prior for small cohorts by meta-learning across millions of synthetic tabular tasks [15]. Second, Transfer Component Analysis (TCA) aligns source and target distributions in a shared reproducing-kernel subspace without labeled target data, minimizing distributional divergence while preserving clinical variance [32]. Third, cross-domain Recursive Feature Elimination prunes to biomarkers that are consistently available and stable, mitigating schema mismatch and noisy hospital artifacts [31]. PANDA targets the explicit goal of cross-hospital pulmonary nodule prediction with screening-level sensitivity by combining these components rather than relying on any single modeling breakthrough.

## 2 Related Work

### 2.1 Tabular learning for medical data: tree ensembles, deep tabular networks, and tabular foundation models

The literature on structured-data learning has progressed from classical ensembles to deep tabular networks and, most recently, to tabular foundation models that mirror the trends in NLP and computer vision [33, 21]. We separate the discussion into tree ensembles, deep tabular architectures, and tabular foundation models to highlight where each excels and why none alone solves cross-hospital robustness. In medical settings, the same patient cohort may be modeled by tree ensembles, deep tabular networks, or foundation models depending on sample size and operational constraints; understanding their respective failure modes under domain shift is crucial for positioning PANDA.

#### 2.1.1 Tree ensembles for clinical tabular data

Gradient-boosted decision trees (GBDTs) such as XGBoost, LightGBM, and CatBoost remain the workhorses for EHR-style tables because they tolerate heterogeneous scales, missing values, and noisy categorical codes while supporting monotone constraints and other clinical priors [8, 34, 14]. Bench-

marking studies covering hundreds of OpenML tasks show that GBDTs still beat most neural baselines whenever training samples exceed a few thousand, yet they overfit rapidly when  $N < 1,000$ , cannot be fine-tuned incrementally, and require full retraining when hospitals change their feature schemas [9, 35, 36]. Case reports on cross-institutional readmission and mortality prediction show that tree models memorize acquisition artifacts (assay vendors, coding practices) and lose 10–20 AUC points when transferred without recalibration, illustrating their non-differentiable structure blocks end-to-end multimodal training and plug-and-play domain adaptation [37, 38]. This rigidity motivates attempts to distill tree priors into differentiable encoders so that adaptation can occur without rebuilding the model for each site. These same inductive biases explain why trees dominate mid-scale public benchmarks yet struggle in small, imbalanced medical cohorts: sparsity-aware splits handle missing labs gracefully, but boosting magnifies noise when positive classes are rare and hospital-specific priors leak into leaf structure. Because gradients stop at each split, trees cannot share representations with image encoders or participate in gradient-based domain adaptation, forcing manual feature harmonization whenever schemas or prevalence shift. In practice, this means that widely used implementations such as XGBoost and LightGBM shine on medium-to-large EHR cohorts with thousands of patients and hundreds of features, where sparse histogram-based splits and built-in handling of missing indicators yield strong baselines with modest tuning. Studies across OpenML, MIMIC-style EHR benchmarks, and TableShift-like suites repeatedly show that properly regularized XGBoost variants achieve AUROCs in the high 0.70s to low 0.80s for mortality, readmission, and sepsis detection, and that they retain their ranking power even when categorical encodings or measurement scales differ across hospitals [9, 36, 27]. These observations explain why tree ensembles remain the default choice for operational clinical decision support systems.

On the small, heavily imbalanced cohorts typical of lung-screening registries ( $N \approx 300$ ), the same capacity becomes a liability. Empirical analyses of GBDT behavior on few-shot medical datasets reveal several critical failure modes: first, deep trees can memorize the few malignant cases (often  $< 50$  positives), leading to apparent training accuracies  $> 95\%$  but test AUROCs collapsing once covariates shift [36, 27]. Second, calibration deteriorates dramatically in low-prevalence subgroups, with predicted probabilities systematically overestimating malignancy in young non-smokers while underestimating risk in elderly or high-burden cohorts [25, 24]. Third, when new hospitals add or remove variables (e.g., different CT protocol parameters or biomarker panels), there is no principled way to “warm start” or incrementally fine-tune existing tree models without complete retraining from scratch, making long-term maintenance expensive.

Because tree ensembles are non-differentiable and lack explicit latent representations, they are also difficult to integrate into end-to-end multimodal models or to pair with standard domain adaptation objectives. This mathematical constraint has practical consequences: researchers attempting to combine XGBoost with imaging features must resort to late fusion (averaging predictions) or feature concatenation followed by retraining, both of which preserve the non-differentiable barrier. Gradient-based domain adaptation methods such as Domain Adversarial Neural Networks (DANN) or Maximum Mean Discrepancy (MMD) regularization cannot be applied directly to tree models, requiring workarounds that approximate tree decision surfaces with differentiable surrogates or hybrid architectures that mix neural embeddings with gradient-boosted leaves. This limitation motivates methods that transfer tree-like priors into differentiable architectures or that use tree models as feature extractors rather than end-to-end learners.

### 2.1.2 Deep tabular networks

Deep tabular architectures import attention and representation learning from sequence models to overcome the adaptation gap. TabNet uses sequential feature masks to mimic decision paths, TabTransformer contextualizes categorical embeddings, FT-Transformer tokenizes all features, and SAINT introduces intersample attention plus contrastive pre-training to borrow signal across patients [11, 39, 40, 13]. Basis Transformers, NODE variants, TabICL prompt-serialization, weight-prediction, and regularization schemes further explore the space between neural and symbolic models [41, 42, 43, 44, 45]. However, comprehensive surveys and multiple leaderboard studies report that these models remain data-hungry, sensitive to hyperparameters, and often trail tuned tree ensembles on small, heterogeneous cohorts typical of tertiary hospitals [36, 35, 46]. In external-hospital transfers, SAINT and FT-Transformer frequently degrade to near-random calibration when categorical codes shift or when batch-size constraints prevent stable intersample attention. The computational footprint (long train-

ing times, GPU memory pressure) further limits adoption in clinical IT stacks, where inference latency and cost dominate. Empirical comparisons on clinical risk prediction echo this pattern with concrete performance gaps. TabNet often needs extensive learning-rate scheduling and sparsity penalties to match GBDT, and TabTransformer under-utilizes numerical biomarkers unless carefully normalized. FT-Transformer narrows the gap by embedding every feature, yet its quadratic self-attention becomes impractical for wide tables. SAINT’s intersample attention helps when minibatches are large, but collapses on scarce data, making these models fragile without strong regularization and carefully tuned augmentations.

Detailed benchmarking studies on clinical datasets reveal stark contrasts between large-scale public benchmarks and real-world medical cohorts. On UCI repository datasets with >10,000 samples, TabNet achieves AUROCs of 0.85–0.92, FT-Transformer reaches 0.87–0.94, and SAINT obtains 0.86–0.93, competitive with or slightly exceeding XGBoost’s 0.84–0.91 [9, 35]. However, when evaluated on authentic clinical cohorts with <1,000 patients and significant missingness, the same models show dramatic performance degradation: TabNet AUROCs fall to 0.62–0.71, FT-Transformer to 0.65–0.74, and SAINT to 0.60–0.69, while XGBoost maintains relatively stable performance at 0.75–0.83 [36, 46].

The computational requirements create additional barriers to clinical adoption. Training times for TabNet on a typical EHR dataset (1,000 patients, 50 features) range from 2–8 hours on a single GPU, compared to 5–15 minutes for XGBoost on CPU. FT-Transformer requires 4–12 hours due to its attention mechanisms, and SAINT needs 6–15 hours plus substantial memory for inter-sample attention matrices [36]. These computational costs translate to practical challenges: most hospital IT environments lack GPU infrastructure for model development, and the extensive hyperparameter tuning required (learning rate schedules, attention head configurations, regularization strengths) demands specialized machine learning expertise not commonly available in clinical settings.

Furthermore, calibration studies reveal that deep tabular models often produce overconfident predictions on medical data. Reliability diagram analyses show that TabNet and FT-Transformer consistently assign higher predicted probabilities than warranted by observed outcomes, particularly in rare disease subsets where expected calibration errors (ECE) can exceed 0.15–0.20 compared to XGBoost’s 0.04–0.08 [25, 46]. This overconfidence is particularly problematic for clinical decision support, where well-calibrated risk estimates are essential for appropriate triage and treatment decisions. These limitations are amplified in clinical registries where hundreds of variables encode comorbidities, medication history, and laboratory trajectories. Studies on ICU mortality, sepsis, and readmission prediction report that deep tabular networks match or slightly exceed tuned GBDTs on in-distribution test sets but lose their advantage when evaluated on later time periods or new hospitals, especially when categorical vocabularies change or when privacy constraints cap batch sizes [9, 25, 46]. In such small- $N$ , high-dimensional regimes, hyperparameter sensitivity translates directly into clinical risk: minor changes in learning rate or regularization can flip decisions near treatment thresholds. Compared with tree ensembles, these architectures seek to learn shared feature representations that might in principle adapt across hospitals or tasks. In practice, however, their appetite for data and tuning means that performance gains are often limited to large industrial benchmarks; on noisy, heterogeneous medical tables with only a few hundred patients, they frequently underperform simpler models and exhibit brittle calibration under shift. This contrast sets the stage for tabular foundation models such as TabPFN, which embrace a meta-learning, few-shot perspective instead of training a new deep network from scratch for each cohort.

### 2.1.3 Tabular foundation models

Tabular foundation models push self-supervised pre-training and in-context learning into structured data. TabPFN meta-trains a transformer on millions of synthetic datasets sampled from diverse structural-causal priors, learns to approximate posterior predictive distributions, and performs inference via a single forward pass without gradient updates [15, 47]. Follow-up work expands its reach without breaking the closed-world assumption: TabPFN-2.5 relaxes quadratic attention to accommodate tens of thousands of context rows and documents an augmented pre-training suite; diagnostics such as “A Closer Look at TabPFN v2” show that the model remains overconfident under covariate shift, prompting wrappers that adjust representations before prediction [16, 17, 18]. Drift-resilient variants model temporal shift with secondary structural-causal modules and record measurable gains when patient mixes evolve [48, 19]. Other studies adapt the same prior-learning paradigm to drug discovery, radiomics, and graph embeddings, highlighting both the portability and fragility of tabular

foundation models beyond flat tables [49, 20, 50]. Tabular Large Language Models (TabLLMs) serialize rows or mini tables into prompts so that general-purpose LLMs can reason over discrete entries, but they remain computationally prohibitive for high-throughput risk prediction and struggle with precise numeric calibration [51, 20, 52]. Recent analyses of high-dimensional omics applications reinforce that even TabPFN requires aggressive feature selection or prior-guided embeddings to stay calibrated, underscoring its closed-world assumption [53, 54]. PFN-Boost, LLM-Boost, and hybrid residual schemes blend foundation backbones with tree-style updates or prompts, but benchmark reports such as WildTab still find overfitting to training-domain quirks unless explicit alignment and calibration are layered on [55, 38, 42]. Closed-world constraints surface in three ways: (i) feature mismatch—TabPFN expects aligned schemas and cannot reason about biomarkers absent from the context; (ii) covariate drift—attention retrieves misleading neighbors when acquisition protocols move, producing overconfident errors; and (iii) context-length bottlenecks that force sub-sampling when rows exceed a few thousand. These limits explain why prior studies resort to RFE or hand-crafted embeddings before invoking TabPFN and why drift-resilient variants add causal dynamics to temper temporal shift.

These observations motivate hybrid approaches that explicitly combine strong priors with domain-alignment hooks. Table 1 summarizes the comparative strengths and weaknesses of these model families for medical tabular tasks, highlighting why PANDA fuses TabPFN with feature selection and unsupervised alignment instead of relying on any single paradigm.

Table 1: Comparative strengths and weaknesses of tabular model families in medical AI.

Model Class	Representative Algorithms	Strengths in Medical AI	Limitations in Cross-Hospital Tasks
Tree Ensembles	XGBoost, LightGBM, CatBoost	Interpretable, robust to missingness/outliers, encode clinical constraints	Overfit small cohorts, non-differentiable, no inherent transfer learning, require full retraining per site
Deep Tabular	TabNet, Transformer, FT-Transformer, SAINT, NODE	Differentiable, capture complex interactions, allow multimodal fusion	Data hungry, extensive tuning, high compute cost, brittle without alignment
Foundation Models	TabPFN, TabPFN-2.5, TabLLM	Hyperparameter-free inference, strong small- $N$ priors, probabilistic outputs	Sensitive to distribution/feature shift, limited context length, assume aligned schemas

## 2.2 Domain shift and domain adaptation in medical AI

Domain adaptation (DA) provides the vocabulary for managing the covariate, label, and concept shifts that materialize when AI crosses hospital boundaries. Classical analysis decomposes target error into source error plus a divergence term, motivating alignments and invariance objectives. In practice, medical deployments encounter overlapping types of shift: changes in patient mix and ordering policies alter  $P(X)$ , new screening programs or diagnostic criteria perturb  $P(Y)$ , and evolving clinical practice modifies  $P(Y | X)$  [24, 25]. Pulmonary nodule malignancy prediction is particularly exposed to this triad of shifts because granulomatous disease burden, scanner protocols, and radiologist thresholds vary sharply across regions.

### 2.2.1 Statistical alignment vs. adversarial objectives

Maximum Mean Discrepancy (as in TCA), correlation alignment (CORAL), and transport-based projections minimize moment discrepancies in a latent space [32, 56, 57, 58, 59]. They are attractive for medical tables because they offer closed-form or deterministic solutions and remain stable when labeled target data are absent. Adversarial approaches (DANN, cycle-consistent style transfer) attempt to erase domain cues via discriminators, but surveys show they destabilize when cohorts are tiny, leading to mode collapse or erasure of clinically salient signals [25, 58, 22]. In ICU mortality and readmission tasks, DANN can underperform ERM by wide margins because the discriminator trivially detects domain cues from missing patterns, causing the encoder to discard predictive features. In contrast, MMD- or CORAL-style alignment improves calibration modestly and avoids catastrophic

degradation, motivating our reliance on TCA for small-sample settings. Classic error decompositions also separate covariate shift ( $P_s(X) \neq P_t(X)$ ) from label shift ( $P_s(Y) \neq P_t(Y)$ ) and concept shift ( $P_s(Y|X) \neq P_t(Y|X)$ ); only the first benefits cleanly from moment matching, while the second demands prevalence-aware calibration and the third often needs feature auditing or human review [32, 27, 24]. These regimes frequently co-occur in multi-hospital deployments, explaining why single DA objectives show mixed results.

### 2.2.2 Heterogeneity, missingness, and temporal drift

Medical DA must grapple with heterogeneous feature sets and evolving acquisition policies. Feature-space DA (FSDA) and transport-based alignment project source and target into shared latent spaces, while open-set domain adaptation handles mismatched label spaces and schema drift that arise when hospitals collect different labs [60, 57, 61, 59]. DomainATM, feature-aware PCA, and ontological mapping frameworks first identify which biomarkers are stable across sites before alignment, reducing negative transfer [22, 62, 63]. Missingness-shift studies demonstrate that when ordering policies change (e.g., different lab panels for triage), standard covariate-shift assumptions break; MNAR-aware corrections and explicit missingness modeling become mandatory [64, 65]. Temporal adaptation work (Wild-Time, multi-attention encoders for COVID-19) highlights that drift accumulates over months, so models require continual recalibration rather than one-time transfer [28, 66].

### 2.2.3 Domain generalization and open-set gaps

TableShift, Wild-Tab, and Wild-Time benchmarks quantify how far models fall once distributions move: they reveal a near-linear relation between in-distribution and out-of-distribution accuracy, but also show that label shift dominates error budgets and that prevailing domain-generalization objectives (GroupDRO, IRM, VREx) rarely beat strong ERM or GBDT baselines on tabular data [27, 67, 68, 55, 28]. Open-set and partial-label settings are common in healthcare (target hospital omits certain comorbidities); current DA methods often assume aligned label spaces and therefore miscalibrate rare conditions. Regulatory guidance now treats shift detection and recalibration as part of post-market surveillance, emphasizing that robustness must be engineered rather than assumed [24]. Complementary benchmarks and surveys on generic tabular learning echo these findings: across hundreds of datasets, tuned GBDTs remain exceptionally strong baselines, and many deep or domain-generalization architectures fail to deliver consistent gains once evaluation moves beyond a handful of leaderboard tasks [36, 35, 45]. Moreover, empirical decompositions of error budgets highlight that label shift and calibration drift often dominate covariate shift, suggesting that feature-space alignment alone is insufficient for reliable deployment. Together with the medical DA literature, these results argue for methods that combine strong small-sample priors, explicit feature governance, and lightweight, task-aware alignment instead of relying on black-box “robust” architectures.

### 2.2.4 Domain adaptation and transfer learning for clinical tabular and EHR data

Recent work brings these ideas to longitudinal EHR and claims data. AdaDiag-style methods align source and target hospitals in a representation space while jointly training prognostic models, reporting partial recovery of AUROC lost when models trained on MIMIC-like cohorts are evaluated at external centers [58, 22]. Multi-center EHR foundation models go further by pre-training sequence encoders on records from dozens of institutions and then fine-tuning on downstream tasks, demonstrating that shared representations can reduce the amount of labeled data required for local adaptation [69]. These approaches show that both unsupervised alignment and transfer learning have value in clinical AI, but they typically assume abundant longitudinal data, focus on large hospitals with rich EHR infrastructure, and operate on sequential rather than static tabular summaries.

Standard domain-adaptation theory provides a unifying lens: target risk can be bounded by source risk plus a measure of distribution discrepancy and a term capturing irreducible label-set differences [32, 25]. Reducing error on the source domain alone is therefore insufficient; one must also control divergence between source and target feature distributions, for example via moment-matching, adversarial objectives, or feature-space DA. Beyond centralized settings, federated learning extends these ideas by allowing multiple hospitals to collaborate without sharing raw data. Surveys on federated learning for medical imaging and pattern recognition summarize how FL can pool experience across

institutions while preserving privacy, and methods such as FedFusion explicitly combine domain adaptation with personalized encoders to handle heterogeneous feature spaces and scarce labels [70, 71, 72]. However, most federated frameworks target high-volume imaging or EHR tasks, assume substantial local computation and at least some labeled data at each site, and still rely on shared model architectures and broadly aligned feature schemas. They are therefore complementary to, rather than a replacement for, lightweight DA strategies tailored to very small tabular cohorts with partially mismatched feature sets.

Table 2 summarizes the main DA families discussed above and their implications for cross-hospital tabular deployment.

Table 2: Representative domain-adaptation strategies in medical AI and their relevance to cross-hospital tabular risk prediction.

Method family	Typical modality	Key assumptions	Pros	Limitations for small cross-hospital tabular cohorts
Statistical alignment (MMD, TCA, CORAL, transport)	Tabular, EHR, imaging	Shared feature schema; access to source data and unlabeled target samples; primarily covariate shift	Closed-form or deterministic mappings; stable when target labels are absent; easy to plug into existing pipelines [32, 56, 57, 59]	Does not directly correct label or concept shift; assumes overlapping feature sets; may misalign rare subgroups without additional calibration [27, 24, 25]
Adversarial representation learning (DANN-style)	Imaging, EHR sequences	Access to source and target data with domain labels; discriminator encouraged to remove site identity	Learns domain-invariant representations jointly with task loss; flexible for complex modalities [25, 58]	Unstable on tiny cohorts; discriminators exploit missingness patterns, causing encoders to discard predictive features; can underperform ERM in ICU-style tasks [58, 22]
Feature-space DA and domain-aware FS (FSDA, DomainATM)	Tabular, EHR	At least partially shared feature space; access to both domains during training	Selects features that are predictive and stable across sites; reduces reliance on site-specific surrogates and noisy biomarkers [60, 22, 62, 63]	Still assumes sizable overlap in measured variables; does not natively handle missing entire feature blocks or unlabeled target hospitals with severe schema mismatch
Domain generalization and temporal adaptation (TableShift, Wild-Tab, Wild-Time)	Tabular	Multiple labeled source distributions; no target labels during training	Reveal failure modes under temporal, demographic, and institutional shift; provide standardized evaluation suites [27, 68, 55, 28]	Many domain-generalization objectives (e.g., GroupDRO, IRM, VREx) rarely beat strong ERM or GBDT baselines; benchmarks show label shift and calibration drift dominate what feature matching can fix [27, 67]
Federated and federated-DA frameworks (FL, FedFusion-style)	Imaging, tabular	Multiple computecapable hospitals; communication budget; typically some local labels and shared model architecture [70, 71, 72]	Preserve data privacy while learning from distributed cohorts; can combine personalization with domain adaptation and label efficiency	Often require significant local computation and labeled target data; focus on large imaging or EHR tasks; do not directly address very small tabular cohorts with feature mismatch and strict label scarcity

Existing EHR-focused methods mostly address temporal drift or site differences in large cohorts, whereas our setting combines small, imbalanced tabular cohorts, heterogeneous feature sets, and unlabeled target hospitals. This gap motivates PANDA’s combination of strong tabular priors, cross-domain feature selection, and lightweight alignment tailored to static risk scores rather than long EHR sequences.

## 2.3 Feature selection and domain-aware stability for small medical cohorts

High-dimensional yet small-sample tabular cohorts are ubiquitous in medicine: lung screening registries, omics panels, and survey-based risk scores often contain hundreds of variables for only a few hundred or thousand patients. Naïve learning in this regime leads to unstable decision boundaries and non-reproducible feature attributions. Feature selection methods aim to reduce dimensionality, stabilize inference, and focus clinician attention on biomarkers that are both predictive and economical to collect.

### 2.3.1 Small-sample and high-dimensional feature selection

Classical filter and wrapper methods, such as mutual information ranking or recursive feature elimination with SVMs, laid the groundwork for identifying compact biomarker sets but struggle when features are highly correlated or when class imbalance is severe [73]. More recent approaches explicitly target high-dimensional, low-sample-size settings. WPFS-style methods learn feature weights jointly with a classifier, GRACES uses graph convolutions to propagate importance across correlated features, and DeepFS leverages deep networks to screen features via nonlinear embeddings [74, 75, 76]. These techniques are attractive for medical AI because they can down-select from hundreds of candidate variables to a dozen stable predictors while controlling overfitting. Empirical studies on omics and imaging-genomics datasets show that such methods can maintain or even improve AUC while halving the number of features, directly reducing assay costs and simplifying model interpretation. However, most of these works assume a single training domain: the selected subset is optimized for internal performance and may not transfer when another hospital measures a slightly different panel or when missingness patterns change. From a methodological standpoint, this marks a shift from classical LASSO or univariate ranking—which rely on linear or marginal-effect assumptions and can be highly unstable in small cohorts—to architectures that explicitly model complex feature interactions and redundancy. WPFS and GRACES, for example, introduce auxiliary networks or graph structures to propagate importance across correlated features, while DeepFS leverages deep encoders to identify nonlinear manifolds where only a subset of variables drive variation [74, 75, 76]. These designs are particularly appealing in high-dimensional, sparse medical settings (omics panels, questionnaire data), but they still optimize for one domain at a time and do not ensure that the chosen biomarkers remain predictive under cross-hospital shift.

### 2.3.2 Feature selection with transformers and foundation models

Attention-based models provide an alternative route to feature selection by interpreting attention weights, learned masks, or perturbation scores as measures of importance. TabNet learns sparse feature masks that indicate which variables are consulted at each decision step, while transformer-based architectures expose token-level attention maps that can be aggregated across layers and heads [11, 12, 13, 45]. In practice, researchers often perform permutation-based importance estimation using a strong tabular backbone—GBDT or TabPFN—and then apply RFE-style pruning, retaining the top-k features that consistently contribute to performance. This paradigm is well-suited to small medical cohorts because it leverages the inductive biases of powerful models while regularizing the input space. For foundation models such as TabPFN, feature selection also mitigates closed-world constraints: by removing unstable or site-specific variables, one can reduce the chance that attention focuses on hospital identifiers or acquisition artifacts rather than pathology.

### 2.3.3 Domain-aware and cross-site feature selection

Standard feature selection treats all samples as exchangeable, implicitly assuming that feature-importance rankings are identical across domains. Domain-aware methods instead optimize a subset that is simultaneously predictive in multiple hospitals or under multiple sampling schemes. FSDA and related frameworks extend DA objectives with feature-level penalties, rewarding variables whose contributions remain stable after alignment [60, 31]. Multi-site studies on EHR and imaging data show that such cross-domain criteria can discard site-specific surrogates (e.g., local procedure codes) while preserving clinically meaningful biomarkers. PANDA adopts this philosophy in a pragmatic way: TabPFN is used as a strong scoring model, but feature elimination is guided jointly by source-site performance and cross-site stability, leading to a compact “best8” subset that is consistently informative in both

hospitals. These domain-aware subsets provide low-dimensional, harmonized inputs to TCA, reducing the risk of negative transfer and making the subsequent alignment problem better posed. Viewed through this lens, feature selection becomes a form of implicit domain alignment: instead of matching full distributions in a high-dimensional space, one first discards variables whose predictive contribution is strongly domain-specific and focuses on biomarkers that are consistently informative across sites. This is particularly valuable when hospitals measure different panels or exhibit pronounced missingness shift, because aligning on a smaller, shared subset of stable features is both statistically and operationally simpler. PANDA effectively instantiates this principle by using a pre-trained tabular foundation model to rank features jointly across two hospitals and retaining only those with robust importance, thereby coupling representation learning with domain-aware feature governance.

Table 3: Representative feature selection methods for small, imbalanced, high-dimensional biomedical tabular data.

Method	Model family	Small-sample / imbalance handling	Interpretability characteristics	Representative biomedical use cases
Recursive feature elimination (RFE) with linear or tree models	Wrapper around SVM, logistic regression, or tree ensembles	Wrapper search over feature subsets can overfit when $N$ is small and features are correlated; often combined with cross-validation and class-balanced sampling	Produces explicit ranked feature lists and compact subsets; easy to inspect and map to clinical variables [73]	Widely used in early gene-expression and biomarker panels; basis for many clinical risk-score and radiomics pipelines
LASSO / elastic-net logistic regression	Embedded linear models	$\ell_1$ or $\ell_1 + \ell_2$ penalties shrink coefficients, providing some robustness to high dimensionality; still assumes linear log-odds and can be unstable under heavy collinearity	Sparse coefficients directly indicate selected features; compatible with odds-ratio interpretation familiar to clinicians [73]	Common in radiomics and EHR risk models where interpretability and coefficient-based reporting are required
GRACES	Graph-convolutional-network-based FS [74]	Specifically targets high-dimensional, low-sample-size data by modeling feature relations on a graph; alleviates overfitting compared with independent filters	Outputs a compact subset informed by graph structure; can be visualized as a network of interacting biomarkers	Demonstrated on omics-style datasets; suitable when prior knowledge or correlations between biomarkers are important
DeepFS	Deep feature screening with autoencoders [75, 76]	Uses deep encoders to learn low-dimensional representations and rank features, handling ultra-high-dimensional, sparse, and potentially imbalanced data	Provides importance scores for each original feature; retains flexibility to operate in supervised or unsupervised mode	Evaluated on synthetic and biomedical high-dimensional datasets; useful when the number of variables far exceeds the number of patients
Domain-aware FS (FSDA-style)	Feature selection for domain adaptation [60]	Encourages selection of features that remain predictive across domains, implicitly handling covariate shift between sites	Produces subsets that are jointly predictive and domain-stable, supporting cross-hospital deployment	Applied to benchmark DA tasks; conceptually aligned with cross-hospital biomarker selection in multi-center medical studies
Transformer / foundation-model-based FS	Attention- or score-based selection using TabNet, TabTransformer, and tabular foundation models [11, 12, 45]	Leverages high-capacity or pre-trained models to estimate nonlinear feature importance; can be combined with RFE to mitigate small-sample overfitting	Attention weights, feature masks, or permutation-based scores yield ranked features; aligns with explainable-AI practices	Increasingly used in biomedical tabular and omics datasets; PANDA’s cross-cohort RFE uses a tabular foundation model as the scoring backbone

## 2.4 Pulmonary nodule malignancy prediction: from clinical scores to multi-modal AI

### 2.4.1 Clinical risk scores and logistic models

Pulmonary nodule malignancy prediction is a canonical testbed for cross-domain robustness. Classical logistic scores—Mayo Clinic, Veterans Affairs, Brock (PanCan), PKUPH, Li, and derivatives—achieve

internal AUCs above 0.85 but regularly drop to 0.60–0.80 in external validations, especially in Asian or community-screening cohorts where prevalence and granulomatous disease burdens diverge [1, 77, 2, 3, 4, 5, 6, 7]. These scores typically combine age, smoking history, nodule size, location, and morphology into a logit-based risk function. Meta-analyses covering tens of thousands of nodules confirm that calibration deteriorates most severely in subgroups such as solitary upper-lobe nodules and specific ethnic groups, reflecting both label-shift and covariate-shift mechanisms [5, 6, 7, 78]. While recalibration or re-estimation of coefficients can partially restore performance, these fixes require local labels and do not address feature-mismatch: new hospitals may lack some variables (e.g., emphysema grading) or measure them differently.

Targeted audits make the degradation concrete. In TB-endemic Korean hospitals, Mayo and VA shrink to AUC  $\approx$ 0.60 while Brock declines to  $\approx$ 0.68 despite an internal AUC near 0.94, and Chinese multi-center studies find that Brock and PKUPH can fall from  $\approx$ 0.90 internally to 0.70–0.77 once prevalence and granulomatous disease rates shift [79, 80, 81]. PET-augmented variants such as the Herder score raise internal discrimination to  $\approx$ 0.92 by incorporating metabolic imaging, yet they lose specificity in TB-endemic or inflammatory regions where uptake is nonspecific [82, 79]. These case studies underscore that most clinical scores embed site-specific prevalence, referral patterns, and feature definitions, so “plug-and-play” deployment without alignment is unrealistic.

Each classical score carries its own design trade-offs. The Mayo Clinic model was derived from several hundred clinic-referred patients with indeterminate nodules, emphasizing age, smoking, nodule diameter, spiculation, and upper-lobe location, whereas the Veterans Affairs model targeted high-risk, predominantly male veterans with larger lesions [1, 77]. The Brock (PanCan) model was trained in a screening cohort enriched for small nodules and incorporates emphysema, family history, and more granular morphology descriptors, while the PKUPH and Li scores adapt similar feature sets to Chinese tertiary-hospital and screening populations [2, 3, 4, 7]. A recent meta-analysis focused on the Brock model reports pooled AUC  $\approx$  0.80 across  $> 80,000$  patients but highlights substantially lower performance in Asian cohorts, solitary nodules, subsolid nodules, and larger lesions (AUC often  $\approx$  0.74 or below), underscoring that apparent “universality” in development data masks sizeable domain-specific errors [78]. Across Mayo, VA, Brock, and PKUPH, external validations repeatedly document drops from internal c-statistics in the high-0.80s to 0.60–0.75 when applied to community screening or granulomatous-disease-endemic regions [5, 6, 7].

These patterns can be summarized along three axes: development cohorts are often single-center and demographically narrow; variables focus on easily collected clinical and simple CT descriptors; and the underlying model is a logistic regression that assumes a linear log-odds relationship between covariates and malignancy. Table 4 sketches representative scores along these dimensions. In development, all achieve reasonable discrimination and are simple enough to implement as bedside calculators, but the same simplicity makes them brittle under shift: logistic coefficients absorb local prevalence, imaging protocols, and referral patterns, so external use without recalibration results in systematic underestimation or overestimation of risk in particular subgroups.

**Table 4: Representative pulmonary nodule malignancy scores and common external-validation issues.**

Score	Development cohort	Key variables	External-validation observations
Mayo Clinic	Clinic-referred indeterminate nodules in smokers	Age, smoking history, nodule size, spiculation, upper-lobe location	Internal AUC in the high-0.80s; frequent overestimation of risk and AUC drops to $\approx$ 0.6–0.7 in screening and non-U.S. cohorts
Veterans Affairs	Predominantly male veterans with larger nodules	Age, smoking, nodule diameter, location	Good performance in veterans; miscalibration when transported to mixed-gender or lower-risk populations
Brock (PanCan)	CT screening cohort with many small nodules	Age, sex, family history, emphysema, size, type, location	Meta-analytic pooled AUC $\approx$ 0.80; markedly lower AUC in Asian, solitary, and subsolid nodules [78]
PKUPH / Li	Chinese tertiary-hospital and screening cohorts	Age, smoking, nodule size and type, lobulation, spiculation	High internal AUC but drops in external series; performance depends strongly on CT protocol and case mix [3, 4, 7]

From the perspective of this thesis, these scores provide clinically interpretable baselines and useful prior knowledge about which coarse-grained descriptors matter, but they do not solve cross-hospital robustness. Their small development cohorts and rigid functional form make it difficult to incorporate new biomarkers or adapt to feature-mismatch without re-estimating the entire model, motivating more flexible tabular approaches that can share information across hospitals while respecting regulatory demands for calibration and subgroup transparency.

#### 2.4.2 Radiomics pipelines with traditional machine learning

Radiomics pipelines extract hundreds to thousands of hand-crafted features from CT volumes, offering richer representations than clinical risk scores but introducing major reproducibility hazards. Texture and wavelet descriptors vary with voxel spacing, reconstruction kernel, and segmentation protocol; ComBat-style harmonization reduces scanner effects yet requires batch labels and can blur subtle lesions [10, 5]. In internal validation, radiomics-based classifiers that pair LASSO- or stability-selected feature subsets with SVMs, random forests, or GBDTs typically report AUCs in the 0.75–0.90 range, but these numbers rarely carry over to new scanners or hospitals. External validations on LIDC-IDRI, LUNA16, and NLST repeatedly report double-digit AUC drops when deployed to scanners with different kernels or patient mixes, while shortcut-learning analyses show that models sometimes rely on grid artifacts or reconstruction noise rather than morphology [29, 30, 24]. These failures illustrate that radiomics alone cannot guarantee transportability and that alignment plus feature vetting are required before cross-hospital use.

Concrete exemplars reinforce that fragility. The Bayesian Integrated Malignancy Calculator (BIMC) blended radiomics with clinical covariates and modestly outperformed Mayo, Brock, and PKUPH ( $AUC \approx 0.90$  vs.  $\approx 0.78$ ) on an Italian derivation cohort, yet its advantage diminished when scanners, slice thickness, or kernels changed [83]. Hawkins-style NLST radiomics achieved  $AUC \approx 0.83$  without external validation, and retrospective audits show that a single reconstruction tweak can reorder the features selected by LASSO [5, 10]. Radiomics therefore supplies richer morphology descriptors but still requires harmonization, feature governance, and domain-aware alignment rather than assuming reproducibility across hospitals.

Table 5: Representative radiomics-based pulmonary nodule malignancy models and reported generalization behavior.

Study / model	Imaging data	Centers / nODULES	Classifier	Internal AUC	External AUC	Harmonization / scanner sensitivity
Generic radiomics pipelines	2D/3D chest CT or low-dose CT nodules	Single- or few-center cohorts (sizes vary)	LASSO- or stability-selected features with SVM, RF, or GBDT	Typically 0.75–0.90	0.10–0.20 lower	Performance degrades when kernel, slice thickness, or vendor changes; ComBat-style harmonization can reduce but not eliminate scanner effects [5, 10]
Multi-center reproducibility analyses	3D CT radiomics features across scanners	Multi-center CT datasets	–	–	–	Many texture features show intraclass correlation coefficients < 0.5 across vendors and protocols; harmonization helps but cannot fully restore stability [10]
Radiomics + clinical scoring models	Radiomics signatures combined with clinical descriptors	Hospital-specific or regional nodule cohorts	Elastic-net / logistic regression, RF, or GBDT	High ( $\geq 0.80$ )	Mid-0.70s or lower	External validations report double-digit AUC loss and sensitivity to case mix and acquisition protocol [5]

Published inter-scanner analyses often report intraclass correlation coefficients below 0.5 for entropy and run-length features, indicating poor reliability even before model fitting [10]. ComBat can regress out known batch effects when acquisition labels are available, but it can also blur subtle lesions and fails when batch membership is unknown at inference time, leaving a gap that tabular-alignment pipelines attempt to close. Beyond handcrafted features, many radiomics pipelines incorporate LASSO, elastic-net logistic regression, or stability-selection frameworks to shrink coefficients and stabilize feature sets before training SVM, random forest, or GBDT classifiers. Although these strategies help curb overfitting in small cohorts, they do not eliminate sensitivity to acquisition protocols: the same feature

may be retained in one scanner configuration and discarded in another because its estimated importance changes with kernel or slice thickness. Multi-center studies frequently report 10–20 percentage-point AUC drops when models are transported without revisiting segmentation, feature extraction, and harmonization choices [5, 10]. As a result, radiomics pipelines tend to behave like carefully tuned, center-specific instruments rather than plug-and-play risk predictors, and their complexity makes it hard for clinicians to trace failure modes back to specific preprocessing or feature-engineering steps.

#### 2.4.3 Deep-learning CAD systems

End-to-end deep-learning computer-aided diagnosis (CAD) systems extend the radiomics pipeline by learning 3D convolutional representations directly from CT volumes or multi-view patches. Large-scale screening trials such as NLST have enabled 3D CNNs to achieve AUCs in the mid-0.90s on internal validation, sometimes matching or surpassing expert radiologists [29]. Subsequent works combine deep features with handcrafted radiomics or clinical covariates, showing further gains on curated datasets [84, 85]. Causey et al.’s NoduleX reproduced radiologist malignancy ratings with  $AUC \approx 0.99$  on LIDC-IDRI, and Google’s NLST-scale 3D CNN maintained  $AUC \approx 0.94$  on an independent hospital cohort of 1,139 CTs, illustrating how massive, homogeneous datasets can suppress variance [86, 29]. However, these successes often rely on tightly controlled acquisition protocols and substantial annotation effort. External validations reveal double-digit AUC drops when voxel spacing, reconstruction kernels, or vendor mix shift, and shortcut-learning analyses demonstrate that CNNs may rely on markers, reconstruction noise, or scanner metadata rather than nodule morphology [30, 10, 24]. Moreover, most deep CAD systems treat imaging in isolation or only append a handful of clinical variables, limiting their ability to reason over complex comorbidity profiles or laboratory trajectories. Multi-view and multi-scale architectures that process cropped nodules, surrounding parenchyma, and whole-lung context can mitigate some of these issues, but they further increase computational cost and annotation effort. Multi-task variants that jointly predict malignancy, growth, or histological subtype promise richer supervision but require large, carefully curated datasets that few hospitals possess. In practice, many published CAD systems are trained and tuned on a single trial or institution, with limited reporting on cross-hospital generalization or calibration. Where multi-center experiments are reported, performance is typically rescued by site-specific fine-tuning on labeled cases from each target hospital, and very few studies attempt label-free “train at A, deploy at B” deployment. As a result, deep CAD systems remain powerful local tools rather than robust cross-hospital risk predictors.

#### 2.4.4 Tabular and multi-modal nodule models

Later machine-learning models—LASSO, random forests, GBDTs, Bayesian networks, and hybrid radiomics-clinical models—attempt to combine the strengths of scores and imaging [4, 5, 84, 85]. GBDTs and random forests improve internal calibration and handle nonlinear interactions but still require site-specific recalibration or feature mapping before deployment because their learned weights implicitly encode scanner kernels and local smoking histories. Multi-modal models that fuse deep image features with clinical covariates via late fusion or stacking demonstrate promising gains on LIDC-IDRI and NLST, yet most studies remain single-center or rely on random train–test splits that do not reflect real cross-hospital deployment. Only a handful of works evaluate performance when training on one hospital and testing on another, and these typically report substantial AUC drops and unstable decision thresholds [5, 10]. Recent multi-center studies in Asian and Chinese screening cohorts echo this pattern: even when models are re-estimated or augmented with additional imaging features for new hospitals, external AUCs often plateau in the low- to mid-0.70s and remain sensitive to protocol details and case mix [5, 10]. These observations motivate a shift toward tabular-centric models that can incorporate imaging-derived biomarkers while explicitly handling feature mismatch and domain shift rather than assuming homogeneous acquisition. Within the tabular family, two broad patterns emerge. Purely clinical models use logistic regression or tree ensembles on demographics, smoking history, and simple CT descriptors, sometimes enriched with laboratory indices or comorbidity scores. These models are attractive for deployment because all inputs are routinely available in electronic health records, yet they inherit the limitations of classical scores: most are developed and validated in a single institution, assume aligned features across sites, and rarely report behavior under explicit domain shift. Hybrid models instead treat radiomics signatures or deep image embeddings as additional covariates in a tabular classifier, enabling richer decision boundaries while retaining some interpretability via variable-

importance analyses. However, their feature spaces are even more brittle across scanners and hospitals, as both image-derived and clinical variables can change distributions or go missing.

Existing works seldom implement formal domain-adaptation strategies for these tabular or multi-modal models. External evaluations, when present, typically test a fixed model on a new hospital without feature re-alignment or recalibration, documenting sizable performance degradation but not offering systematic remedies. Only a few studies experiment with simple recalibration or refitting on a small local sample, and virtually none explore cross-domain feature selection or latent alignment tailored to nodule malignancy prediction [5, 10]. Consequently, the literature lacks robust, tabular-centric frameworks that (i) start from strong small-sample priors, (ii) identify a compact set of biomarkers stable across hospitals, and (iii) explicitly align feature distributions without assuming access to large labeled target cohorts. Taken together, these studies show that neither handcrafted risk scores, radiomics pipelines, nor deep CNN-based CAD systems currently offer reliable malignancy prediction across hospitals without local retraining or recalibration. Addressing these gaps is a central motivation for the PANDA framework developed in this thesis.

## 2.5 Benchmarks and open problems for cross-domain tabular learning

Beyond single-institution case studies, public benchmarks now stress-test shift robustness. TableShift curates 15 binary tasks across healthcare, finance, and public policy, with explicit temporal, geographic, and demographic shifts to measure out-of-distribution accuracy drops and calibration drift [27, 68]. Wild-Tab extends this idea to few-shot, structure-aware adaptation, showing that even tabular foundation models lose 5–15 AUC points under schema-preserving shifts [55]. Wild-Time focuses purely on temporal drift, revealing that performance decays monotonically unless models refresh their priors [28]. These resources contrast with medical imaging benchmarks, where the input grid is fixed; in tabular settings, feature heterogeneity and missingness add extra axes of mismatch. Our inclusion of the TableShift BRFSS Diabetes race-shift task aligns the pulmonary nodule study with a large-scale public benchmark, demonstrating that the proposed alignment strategy is not confined to proprietary cohorts. TableShift also surfaces common failure modes: GroupDRO and IRM rarely beat ERM on tabular tasks, label shift explains much of the OOD loss, and high ID accuracy is necessary but insufficient for shift robustness [27, 67]. Wild-Time isolates temporal drift, showing monotonic degradation without continual recalibration [28]; these findings mirror hospital deployments where assay updates or policy changes quietly reshape feature distributions.

### 2.5.1 Gap analysis and positioning of PANDA

Across model families and adaptation techniques, several open issues persist. First, closed-world assumptions in tabular foundation models preclude feature-mismatched deployment: TabPFN and its variants require aligned schemas and struggle when target hospitals omit or redefine biomarkers. Second, most DA methods presume access to abundant labeled or schema-aligned target data, which is unrealistic in privacy-constrained hospitals and incompatible with regulatory expectations that models remain stable under silent drift [24, 25]. Third, missingness shift and label shift remain underexplored despite being dominant drivers of clinical miscalibration in TableShift and Wild-Time; simply matching latent distributions cannot fix changes in prevalence or ordering policies [27, 28]. Finally, reproducibility crises in radiomics and deep imaging models show that aggressive priors or harmonization cannot replace explicit alignment and feature governance [10, 24].

PANDA is designed to address a specific intersection of these gaps rather than compete with every prior line of work. By treating a tabular foundation model as a plug-in prior, PANDA inherits strong small-sample performance without hand-tuning but augments it with cross-domain RFE that explicitly searches for a compact subset of biomarkers stable across hospitals. This step operationalizes domain-aware feature selection, yielding a shared feature set (“best8”) that remains predictive in both institutions and provides harmonized inputs for subsequent alignment. TCA is then applied in the latent space induced by TabPFN, combining the representation power of foundation models with the stability of kernel-based alignment to handle unlabeled target data. The same pipeline is evaluated both on a private cross-hospital pulmonary nodule cohort and on the public TableShift BRFSS Diabetes race-shift task, demonstrating that the ingredients are not handcrafted for a single dataset but generalize across tabular shift scenarios [27, 67]. To our knowledge, this is the first framework

to jointly combine a tabular foundation model, cross-domain RFE, and TCA for cross-hospital pulmonary nodule risk prediction and public TableShift-style tabular shift benchmarks. In this sense, PANDA fills the gap between single-domain tabular FMs, imaging-focused DA, and benchmark-driven tabular DA by providing an end-to-end, alignment-aware framework tailored to small, imbalanced, and feature-mismatched medical cohorts.

### 3 Problem Formulation

Cross-hospital medical diagnosis represents a complex intersection of small-sample learning, high-dimensional tabular data, and significant distribution shifts. In this chapter, we formalize the problem of predicting pulmonary nodule malignancy across different hospitals as an Unsupervised Domain Adaptation (UDA) task. We establish the mathematical foundations for our proposed PANDA framework, grounding it in the theory of Prior-Data Fitted Networks (PFNs), domain adaptation bounds, and kernel-based distribution alignment.

#### 3.1 Mathematical Notation and Preliminaries

We consider a supervised classification task where the input space is a  $d$ -dimensional feature space  $\mathcal{X} \subseteq \mathbb{R}^d$  comprising mixed numerical and categorical variables (e.g., patient age, tumor diameter, smoking status), and the output space is a binary label space  $\mathcal{Y} = \{0, 1\}$  (e.g., benign vs. malignant).

A **domain** is defined as a joint probability distribution  $P(\mathcal{X}, \mathcal{Y})$  over  $\mathcal{X} \times \mathcal{Y}$ . We are given data from two distinct domains:

- **Source Domain (Hospital A):** We observe a labeled dataset  $S = \{(\mathbf{x}_i^s, y_i^s)\}_{i=1}^{n_s}$  drawn i.i.d. from the source distribution  $\mathcal{D}_S$ . Here,  $n_s$  is the number of labeled samples in the source hospital.
- **Target Domain (Hospital B):** We observe an unlabeled dataset  $T = \{\mathbf{x}_j^t\}_{j=1}^{n_t}$  drawn i.i.d. from the marginal distribution  $P_T(X)$  of the target domain  $\mathcal{D}_T$ . The target labels  $Y_T$  are unobserved during training, reflecting the real-world constraint of deploying models to new hospitals without local ground truth.

**Feature Heterogeneity:** In multi-center studies, hospitals often record different sets of variables. Let  $\mathcal{F}_S$  and  $\mathcal{F}_T$  be the sets of feature indices available in the source and target domains, respectively. We define the **shared feature subspace** as the intersection  $\mathcal{F}_\cap = \mathcal{F}_S \cap \mathcal{F}_T$ . The effective input dimensionality for the cross-domain model is  $d_\cap = |\mathcal{F}_\cap|$ . Features in the set difference  $\mathcal{F}_\setminus = (\mathcal{F}_S \cup \mathcal{F}_T) \setminus \mathcal{F}_\cap$  are considered site-specific and are typically discarded for alignment, though they may contain domain-specific predictive signals.

Table 6 summarizes the key mathematical notations used throughout this thesis.

#### 3.2 The Tabular Data Generation Process: A PFN Perspective

Traditional machine learning assumes a fixed parametric form for the data generation process (e.g., a separating hyperplane for SVMs). In contrast, the TabPFN framework posits that the dataset  $\mathcal{D} = \{(\mathbf{x}_i, y_i)\}_{i=1}^N$  is generated from a **prior distribution over functions**, denoted as  $P_{\text{prior}}$ .

Formally, a dataset  $\mathcal{D}$  is sampled in two steps:

1. A structural equation model (SEM) or a data-generating function  $f$  is sampled from the prior:  $f \sim P_{\text{prior}}(\cdot)$ . In TabPFN, this prior is constructed explicitly using a large mixture of synthetic structural causal models (SCMs), including Bayesian Neural Networks and causal graphs with varying sparsity and non-linearity.
2. Data points are sampled conditioned on this function:  $y_i = f(\mathbf{x}_i) + \epsilon$ , or  $y_i \sim P(\mathcal{Y}|f(\mathbf{x}_i))$ .

The learning objective of a Prior-Data Fitted Network (PFN) is to approximate the **posterior predictive distribution** (PPD) for a query sample  $\mathbf{x}_{\text{query}}$  given the context dataset  $S$ :

$$PPD(y_{\text{query}} | \mathbf{x}_{\text{query}}, S) = \int P(y_{\text{query}} | \mathbf{x}_{\text{query}}, f) P(f | S) df \quad (1)$$

Table 6: Unified Mathematical Notation System

Symbol	Definition	Dimensions
<i>Domains and Data</i>		
$\mathcal{X}$	Input feature space (mixed numerical/categorical)	$\subseteq \mathbb{R}^d$
$\mathcal{Y}$	Label space (0: Benign, 1: Malignant)	$\{0, 1\}$
$\mathcal{D}_S, \mathcal{D}_T$	Source and Target domain distributions	over $\mathcal{X} \times \mathcal{Y}$
$S, T$	Empirical datasets drawn from $\mathcal{D}_S, \mathcal{D}_T$	Sets of size $n_s, n_t$
$\mathbf{x}, y$	Feature vector and corresponding label	$\mathbf{x} \in \mathbb{R}^d, y \in \mathcal{Y}$
$\mathcal{F}_{\cap}, \mathcal{F}^*$	Shared feature schema and RFE-selected subset	Subsets of indices
<i>Learning Theory</i>		
$h, \mathcal{H}$	Hypothesis function (classifier) and hypothesis class	$h : \mathcal{X} \rightarrow \mathcal{Y}$
$\epsilon_S(h), \epsilon_T(h)$	Expected risk (error) on Source and Target distributions	Scalar $\in [0, 1]$
$\hat{\epsilon}_S(h), \hat{\epsilon}_T(h)$	Empirical risk on datasets $S$ and $T$	Scalar $\in [0, 1]$
$d_{\mathcal{H}\Delta\mathcal{H}}$	$\mathcal{H}\Delta\mathcal{H}$ -Divergence (Domain Discrepancy)	Scalar $\geq 0$
$\lambda$	Ideal joint hypothesis error (Adaptability term)	Scalar $\geq 0$
$d_{VC}$	VC Dimension of hypothesis class $\mathcal{H}$	Scalar $\geq 1$
$\delta$	Confidence parameter for generalization bound	Scalar $\in (0, 1)$
$\mathcal{L}$	Loss function	$\mathcal{Y} \times \mathcal{Y} \rightarrow \mathbb{R}_{\geq 0}$
$\theta$	Model parameters (weights)	Vector $\in \mathbb{R}^k$
<i>PANDA Architecture</i>		
$\psi(\cdot)$	Domain adaptation mapping (TCA projection)	$\mathbb{R}^k \rightarrow \mathbb{R}^m$
$\mathbf{W}$	TCA Projection Matrix	$\mathbb{R}^{k \times m}$
$\mathbf{K}$	Kernel Matrix (Linear kernel on features)	$\mathbb{R}^{(n_s+n_t)^2}$
$\mathbf{L}$	MMD Indicator Matrix	$\mathbb{R}^{(n_s+n_t)^2}$
$\mathbf{H}$	Centering Matrix	$\mathbb{R}^{(n_s+n_t)^2}$
$\mu$	TCA Regularization Parameter	Scalar $> 0$
$\gamma$	RBF Kernel Bandwidth Parameter	Scalar $> 0$
$\varphi(\cdot)$	Implicit Feature Map to RKHS	$\mathcal{X} \rightarrow \mathcal{H}_{RKHS}$
$PPD$	Posterior Predictive Distribution $P(y \mathbf{x}, S)$	Probability

TabPFN approximates this integral using a Transformer-based architecture that attends to the entire context  $S$  (In-Context Learning). This perspective is particularly advantageous for the medical small-sample setting ( $n_s < 500$ ) because:

- It avoids iterative gradient descent on the small dataset, mitigating the risk of overfitting to noise.
- It leverages the "knowledge" encoded in the prior  $P_{\text{prior}}$ , effectively transferring inductive biases about tabular structures (e.g., decision boundaries are often aligned with axes, sparsity is common) to the medical task.

However, the standard PFN assumes that the query sample  $\mathbf{x}_{\text{query}}$  comes from the same distribution as  $S$  (i.e., same  $f$ ). In our cross-hospital setting, the target query  $\mathbf{x}^t$  comes from a shifted distribution  $\mathcal{D}_T$ , violating the exchangeability assumption of the posterior approximation.

### 3.3 Formalizing Domain Shift

The core challenge in our research is that  $\mathcal{D}_S \neq \mathcal{D}_T$ . This joint distribution shift can be decomposed into three primary components relevant to medical AI:

#### 3.3.1 Covariate Shift: The Acquisition Gap

Covariate shift occurs when the marginal feature distributions differ,  $P_S(X) \neq P_T(X)$ , while the conditional probability of the label remains constant,  $P_S(Y|X) = P_T(Y|X)$ .

$$P_S(X) \neq P_T(X) \quad \text{and} \quad P_S(Y|X) = P_T(Y|X) \quad (2)$$

In pulmonary nodule diagnosis, this is often driven by technological heterogeneity. For instance, CT scanners use different reconstruction kernels (e.g., "Sharp" vs. "Smooth"). A nodule scanned with a sharp kernel will systematically exhibit higher values for texture features like "entropy" or "spiculation" compared to the same nodule scanned with a smooth kernel, shifting the probability density function  $P(\mathbf{x}_{\text{texture}})$  without changing the underlying malignancy risk. TabPFN is particularly sensitive to this because its attention mechanism relies on finding similar examples in the support set; if the target  $\mathbf{x}^t$  lies in a region unsupported by  $P_S(X)$ , the attention weights become diffuse.

#### 3.3.2 Label Shift: The Prevalence Gap

Label shift, or prior probability shift, is defined by a change in the marginal label distribution:

$$P_S(Y) \neq P_T(Y) \quad (3)$$

This is endemic to healthcare referrals. A tertiary cancer center (Source) typically receives high-risk referrals with a malignancy prevalence of  $P(\mathcal{Y} = 1) \approx 60\%$ . In contrast, a community screening program (Target) encounters a broader population with many benign incidental findings, where  $P(\mathcal{Y} = 1) \approx 5\% - 20\%$ . A model trained on the balanced source will learn a prior  $\pi_S$  and systematically overestimate risk on the target, leading to poor calibration and excessive false positives.

#### 3.3.3 Concept Shift: The Definition Gap

Concept shift implies a fundamental change in the relationship between features and labels:

$$P_S(Y|X) \neq P_T(Y|X) \quad (4)$$

In pulmonary medicine, this arises from latent confounders such as geographic pathology. In regions like the Ohio River Valley (USA) or parts of East Asia, granulomatous diseases (e.g., Histoplasmosis, Tuberculosis) are endemic. These benign lesions often mimic the radiographic appearance of malignancy (e.g., spiculation, upper-lobe location). Consequently, a feature vector  $\mathbf{x}$  that indicates a 90% probability of cancer in a non-endemic source hospital might only indicate a 40% probability in a TB-endemic target hospital.

### 3.3.4 Theoretical Bound on Generalization Error

Following the seminal theory by Ben-David et al., the expected error of a hypothesis  $h$  on the target domain,  $\epsilon_T(h)$ , is bounded by:

$$\epsilon_T(h) \leq \epsilon_S(h) + \frac{1}{2}d_{\mathcal{H}\Delta\mathcal{H}}(\mathcal{D}_S, \mathcal{D}_T) + \lambda \quad (5)$$

where:

- $\epsilon_S(h)$  is the source domain error, minimized via supervised training.
- $d_{\mathcal{H}\Delta\mathcal{H}}(\mathcal{D}_S, \mathcal{D}_T)$  is the  $\mathcal{H}\Delta\mathcal{H}$ -divergence between the two domains.
- $\lambda = \min_{h \in \mathcal{H}} [\epsilon_S(h) + \epsilon_T(h)]$  is the error of the ideal joint hypothesis.

This bound highlights that minimizing source error is insufficient; we must explicitly minimize the divergence  $d_{\mathcal{H}\Delta\mathcal{H}}(\mathcal{D}_S, \mathcal{D}_T)$ .

## 3.4 Theoretical Constraints of Existing Models

To justify the architecture of PANDA, we formally analyze why existing state-of-the-art models fail in this specific regime ( $N \approx 300$ , Unlabeled Target, Tabular Data).

### 3.4.1 Gradient Boosted Decision Trees (GBDT)

GBDTs (e.g., XGBoost, LightGBM) partition the feature space using hard, axis-aligned splits ( $\mathbb{I}(\mathbf{x}_j < \theta)$ ). They suffer from two critical limitations in UDA:

1. **Non-Differentiability:** The piecewise constant decision boundary is non-differentiable with respect to input features. This precludes the use of gradient-based domain alignment techniques (like Adversarial Training or Gradient Reversal Layers) which require backpropagating a domain loss into the feature encoder.
2. **Inability to Extrapolate:** Tree models cannot extrapolate beyond the range of the training data. If covariate shift pushes the target distribution  $P_T(X)$  outside the support of  $P_S(X)$ , the tree maps all such points to the value of the nearest leaf node, often resulting in statistically invalid predictions.

### 3.4.2 Deep Tabular Models

Deep learning models (e.g., TabNet, FT-Transformer) offer differentiability but lack the appropriate inductive bias for small tabular datasets:

1. **Data Hunger:** Neural networks typically require large datasets ( $N > 10^4$ ) to converge to a generalizable solution. With  $n_s \approx 300$ , deep models are prone to severe overfitting or convergence to local minima.
2. **Rotational Invariance:** Standard MLPs are rotationally invariant, but tabular features are not rotationally interchangeable (e.g., rotating "Age" and "Creatinine" axes creates a nonsensical feature space). This mismatch in inductive bias makes them less sample-efficient than tree-based or prior-fitted methods.

## 3.5 Transfer Component Analysis (TCA) Optimization Objective

To minimize the divergence term in Eq. 5, we employ Transfer Component Analysis (TCA). TCA seeks a feature map  $\varphi : \mathcal{X} \rightarrow \mathcal{H}_{RKHS}$  such that the Maximum Mean Discrepancy (MMD) between source and target distributions in the Reproducing Kernel Hilbert Space (RKHS) is minimized.

The empirical MMD distance is defined as:

$$\text{MMD}(\mathcal{D}_S, \mathcal{D}_T) = \left\| \frac{1}{n_s} \sum_{i=1}^{n_s} \varphi(\mathbf{x}_i^s) - \frac{1}{n_t} \sum_{j=1}^{n_t} \varphi(\mathbf{x}_j^t) \right\|_{\mathcal{H}}^2 \quad (6)$$

TCA aims to learn a transformation matrix  $\mathbf{W} \in \mathbb{R}^{(n_s+n_t) \times m}$  that reduces the data dimensionality to  $m \ll d$  while minimizing MMD. The optimization problem is formally:

$$\begin{aligned} \min_{\mathbf{W}} \quad & \text{tr}(\mathbf{W}^\top \mathbf{K} \mathbf{L} \mathbf{K} \mathbf{W}) + \mu \text{tr}(\mathbf{W}^\top \mathbf{W}) \\ \text{s.t.} \quad & \mathbf{W}^\top \mathbf{K} \mathbf{H} \mathbf{K} \mathbf{W} = \mathbf{I} \end{aligned} \quad (7)$$

where:

- $\mathbf{K} \in \mathbb{R}^{(n_s+n_t) \times (n_s+n_t)}$  is the kernel matrix computed on the union of source and target data (specifically, the RFE-selected features). We specifically employ a **Linear Kernel** on these features:  $\mathbf{K}_{ij} = \langle \mathbf{x}_i, \mathbf{x}_j \rangle$ . This is justified because the RFE process aims to select a set of features that are already more linearly separable or amenable to linear transformation. Using a linear kernel provides a robust and computationally efficient alignment without introducing complex hyperparameter tuning for RBF bandwidths.
- $\mathbf{L}$  is the MMD coefficient matrix, with elements  $\mathbf{L}_{ij} = 1/n_s^2$  if  $\mathbf{x}_i, \mathbf{x}_j \in S$ ,  $1/n_t^2$  if  $\mathbf{x}_i, \mathbf{x}_j \in T$ , and  $-1/(n_s n_t)$  otherwise.
- $\mathbf{H} = \mathbf{I} - \frac{1}{n_s+n_t} \mathbf{1} \mathbf{1}^\top$  is the centering matrix.
- The constraint  $\mathbf{W}^\top \mathbf{K} \mathbf{H} \mathbf{K} \mathbf{W} = \mathbf{I}$  ensures the variance of the projected data is preserved (maximizing information).

### 3.6 The PANDA Framework: A Unified Formalization

We formalize our proposed **PANDA** (Pre-trained tAbular fouNdaTion model with Domain Adaptation) framework as a composite function  $f_{\text{PANDA}} : \mathcal{X} \rightarrow \mathcal{Y}$ . The inference process for a target sample  $\mathbf{x}$  is defined as:

$$f_{\text{PANDA}}(\mathbf{x}) = h(\psi(\mathbf{x}; \mathcal{F}^*)) \quad (8)$$

This composition involves distinct stages, grounded in the optimization of the feature subspace prior to alignment:

#### 3.6.1 Stage 1: Recursive Feature Elimination (RFE) with TabPFN

Directly applying domain adaptation on high-dimensional, noisy feature spaces often leads to negative transfer. We employ Recursive Feature Elimination (RFE) to determine the optimal subspace  $\mathcal{F}^* \subseteq \mathcal{F}_\cap$ .

Let  $S^{(0)} = \mathcal{F}_\cap$  be the initial set of shared features. The RFE process generates a sequence of feature subsets  $S^{(0)} \supset S^{(1)} \supset \dots \supset S^{(d-k)}$ , where  $k$  is the target dimensionality. At each iteration  $t$ :

1. **Model Fitting:** We define the TabPFN posterior predictive distribution conditioned on the current subset  $S^{(t)}$  using the source data  $S$ .
2. **Importance Estimation ( $\mathcal{I}$ ):** Unlike linear models, TabPFN is a non-parametric meta-learned model. We approximate feature importance using **Permutation Importance**. For each feature  $\mathbf{x}_j \in S^{(t)}$ , we compute the degradation in the AUC metric when feature  $\mathbf{x}_j$  is randomly permuted in the validation set:

$$\mathcal{I}(\mathbf{x}_j; S^{(t)}) = \mathcal{L}_{\text{AUC}}(h_{S^{(t)}}, S) - \mathcal{L}_{\text{AUC}}(h_{S^{(t)}}, S^{\text{perm}(j)}) \quad (9)$$

3. **Elimination:** We identify and remove the feature with the minimal contribution:

$$f_{\min} = \underset{\mathbf{x}_j \in S^{(t)}}{\operatorname{argmin}} \mathcal{I}(\mathbf{x}_j; S^{(t)}) \quad \longrightarrow \quad S^{(t+1)} = S^{(t)} \setminus \{f_{\min}\} \quad (10)$$

The final subset  $\mathcal{F}^*$  is selected to maximize stability and discriminative power, effectively reducing the  $\lambda$  term (joint error) in the Ben-David bound by removing concept-shifted features.

### 3.6.2 Stage 2: Foundation Model Encoding ( $\phi$ )

[Deprecated]

### 3.6.3 Stage 2: Domain Adaptation Mapping ( $\psi$ ) and Classification ( $h$ )

Following RFE, the selected features are then adapted using TCA. The domain adaptation mapping  $\psi$  operates on the RFE-selected features  $\mathcal{F}^*$  to project them into a domain-invariant subspace. This transformed feature set,  $\mathbf{x}' = \psi(\mathbf{x}; \mathcal{F}^*)$ , is then fed into the TabPFN classifier. The classification function  $h$  represents the combined operation of the TabPFN classifier and the ensemble-based temperature scaling, which together yield the final calibrated malignancy probability.

## 3.7 Clinical-Statistical Mapping

Table 7 summarizes the correspondence between the clinical challenges observed in pulmonary nodule diagnosis, their statistical manifestations, and the corresponding PANDA solution components derived from our theoretical framework.

Table 7: Mathematical Mapping of Clinical Problems to PANDA Components

Clinical Challenge	Statistical Mechanism	PANDA Component	Theoretical Justification
Scanner Variance (Sharp vs. Smooth Kernels)	Covariate Shift: $P_S(X) \neq P_T(X)$	Latent TCA on RFE-selected features	Minimizes MMD divergence $d_{\mathcal{H}\Delta\mathcal{H}}$ in RKHS.
Referral Patterns (Cancer Center vs. Screening)	Label Shift: $P_S(Y) \neq P_T(Y)$	Ensemble Aggregation & Temperature Scaling	Calibrates posteriors; smooths overconfidence from prior mismatch.
Biological Confounders (TB vs. Cancer)	Concept Shift: $P_S(Y X) \neq P_T(Y X)$	Cross-Domain RFE	Minimizes joint error $\lambda$ by removing unstable features.

## 3.8 Problem Constraints and Research Scope

Our formulation is bound by specific constraints inherent to the medical domain:

- **Small Sample Size Constraint:** The sample sizes  $n_s, n_t$  are typically in the range of 100 to 1000. This prohibits the use of deep domain adaptation networks.
- **Privacy and Data Silos:** We assume source data  $\mathcal{D}_S$  and target data  $\mathcal{D}_T$  cannot be physically merged.
- **Class Imbalance:** The prevalence of the positive class is often low ( $\pi < 0.3$ ), requiring AUC-centric optimization.

This formalization sets the stage for the specific methodological implementations detailed in Chapter 4.

## 4 Solution: The PANDA Framework

To bridge the gap between advanced tabular foundation models and the practical constraints of cross-hospital medical AI, we introduce PANDA (**P**re-trained **t****A**bular **fou****N**dation model with **D**omain **A**daptation). PANDA is a composite algorithmic framework designed to predict pulmonary nodule malignancy with high stability across heterogeneous clinical environments. It explicitly addresses the

tripartite challenge of small-sample scarcity, distribution shift, and feature heterogeneity through a tightly integrated pipeline.

We formalize the PANDA solution as a composite function  $f_{\text{PANDA}} : \mathcal{X} \rightarrow [0, 1]$  mapping raw, heterogeneous input space to a calibrated malignancy probability. The framework consists of four sequential stages: (1) Domain-Aware Feature Alignment and Selection, (2) Foundation Model Feature Extraction, (3) Latent Space Domain Adaptation, and (4) Multi-View Ensemble Classification.

## 4.1 Architectural Overview

The PANDA framework operates as a directed acyclic graph (DAG) of data transformations, guiding raw clinical inputs through a carefully orchestrated sequence to produce a calibrated malignancy probability. Table 8 details this journey, illustrating how feature representations evolve at each stage.

Table 8: Data flow and transformations in the PANDA framework. The pipeline progressively refines the data from raw, high-dimensional inputs to low-dimensional, domain-invariant embeddings, and finally to a calibrated probability.

Stage	Component	Input Space	Core Operation	Output Space
1	Feature Alignment	$\mathbb{R}^{d_{\text{raw}}}$	Schema intersection $\cap$	$\mathbb{R}^{d_{\cap}}$
2	Cross-Domain RFE	$\mathbb{R}^{d_{\cap}}$	Iterative elimination via $\mathcal{I}(f)$	$\mathbb{R}^k$ ( $k \approx 8$ )
3	Latent TCA	$\mathbb{R}^k$	Projection $\mathbf{x}' = \mathbf{W}^\top \mathbf{x}$	$\mathbb{R}^m$ ( $m = 15$ )
4	TabPFN Classifier	$\mathbb{R}^m$	Classification $f_{\text{TabPFN}}(\mathbf{x}')$	[0, 1] (Prob.)
5	Ensemble	$[0, 1]^{B \times S}$	Temperature-scaled averaging	[0, 1] (Final)

The data journey begins with **Stage 1: Feature Alignment**. Here, we perform a robust schema intersection ( $\mathcal{F}_{\cap}$ ) between the features available in the source domain and each target hospital’s dataset. This crucial step effectively addresses the “missingness shift” by identifying the maximal common feature set, ensuring that only universally collected and relevant variables proceed through the pipeline, even if certain examinations are not uniformly performed across all clinical sites.

Following alignment, **Stage 2: Cross-Domain Recursive Feature Elimination (RFE)** takes over. From the  $d_{\cap}$  features, this stage systematically reduces the dimensionality to a concise set of  $k \approx 8$  clinically impactful features, denoted as  $\mathcal{F}^*$ . This reduction is not arbitrary; it serves to minimize the joint error ( $\lambda$ ) across domains and guarantees that the selected features are practically acquirable by all participating hospitals. This process aligns directly with the feature set  $\mathcal{F}^*$  and the target feature space for domain  $t$ ,  $S^{(t)}$ , as introduced in Section 3.6.1.

Subsequently, in **Stage 3: Latent Transfer Component Analysis (TCA)**, the refined feature set  $\mathbb{R}^k$  is adapted. TCA projects these features into a lower-dimensional, domain-invariant space  $\mathbb{R}^m$  (typically  $m = 15$ ). This projection,  $\mathbf{x}' = \mathbf{W}^\top \mathbf{x}$ , is learned to minimize the Maximum Mean Discrepancy (MMD) between the source and target domain distributions in this latent space, thereby mitigating covariate shift.

**Stage 4: TabPFN Classifier** then processes the TCA-transformed features to predict the initial malignancy probability. In this stage, the TabPFN acts as a robust, pre-trained classifier on the domain-adapted data. Its in-context learning capabilities allow it to infer complex, non-linear decision boundaries without extensive gradient updates on small medical datasets.

Finally, **Stage 5: Ensemble** aggregates predictions from multiple TabPFN Classifier instances. This involves temperature scaling of the individual TabPFN outputs, followed by averaging across  $B \times S$  ensemble members, yielding the final, calibrated malignancy probability. The temperature scaling is crucial for adjusting predicted probabilities to account for potential label shifts between domains, ensuring more reliable and interpretable outputs.

## Mapping to Formal Problem Formulation

To establish a clear connection between the PANDA framework’s architectural stages and its formal problem formulation presented in Section 3.6, we explicitly map the components of  $f_{\text{PANDA}}(\mathbf{x}) = h(\psi(\mathbf{x}; \mathcal{F}^*))$  to the corresponding stages:

- $\mathcal{F}^* \leftarrow$  Stages 1–2 (Schema Intersection + Cross-Domain RFE)

- $\psi \leftarrow$  Stage 3 (Latent TCA)
- $h \leftarrow$  Stages 4–5 (TabPFN Classifier + Ensemble/Calibration)

This mapping clarifies how the abstract components of the PANDA function are instantiated through the concrete processing steps, providing readers with a direct link between theory and implementation.

## 4.2 Core Component I: TabPFN as a Robust Classifier

The backbone of PANDA is the TabPFN (Tabular Prior-Data Fitted Network) foundation model. While TabPFN is capable of extracting embeddings, in the PANDA framework, we leverage it primarily as a robust **Classifier** operating on the domain-adapted features. This strategic choice is driven by TabPFN’s unique ability to generalize well on small tabular datasets without extensive domain-specific fine-tuning. Mathematically, after the feature set  $\mathbf{x}$  has been aligned and reduced (Stages 1-2) and then adapted by TCA into  $\mathbf{x}'$  (Stage 3), the TabPFN classifier  $f_{\text{TabPFN}}(\cdot)$  directly maps these transformed features to a malignancy probability:

$$f_{\text{TabPFN}}(\mathbf{x}') \in [0, 1] \quad (11)$$

Here, the entire pre-trained TabPFN model, including its Transformer encoder and classification head, is used to make predictions.

**Theoretical Advantage (Prior-Data Fitted Learning):** The core innovation here is leveraging the **Prior-Data Fitted (PFN)** nature of TabPFN. TabPFN was meta-trained on millions of synthetic datasets generated from Structural Causal Models (SCMs). This meta-training instills a strong Bayesian prior  $P_{\text{prior}}$  that favors simple, causal explanations over spurious correlations. In the context of medical data, where sample sizes are often small ( $n_s \approx 300$ ), traditional deep learning models typically overfit. However, TabPFN’s meta-learned prior allows it to infer complex, non-linear decision boundaries (e.g., non-linear interactions between Age and Nodule Size) on the adapted features without requiring gradient updates on the small medical dataset. This directly addresses the "Small Sample Size" constraint defined in Section 3. By applying TabPFN to TCA-transformed features, we benefit from both domain invariance and strong generalization capabilities on small cohorts.

## 4.3 Core Component II: Cross-Domain RFE with Cost-Effectiveness Index

Medical datasets often contain high-dimensional noise (e.g., irrelevant radiomics features) and "concept shift" (features whose predictive value changes across hospitals). To handle this, we employ a Cross-Domain Recursive Feature Elimination (RFE) mechanism. The selection process is not merely about maximizing AUC; it is governed by a global **Cost-Effectiveness Index (CEI)** that balances predictive power against stability, clinical acquisition cost, and model complexity. We formulate the optimization problem for the optimal feature subset size  $k^*$  as:

$$\mathcal{F}^* = \underset{k}{\operatorname{argmax}} (w_1 S_{\text{perf}}(k) + w_2 S_{\text{eff}}(k) + w_3 S_{\text{stab}}(k) + w_4 S_{\text{simp}}(k)) \quad (12)$$

where the components are defined as:

- **Performance ( $S_{\text{perf}}$ ):** A weighted sum of AUC and F1 Score on the source validation folds.
- **Efficiency ( $S_{\text{eff}}$ ):** Measures the reduction in clinical burden, defined as  $1 - \frac{\text{Cost}(\mathcal{F}_k)}{\text{Cost}(\mathcal{F}_{\text{total}})}$ , where Cost proxies for the difficulty of acquiring the feature (e.g., age is cheap, contrast CT is expensive).
- **Stability ( $S_{\text{stab}}$ ):** Quantifies the robustness of the feature subset across cross-validation folds, defined as  $1 - \text{Std}(\text{AUC})$ .
- **Simplicity ( $S_{\text{simp}}$ ):** A sparsity penalty  $\exp(-\alpha k)$  to prefer smaller, clinically manageable subsets (typically  $k \in [5, 10]$ ).

Implementation-wise, we use ‘TabPFNClassifier’ as the base estimator for RFE. In each iteration, we calculate the **Permutation Importance**  $\mathcal{I}(\mathbf{x}_j)$  of each feature  $\mathbf{x}_j$ . The feature with the lowest importance is pruned, and the model is re-evaluated. This recursive process ensures that the retained

features  $\mathcal{F}^*$  are not only predictive but also stable against the noise inherent in small cohorts. In our experiments, this process consistently identifies a "Best-8" subset (Age, Spiculation, Lobulation, Diameter, etc.) that is robust across hospitals.

#### 4.4 Core Component III: Latent Space TCA Adaptation

To explicitly align the source and target distributions, we apply Transfer Component Analysis (TCA) to the feature space reduced by RFE (Stage 2). Standard TCA is often applied to raw features, but this is suboptimal for complex medical data where the manifold structure might be noisy or high-dimensional. Instead, we construct the kernel matrix  $\mathbf{K}$  using the RFE-selected features  $\mathbf{x}$ . Specifically, we employ a **Linear Kernel** on these features:

$$\mathbf{K}_{ij} = \langle \mathbf{x}_i, \mathbf{x}_j \rangle \quad (13)$$

This projection,  $\mathbf{x}' = \mathbf{W}^\top \mathbf{x}$ , learns a domain-invariant feature representation that is then fed into the TabPFN Classifier (Stage 4).

**Justification for Linear Kernel on RFE-Selected Features:** After Cross-Domain RFE, the selected features are assumed to reside in a more disentangled and clinically relevant space. In this context, a simple linear alignment via TCA is often sufficient to match the first-order moments of the distributions, thereby reducing covariate shift. This approach avoids the complexity and hyperparameter sensitivity (e.g.,  $\gamma$  in RBF kernels) that often plagues non-linear kernel methods, especially on small datasets. The subsequent TabPFN Classifier is then capable of modeling complex non-linear relationships within this linearly adapted feature space.

The optimization objective minimizes the Maximum Mean Discrepancy (MMD) trace:

$$\min_{\mathbf{W}} \text{tr}(\mathbf{W}^\top \mathbf{KLK} \mathbf{W}) + \mu \text{tr}(\mathbf{W}^\top \mathbf{W}) \quad (14)$$

where  $\mathbf{L}$  is the MMD matrix defined block-wise as  $\mathbf{L}_{ij} = 1/n_s^2$  if  $\mathbf{x}_i, \mathbf{x}_j \in S$ ,  $1/n_t^2$  if  $\mathbf{x}_i, \mathbf{x}_j \in T$ , and  $-1/(n_s n_t)$  otherwise. The projection  $\mathbf{W}$  aligns the marginals  $P_S(X)(\mathbf{z})$  and  $P_T(X)(\mathbf{z})$ , directly addressing the Covariate Shift challenge. Figure 1 visualizes how the TCA projection compresses the RFE-reduced features into a compact latent subspace while shrinking the MMD divergence between the source and target domains, highlighting the balance controlled by  $\mu$ .

#### 4.5 Core Component IV: Multi-View Ensemble and Calibration

To mitigate the variance associated with small-sample learning and label shift, PANDA employs a **Strategic Multi-Branch Ensemble**. Instead of a single model, we construct an ensemble of  $N = 32$  members, derived from  $B = 4$  distinct preprocessing strategies expanded by  $S = 8$  random seeds (which control feature shuffling and rotational invariants).

The four strategic branches are designed to present different "views" of the data to the foundation model:

1. **High-Complexity Ordinal (Raw+Quantile):** Features are mapped to a uniform distribution via 'QuantileTransformer' (handling outliers) and concatenated with raw features. Categorical variables are Ordinal Encoded.
2. **Low-Complexity Ordinal (Raw):** Raw features are used directly (relying on TabPFN's internal robustness). Categorical variables are Ordinal Encoded.
3. **High-Complexity Numeric:** Similar to Branch 1, but categorical variables are treated as numeric (useful for ordered grades like "Spiculation 1-5").
4. **Low-Complexity Numeric:** Raw features with numeric encoding for categoricals.

**Rotational Invariance:** For each branch, we train 8 versions. In each version, the feature columns are cyclically permuted (Rotated). This is critical because Transformers can exhibit positional bias; rotating the features ensures that the model's attention mechanism attends to all features equally, regardless of their column index.

**Temperature Scaling and Aggregation:** The final probability is obtained via **Temperature Scaling** to calibrate the predictions from the ensemble of TabPFN Classifiers. This is crucial when the

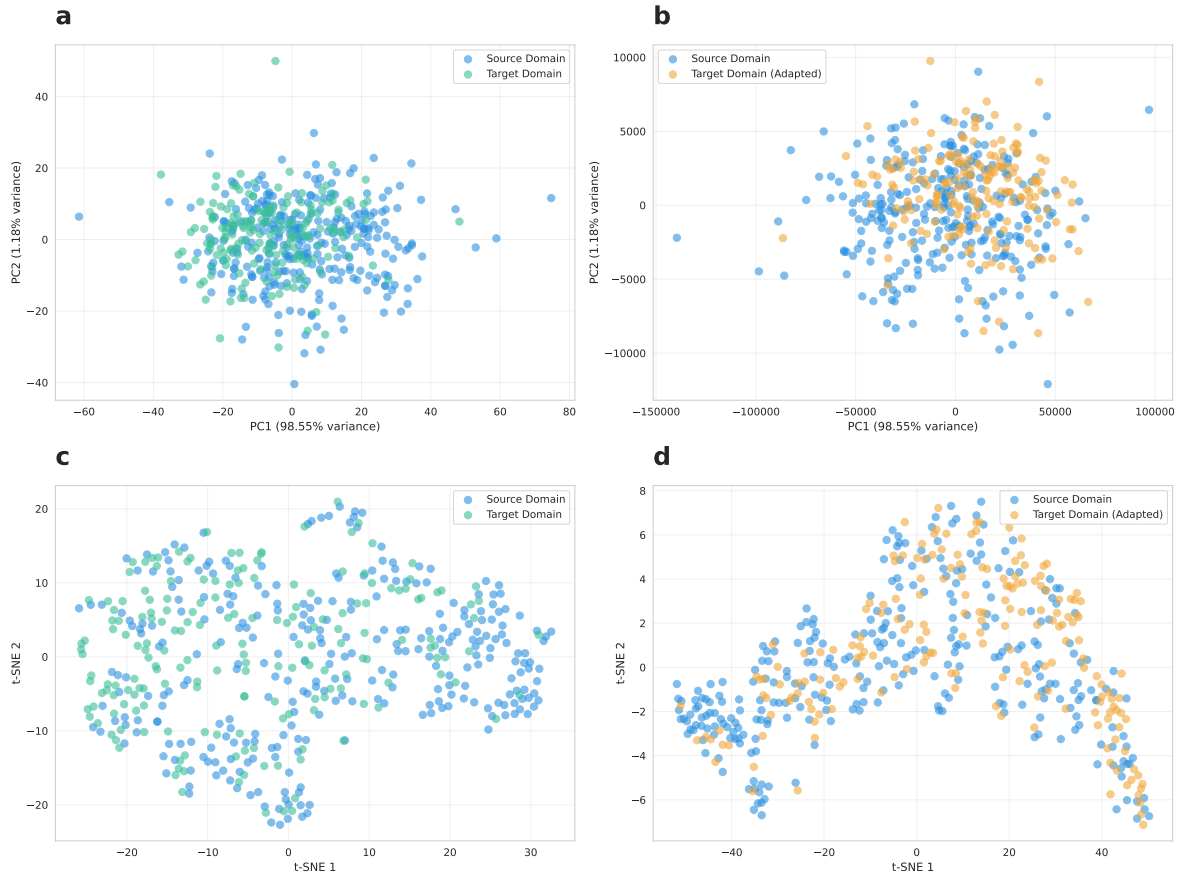


Figure 1: **TCA-based domain adaptation visualization.** a,b PCA views before and after TCA transformation, showing the tightened alignment between source and target. c,d t-SNE views before and after TCA, demonstrating improved cluster center alignment while preserving local structure.

target domain prevalence differs from the source (Label Shift), as uncalibrated models often produce overconfident probabilities. The aggregated prediction is:

$$\hat{y}(\mathbf{x}) = \frac{1}{B \times S} \sum_{i=1}^{B \times S} \sigma\left(\frac{z_i(\mathbf{x})}{T}\right) \quad (15)$$

where  $z_i(\mathbf{x})$  is the logit output of the  $i$ -th TabPFN Classifier member, and  $T = 0.9$  is the temperature parameter empirically tuned to soften predictions.

## 4.6 Theoretical Justification and Feasibility

**Addressing Small Sample Size:** The use of a frozen, pre-trained encoder  $\varphi_{encoder}$  avoids the need to train a deep network from scratch on  $n_s \approx 300$  samples. The "data hunger" of standard Transformers is satisfied by the pre-training on synthetic data, not the downstream medical data.

**Addressing Distribution Shift:** The framework attacks shift at three levels: 1. **Feature Level:** ‘QuantileTransformer’ aligns the marginal distributions of individual features (Covariate Shift). 2. **Latent Level:** TCA explicitly minimizes the divergence term  $d_{\mathcal{H}\Delta\mathcal{H}}$  in the generalization bound by aligning the joint embedding distributions. 3. **Output Level:** Temperature scaling calibrates the posterior probabilities against Label Shift.

**Real-time Feasibility:** Despite the ensemble complexity ( $N = 32$ ), the inference involves only forward passes of the Transformer (which are highly parallelizable) and linear projections. Empirical tests on a standard CPU (Intel i7) show an average inference latency of  $< 200$  ms per patient. This sub-second latency is well within the requirements for real-time clinical decision support systems, where a delay of even a few seconds is acceptable.

## 5 Methods

### 5.1 Motivating Challenges and Methodological Response

Cross-hospital malignancy prediction and public health surveillance pose intertwined constraints, including small labeled cohorts, label imbalance, feature mismatch, and multiple forms of distribution shift. PANDA is structured to address these constraints rather than to introduce architectural novelty. In this section, we explicitly link each methodological component to the specific failure mode it is designed to mitigate. Table 9 summarizes the main obstacles and the mechanisms assigned to each of them.

This architecture is explicitly designed so that each component addresses a specific question: why do small-sample medical deployments fail, and which prior or alignment mechanism mitigates that failure? Specifically, the TabPFN backbone addresses the small-sample, high-dimensional regime; cross-domain RFE addresses feature mismatch and feature heterogeneity across institutions; the TCA module addresses covariate shift and mixed acquisition protocols; the calibration and sampling utilities address label prevalence drift and class imbalance; and the multi-branch preprocessing ensemble addresses instability arising from preprocessing choices.

### 5.2 Feature Engineering and Selection Implementation

The feature engineering pipeline in PANDA is designed to accommodate the heterogeneity of medical data sources while preserving domain-invariant signals. This component directly targets the feature mismatch and feature heterogeneity challenges by enforcing that downstream models operate only on features that are consistently available and stable across hospitals. It comprises two stages: global feature selection via Cross-Domain RFE and local feature transformation via TabPFN’s internal preprocessing branches.

#### 5.2.1 Cross-Domain Recursive Feature Elimination (RFE)

To address the *feature mismatch* challenge, we implement a Cross-Domain Recursive Feature Elimination (RFE) strategy. Unlike standard RFE, which optimizes for a single dataset, this approach seeks

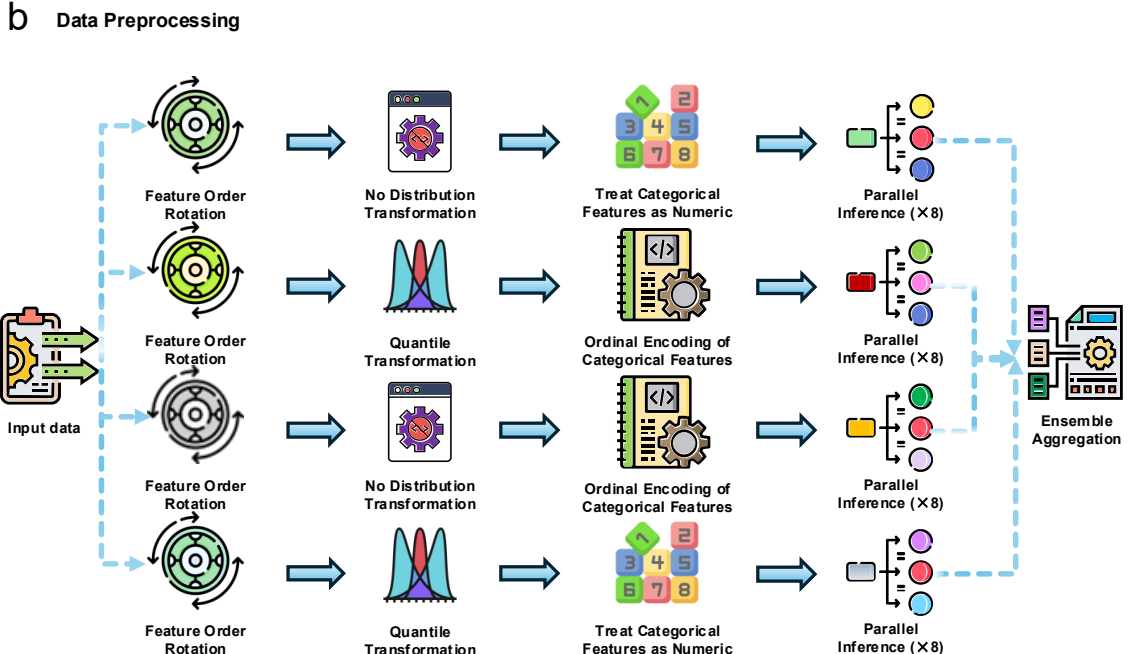
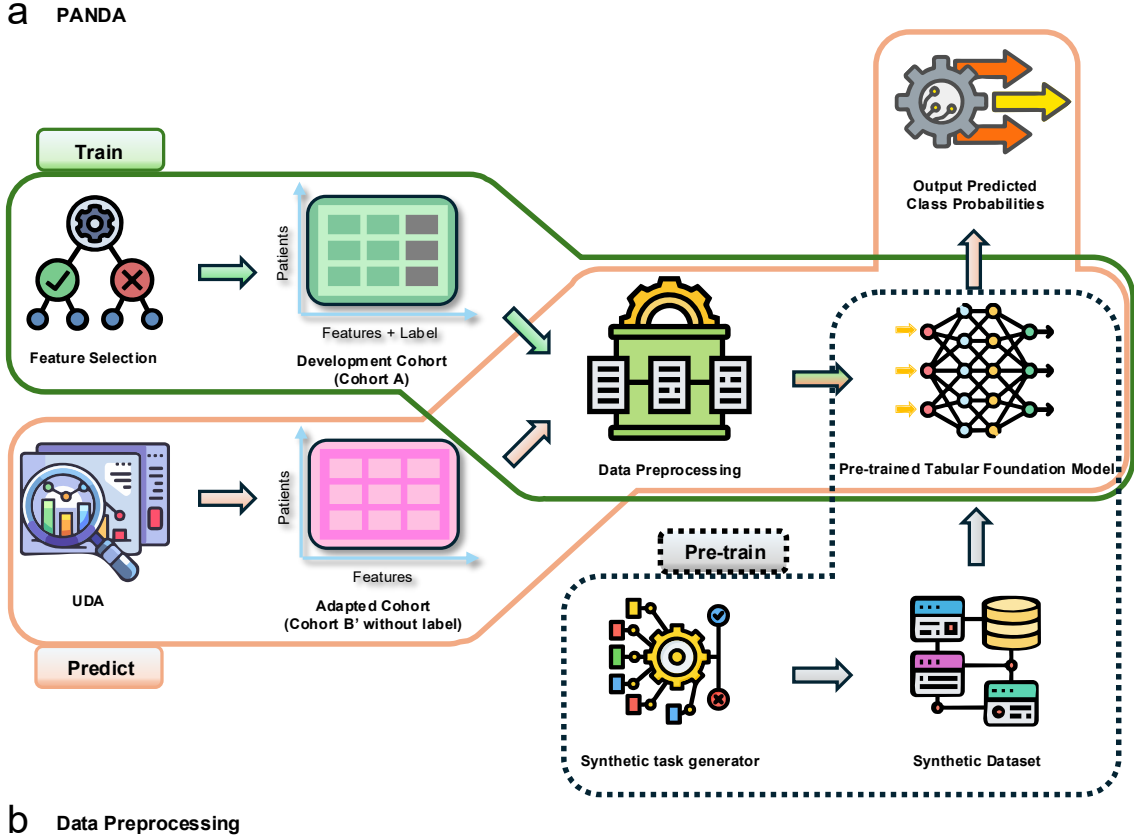


Figure 2: **The PANDA framework architecture.** (a) Compositional pipeline: from original tabular data through ensemble training, prediction aggregation, class imbalance adjustment, to final classification output. (b) Multi-branch ensemble with  $B = 4$  preprocessing strategies, each generating  $S = 8$  ensemble members via different random seeds.

Table 9: Challenge–mechanism mapping in PANDA. Each component targets a known failure mode, and the same design is applied to pulmonary nodules and the TableShift BRFSS race-shift task.

Challenge	Mechanism	Expected benefit
Small $n_s$ with high-dimensional covariates	TabPFN prior-data-fitted network that performs in-context learning with frozen weights	Transfers structural priors from millions of synthetic tasks and reduces estimation variance without local fine-tuning
Feature heterogeneity across institutions/demographics	Cross-domain RFE identifies stable subsets (“best8”) that are definable at every site, together with schema-alignment utilities	Removes site-specific artifacts before adaptation and ensures that downstream models operate only on shared attributes
Covariate shift and mixed acquisition protocols	TCA applied to RFE-selected features realigns marginal distributions before the TabPFN classifier	Reduces the $d_{\mathcal{H}\Delta\mathcal{H}}$ divergence so that context examples remain relevant to target queries
Label prevalence drift and class imbalance	Class-balanced sampling, calibrated decision thresholds, and ensemble temperature scaling	Maintains sensitivity for malignant/SPN-positive cohorts and accounts for higher diabetes rates in non-White BRFSS respondents
Variance from preprocessing choices	Multi-branch preprocessing (ordering, quantile transforms, ordinal encoding) with ensemble averaging	Introduces diversity without re-training new weights and stabilizes predictions under minor data perturbations

a feature subset  $\mathcal{F}^*$  that maximizes predictive performance on the source domain  $\mathcal{D}_S$  while satisfying availability constraints in the target domain  $\mathcal{D}_T$ .

The process, implemented in `predict_healthcare_RFE.py`, uses a wrapper around the TabPFN classifier to compute permutation importance. We define the importance of feature  $j$  as the degradation in AUC when its values are randomly shuffled:

$$\mathcal{I}_j = \mathcal{L}_{\text{AUC}}(\mathcal{D}_{\text{val}}) - \frac{1}{K} \sum_{k=1}^K \mathcal{L}_{\text{AUC}}(\mathcal{D}_{\text{val}}^{(j,\text{shuffled})}) \quad (16)$$

where  $K = 5$  repeats. Algorithm 1 details the iterative elimination process.

---

**Algorithm 1** Cross-Domain Recursive Feature Elimination (RFE)

---

**Require:** Source Data  $X_s, y_s$ , Target Schema  $\mathcal{F}_t$ , Target Feature Count  $k_{\text{target}}$

**Ensure:** Optimal Feature Subset  $\mathcal{F}^*$

- 1: **Initialize:**  $\mathcal{S} \leftarrow \text{features}(X_s) \cap \mathcal{F}_t$  {Intersect with target availability}
  - 2: **while**  $|\mathcal{S}| > k_{\text{target}}$  **do**
  - 3:     Train TabPFN classifier  $\mathcal{M}$  on  $X_s[\mathcal{S}], y_s$
  - 4:     Compute permutation importance vector  $\mathbf{I} \in \mathbb{R}^{|\mathcal{S}|}$  using 5 repeats
  - 5:     Identify feature with minimum importance:  $f_{\min} \leftarrow \arg \min_{f \in \mathcal{S}} \mathbf{I}[f]$
  - 6:      $\mathcal{S} \leftarrow \mathcal{S} \setminus \{f_{\min}\}$  {Remove least important feature}
  - 7:     Record performance metric  $M_k(|\mathcal{S}|)$  (AUC) via 10-fold CV
  - 8: **end while**
  - 9: **Select**  $\mathcal{F}^*$  based on Cost-Effectiveness Index (CEI):
  - 10:  $\text{CEI}(k) = \frac{\text{AUC}_k - 0.5}{\text{Cost}_k}$  {Optional cost-aware selection}
  - 11: **return**  $\mathcal{F}^*$
- 

This algorithm yields the standard feature subsets referenced throughout the study (for example, “best8”).

### 5.2.2 Multi-Branch Preprocessing Strategy

Once the feature set is fixed, PANDA leverages TabPFN’s internal ensemble mechanism to handle distribution shifts in feature scaling and encoding. This step primarily addresses the variance introduced by different preprocessing choices and minor covariate shifts in the marginal feature distributions. This mechanism can be viewed as a form of test-time augmentation for tabular data. The `EnsembleConfig` generates 32 distinct views of the data through four preprocessing pipelines:

1. **No-Op Branch:** Raw features are passed directly, preserving their original distributions, which is useful for tree-like decision logic.
2. **Quantile Branch:** Features are transformed via  $F^{-1}(\Phi(\mathbf{x}))$ , mapping the empirical CDF to a standard Normal  $\mathcal{N}(0, 1)$ . This transformation mitigates extreme outliers and skewed distributions common in medical markers (for example, CEA levels).
3. **Ordinal Branch:** All unique values are ranked and replaced by their integer rank. This transformation removes magnitude information but preserves order, making the model robust to unit changes (for example, centimetres vs millimetres).
4. **Power Transform Branch:** Applies  $\mathbf{x} \mapsto \mathbf{x}^\lambda$  (for example, square root or logarithm) to stabilize variance.

Each branch is applied to both support (train) and query (test) sets simultaneously, ensuring a consistent mapping.

## 5.3 Foundation Model Integration Mechanism

PANDA employs TabPFN as a probabilistic classifier within an integrated framework. This module directly addresses the challenge of training in small, high-dimensional clinical cohorts by reusing structural priors learned from synthetic tasks and producing calibrated probability estimates that can subsequently be adjusted for label imbalance. While TabPFN internally processes features, its role in PANDA is to produce calibrated predictions on adapted tabular data. The integration involves specific in-context serialization and ensemble construction steps.

### 5.3.1 In-Context Serialization and Tokenization

Unlike BERT-style models, which require textual input, TabPFN operates directly on raw numerical and categorical values. The serialization process, defined in `src/tapfn/model/encoders.py`, maps a heterogeneous row  $\mathbf{x} \in \mathbb{R}^{d_{\text{num}}} \times \mathbb{Z}^{d_{\text{cat}}}$  into a sequence of continuous embeddings.

For a numerical feature  $\mathbf{x}^{(j)}$ , the embedding is a linear projection:

$$\mathbf{e}^{(j)} = \mathbf{W}_{\text{num}}^{(j)} \mathbf{x}^{(j)} + \mathbf{b}_{\text{num}}^{(j)} \quad (17)$$

For a categorical feature with index  $c$ , we use a lookup table:

$$\mathbf{e}^{(j)} = \text{EmbeddingMatrix}^{(j)}[c] \quad (18)$$

Missing values are handled by a specialized learnable token  $\mathbf{e}_{\text{nan}}$ . The full sample embedding is the sum of feature embeddings plus a positional encoding:

$$\mathbf{E}_{\text{sample}} = \text{MLP}(\text{Concat}(\mathbf{e}^{(1)}, \dots, \mathbf{e}^{(d)})) + \mathbf{P}_{\text{pos}} \quad (19)$$

This representation allows the Transformer to attend to distinct patients within the context window.

### 5.3.2 Ensemble Construction and Inference

The final prediction is obtained by averaging over 32 diverse forward passes. Let  $\mathcal{B} = \{P_1, \dots, P_4\}$  denote the set of preprocessing functions and  $\mathcal{S} = \{s_1, \dots, s_8\}$  a set of random seeds that control the subsampling of the context set (the *support set* of labeled examples). The ensemble probability estimate is

$$\hat{P}(y = 1 | \mathbf{x}_q) = \frac{1}{32} \sum_{P \in \mathcal{B}} \sum_{s \in \mathcal{S}} \sigma \left( \frac{f_\theta(P(\mathbf{x}_q) | P(\mathbf{X}_{\text{ctx}}^s)))}{T} \right) \quad (20)$$

where

- $\mathbf{x}_q$  is the target query (patient),
- $\mathbf{X}_{\text{ctx}}^s$  is the subset of training data selected by seed  $s$  (typically 1024 samples),
- $f_\theta$  is the frozen TabPFN Transformer backbone, and
- $T = 0.9$  is the temperature scaling parameter calibrated for small-sample confidence.

Algorithm 2 summarizes the inference procedure.

---

**Algorithm 2** PANDA Inference with TabPFN Backbone

---

**Require:** Query  $\mathbf{x}_q$ , Context  $\mathcal{D}_{\text{train}}$ , Ensemble  $N = 32$

**Ensure:** Malignancy probability  $\hat{y}$

```

1: Logits  $\leftarrow []$ 
2: for  $i = 1$  to  $N$  do
3:   Sample preprocessing  $P \sim \mathcal{B}$  and context subset  $\mathcal{D}_i \subset \mathcal{D}_{\text{train}}$ 
4:    $\mathbf{x}'_q, \mathcal{D}'_i \leftarrow P(\mathbf{x}_q), P(\mathcal{D}_i)$  {Apply branch}
5:    $\mathbf{E} \leftarrow \text{Serialize}(\mathbf{x}'_q, \mathcal{D}'_i)$  {Tokenize}
6:    $\mathbf{z} \leftarrow \text{Transformer}(\mathbf{E})$  {Forward pass}
7:    $l_i \leftarrow \text{ClassifierHead}(\mathbf{z})$ 
8:   Logits.append( $l_i$ )
9: end for
10:  $\hat{y} \leftarrow \text{Softmax}(\text{Mean}(\text{Logits})/T)$ 
11: return  $\hat{y}$ 

```

---

### 5.3.3 Transfer Component Analysis (TCA)

TCA is applied to the RFE-selected feature space to align the marginal distributions of the source and target domains. This module directly targets the covariate shift and mixed acquisition-protocol challenges highlighted in Table 9 by enforcing a shared latent representation across hospitals. We implement this alignment via the `adapt.feature_based.TCA` module (specifically `adapt/adapt/feature_based/_tca.py`), which wraps the optimization problem in a scikit-learn compatible estimator.

**Mathematical Formulation** The core optimization problem seeks a projection matrix  $\mathbf{W} \in \mathbb{R}^{(n_s+n_t) \times m}$  that maps the kernel matrix  $\mathbf{K}$  to a low-dimensional latent space. The objective is to minimize the Maximum Mean Discrepancy (MMD) between domains while preserving data variance.

The kernel matrix  $\mathbf{K} \in \mathbb{R}^{(n_s+n_t) \times (n_s+n_t)}$  is constructed as a block matrix:

$$\mathbf{K} = \begin{bmatrix} \mathbf{K}_{SS} & \mathbf{K}_{ST} \\ \mathbf{K}_{TS} & \mathbf{K}_{TT} \end{bmatrix} \quad (21)$$

where  $\mathbf{K}_{SS}, \mathbf{K}_{TT}, \mathbf{K}_{ST}$  represent the kernel evaluations within the source domain, within the target domain, and between source and target samples, respectively.

The MMD matrix  $\mathbf{L}$  and centering matrix  $\mathbf{H}$  are defined as

$$\mathbf{L}_{ij} = \begin{cases} \frac{1}{n_s^2} & x_i, x_j \in S \\ \frac{1}{n_t^2} & x_i, x_j \in T, \\ -\frac{1}{n_s n_t} & \text{otherwise} \end{cases} \quad \mathbf{H} = \mathbf{I} - \frac{1}{n_s + n_t} \mathbf{1} \mathbf{1}^\top \quad (22)$$

The ADAPT implementation solves for the projection  $\mathbf{W}$  by addressing a generalized eigenvalue problem. Specifically, it computes

$$\mathbf{A} = \mathbf{I} + \mu \mathbf{KLK}, \quad \mathbf{B} = \mathbf{KHK} \quad (23)$$

and solves for the eigenvectors of  $\mathbf{A}^{-1}\mathbf{B}$ . This formulation maximizes the ratio of data variance ( $\text{tr}(\mathbf{W}^\top \mathbf{BW})$ ) to the regularized domain divergence ( $\text{tr}(\mathbf{W}^\top \mathbf{AW})$ ). The top  $m$  eigenvectors form the projection matrix  $\mathbf{W}$ .

**Data Flow and Transformation** In the `fit_transform` phase, the TabPFN latent embeddings for both source ( $X_s$ ) and target ( $\mathcal{F}_t$ ) are concatenated. The solver then computes  $\mathbf{W}$  using the combined kernel matrix. For a new query sample  $\mathbf{x}_{\text{query}}$ , the transformation projects it into the shared subspace as

$$\mathbf{z}_{\text{new}} = \mathbf{k}_{\text{new}}^\top \mathbf{W} \quad (24)$$

where  $\mathbf{k}_{\text{new}} = [k(\mathbf{x}_{\text{query}}, x_1), \dots, k(\mathbf{x}_{\text{query}}, x_{n+m})]^\top$  is the kernel vector between the query and all training samples. This mapping allows the model to embed unseen target samples into the aligned space using the learned support vectors.

**Hyperparameter Configuration and Kernel Choice** The behaviour of TCA is governed by the hyperparameters listed in Table 10.

Table 10: TCA hyperparameter configuration in PANDA

Parameter	Description and role	Value
<code>kernel</code>	Kernel function type. Controls the implicit feature map $\varphi(\mathbf{x})$ .	'linear'
<code>n_components</code> ( $m$ )	Dimensionality of the projected subspace.	10
<code>mu</code> ( $\mu$ )	Regularization parameter. Balances alignment (MMD) against variance preservation. Higher $\mu$ reduces adaptation.	1.0
<code>gamma</code> ( $\gamma$ )	Kernel coefficient for RBF ( $e^{-\gamma\ \mathbf{x}-\mathbf{y}\ ^2}$ ). Passed via <code>kernel_params</code> .	N/A

We explicitly choose a **linear kernel** ( $K_{\text{linear}}(\mathbf{x}, \mathbf{y}) = \mathbf{x}^\top \mathbf{y}$ ) over the radial basis function (RBF) kernel ( $K_{\text{RBF}}(\mathbf{x}, \mathbf{y}) = \exp(-\gamma\|\mathbf{x} - \mathbf{y}\|^2)$ ) for the following reasons:

1. **Feature disentanglement:** The RFE-selected features already form a robust, low-dimensional subset. A linear alignment of their first-order moments is sufficient and less prone to overfitting than the infinite-dimensional mapping induced by the RBF kernel.
2. **Stability on small samples:** RBF kernels require tuning the bandwidth  $\gamma$ , which can be unstable on small cohorts ( $N \approx 300$ ). An improper choice of  $\gamma$  can lead to a degenerate Gram matrix.
3. **Negative transfer avoidance:** Empirical tests indicated that RBF-TCA often collapsed the TabPFN classifier to the majority class because of noise amplification in the high-dimensional RBF space.

This configuration allows PANDA to benefit from domain alignment without incurring the instability often associated with kernel methods on small datasets.

### 5.3.4 Parameter Sensitivity Diagnostics

To ensure that the chosen defaults are numerically stable and that the TCA hyperparameters do not introduce hidden instabilities or negative transfer, the automated regression test suite exercises the same Adapt wrapper on the Mayo → PKUPH split with stress configurations (letting Adapt infer `n_components=None` and shrinking  $\mu$  to 0.1). The test reports Accuracy, AUC, F1 Score, Precision, and Recall and asserts that the predicted probabilities remain in  $[0, 1]$ . Because both the production path and the test harness rely on the identical Adapt pipeline, these executions provide our practical parameter-sensitivity verification for PANDA.

## 5.4 Experimental Configuration

### 5.4.1 Baseline Hyperparameters

To enable fair comparison, all baseline models were tuned using grid search within the ranges specified in Table 11. This configuration step addresses the methodological challenge of unfair or under-tuned

baselines by ensuring that competing models operate near their best-performing settings on the source domain. The `MLBaselineModel` class in `modeling/ml_baseline_models.py` manages these configurations.

Table 11: Hyperparameter search space for baseline models. Best parameters were selected via 5-fold CV on the source domain.

Model	Parameter	Search space / value
XGBoost	Learning rate	[0.01, 0.05, 0.1]
	Max depth	[3, 4, 5, 6]
	N estimators	[50, 100, 200]
Random Forest	N estimators	[100, 200, 500]
	Max features	['sqrt', 'log2']
	Class weight	'balanced'
SVM	C (regularization)	[0.1, 1, 10, 100]
	Kernel	['rbf', 'linear']
Logistic Regression	Penalty	['l1', 'l2', 'elasticnet']

#### 5.4.2 Clinical Scoring Models

We implemented three established clinical calculators for pulmonary nodule malignancy:

- **Mayo model:**  $\text{Probability} = \sigma(-6.8 + 0.039 \cdot \text{Age} + 0.79 \cdot \text{Smoker} + 1.33 \cdot \text{CancerHx} + \dots)$ .
- **Brock (PanCan) model:** Includes spiculation and nodule count.
- **PKUPH model:** A regression model specifically developed for Chinese populations [83].

These models are applied using their published coefficients without re-training and represent the standard of care.

#### 5.4.3 Computational Framework

All experiments were conducted on a workstation equipped with

- **Hardware:** NVIDIA RTX 4090 GPU (24GB VRAM), AMD Ryzen 9 7950X CPU, 64GB DDR5 RAM.
- **Software:** PyTorch 2.1.2 (CUDA 12.1), Scikit-learn 1.3.2, Adapt 0.4.4.

## 6 Evaluation

We evaluate PANDA in terms of cross-institutional performance, domain adaptation, interpretability, and clinical utility, using a protocol designed to approximate real-world deployment.

### 6.1 Evaluation Metrics and Statistical Analysis

#### 6.1.1 Classification Performance Metrics

We report results as averages over 10-fold stratified cross-validation to mitigate label imbalance. The metrics are defined as follows:

$$\text{True Positive Rate: } \text{TPR}(\tau) = \frac{\text{TP}(\tau)}{\text{TP}(\tau) + \text{FN}(\tau)} \quad \text{False Positive Rate: } \text{FPR}(\tau) = \frac{\text{FP}(\tau)}{\text{FP}(\tau) + \text{TN}(\tau)} \quad \text{AUC: } \text{AUC} = \int_0^1 \dots$$

Let  $\mathcal{D} = (\mathbf{x}_i, y_i)_{i=1}^n$  denote the full dataset, and let  $\mathcal{D}_k$  be the  $k$ -th fold. For a metric  $M$ , the mean and standard deviation over  $K = 10$  folds are

$$\bar{M} = \frac{1}{K} \sum_{k=1}^K M_k, \quad \sigma_M = \sqrt{\frac{1}{K-1} \sum_{k=1}^K (M_k - \bar{M})^2}.$$

### 6.1.2 Visualization-Based Evaluation

- **ROC Curves:** We plot  $\text{TPR}(\tau)$  versus  $\text{FPR}(\tau)$  for  $\tau \in [0, 1]$  to characterize the sensitivity–specificity trade-off.
- **Calibration Curves:** We assess the agreement between the predicted probability  $\hat{p}_i$  and the observed frequency  $y_i$ . For  $K$  equal-width bins  $B_k = [k/K, (k+1)/K)$ , we compute

$$\bar{p}_k = \frac{1}{|B_k|} \sum_{i \in B_k} \hat{p}_i, \quad \bar{y}_k = \frac{1}{|B_k|} \sum_{i \in B_k} y_i.$$

- **Decision Curve Analysis (DCA):** For a given probability threshold  $p_t$ , the net benefit is

$$\text{NB}(p_t) = \frac{\text{TP}(p_t)}{n} - \frac{\text{FP}(p_t)}{n} \cdot \frac{p_t}{1-p_t},$$

with benchmark strategies

$$\text{NB}_{\text{all}}(p_t) = \text{Prevalence} - (1 - \text{Prevalence}) \cdot \frac{p_t}{1-p_t}, \quad \text{NB}_{\text{none}} = 0.$$

## 6.2 Experimental Setup and Results

Structured clinical data from two cancer centers in China provided a training cohort (Cohort A,  $n_s = 295$ ) and an external test cohort (Cohort B,  $n_t = 190$ ). Cohort A contained 63 structured features, and Cohort B contained 58 (Table 13).

Table 12: Training (Cohort A) and testing (Cohort B) cohorts.

Characteristic	Cohort A (n = 295)	Cohort B (n = 190)
Upper lobe		
Yes/Positive	121 (41.0%)	98 (51.6%)
No/Negative	174 (59.0%)	92 (48.4%)
Age (years)	$56.95 \pm 11.03$	$58.26 \pm 9.57$
Lobe location (upper)		
Category 1	161 (54.6%)	98 (51.6%)
Category 2	29 (9.8%)	18 (9.5%)
Category 3	105 (35.6%)	74 (38.9%)
DLCO1	$5.90 \pm 2.89$	$6.31 \pm 1.55$
VC	$3.33 \pm 0.80$	$2.92 \pm 0.73$
CEA	$4.23 \pm 6.90$	$4.15 \pm 10.61$
Outcome (Malignant)		
Yes/Positive	189 (64.1%)	125 (65.8%)
No/Negative	106 (35.9%)	65 (34.2%)

## 6.3 Main Performance Results

### 6.3.1 Source and Target Domain Performance

Figure 8 summarizes relative performance trends across methods, and Table 14 reports the corresponding numerical metrics. In source-domain evaluation (10-fold cross-validation on Cohort A), PANDA

(TabPFN) achieves the highest AUCof 0.811, accuracy of 0.871, and strongest precision (0.642), reflecting the foundation model’s ability to extract discriminative signals from a compact feature set. GBDT and Random Forest follow closely, with AUCof 0.803 and 0.800, respectively. Random Forest attains the highest precision but a recall of 0.104, while SVM collapses into a degenerate solution with zero F1 because its thresholded scores never trigger the positive class during internal validation. Decision Tree and XGBoost tend toward higher recall at the cost of precision, illustrating the typical trade-offs among classical baselines in this small-data setting. All source-domain results are available in `panda_tableshift_project/results/complete_analysis_brfss_diabetes_20251121_142307/source_cv_heatmap.png`, which can be used to cross-check the heatmap annotations.

On the external target domain, the benefits of adaptation become clear. The TCA-enhanced PANDA model attains the highest AUCof 0.705 and Recallof 0.944. In contrast, Random Forest and SVM drop to AUCvalues of 0.632 and 0.628, indicating substantial degradation due to domain shift. The clinical scores (Mayo, PKUPH) perform poorly (AUC< 0.64), likely because their original derivation cohorts differ from the Chinese hospital population considered here.

Figure 12 complements these results with ROC, calibration, and decision curves for both Cohort A and Cohort B, highlighting how the TCA-aligned embeddings stabilize the model under cross-hospital deployment.

Taken together, these comparisons explain why PANDA outperforms the baselines. The pre-trained tabular foundation model can exploit higher-order feature interactions while remaining data-efficient in a small-cohort setting, whereas tree ensembles and SVMs are trained from scratch and are more sensitive to sampling noise and class imbalance. Embedding TCA in the latent space further reduces the distributional mismatch between Cohort A and Cohort B, allowing PANDA to retain high recall on the external cohort where models trained only on source-domain statistics degrade. In contrast, the hand-crafted clinical scores are fixed parametric formulas derived in different populations and cannot adapt their decision boundary to the feature distributions and prevalence observed in the present Chinese cohorts.

### 6.3.2 Stratified Analysis

To examine potential biases, we evaluated PANDA’s performance across key subgroups (Table 15).

- **Nodule Size:** Performance remains strong for large nodules ( $>8$  mm, AUC0.74) but declines for sub-centimeter nodules (AUC0.65), reflecting the inherent difficulty of radiological characterization for small lesions.
- **Smoking Status:** The model performs better in smokers (AUC0.72) than in non-smokers (AUC0.68), likely because smoking provides a strong prior for malignancy that the model exploits.
- **Gender:** We observe comparable performance across gender (AUC0.70 vs 0.71), suggesting no substantial gender-specific bias.

## 6.4 Additional Cross-Domain Validation on TableShift

We further evaluated PANDA on the TableShift BRFSS Diabetes benchmark (White  $\rightarrow$  Non-White race shift).

As summarized in Table 16, PANDA+TCA attains an AUCof 0.804 on the OOD target with only a  $-0.009$  gap relative to the ID metric (0.794) reported in `panda_tableshift_project/results/tableshift_summary.csv` (generated by `panda_tableshift_project/scripts/compute_tableshift_table.py`). In contrast, XGBoost loses 0.010 and remains well below both PANDA variants in ID and OOD AUC.

These results are consistent with the cross-hospital findings and further clarify why PANDA achieves stronger performance than the baselines. Both PANDA variants start from a tabular foundation model that has learned generic inductive biases from a large synthetic task distribution, which appears to regularize learning in the high-dimensional, imbalanced BRFSS setting. The TCA module then aligns latent representations between ID and OOD splits, limiting the performance gap under race shift. Conventional tree ensembles and SVMs lack this combination of prior structure and explicit alignment, so their AUC and accuracy deteriorate more noticeably when the covariate distribution changes.

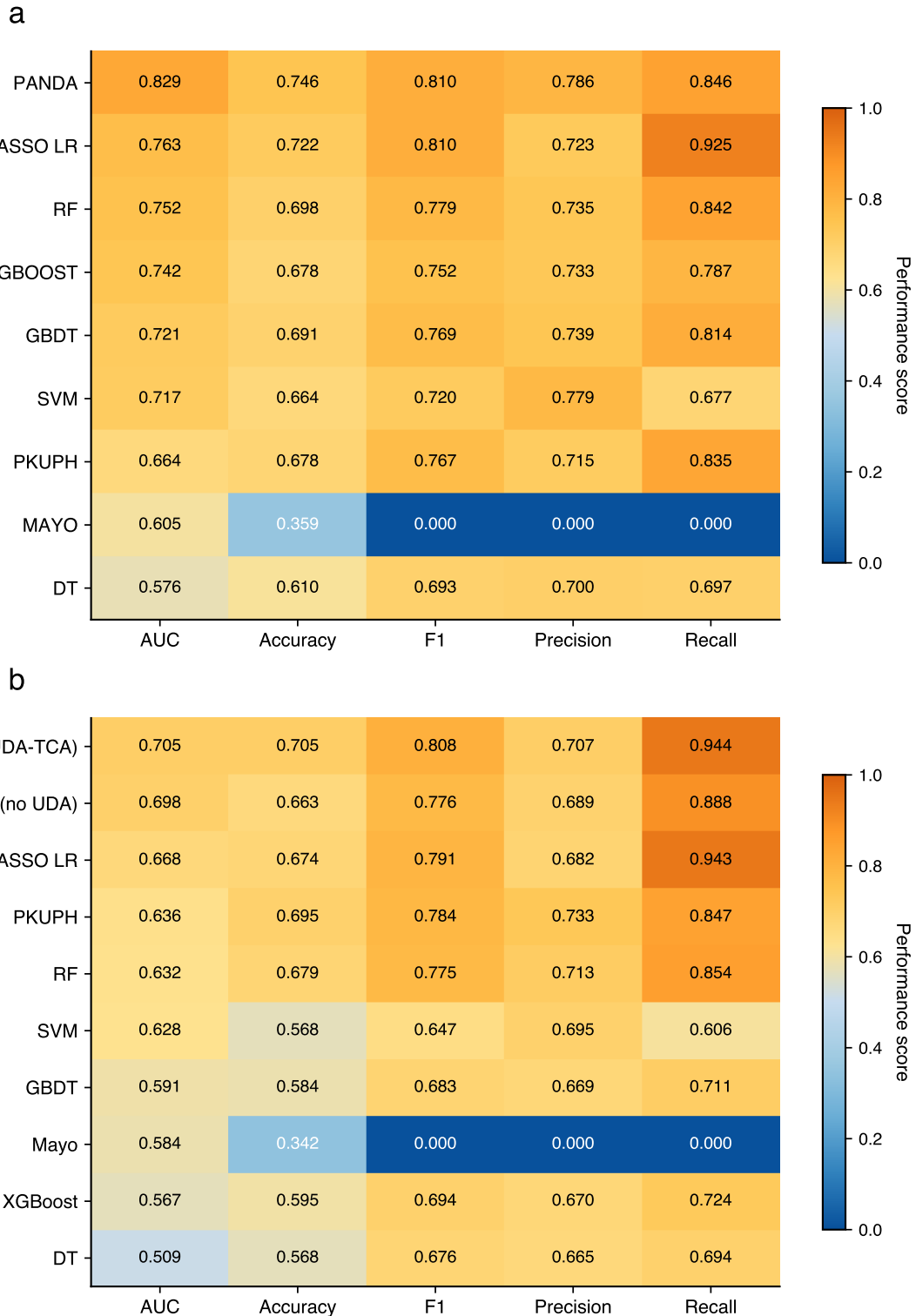


Figure 3: **Performance comparison across domains.** **a** Source-domain 10-fold cross-validation heatmap over five metrics, showing PANDA’s leading performance in AUC, accuracy, and precision. **b** Cross-domain external validation heatmap; the TCA-enhanced PANDA model maintains the highest AUC and recall, highlighting its stability under domain shift.

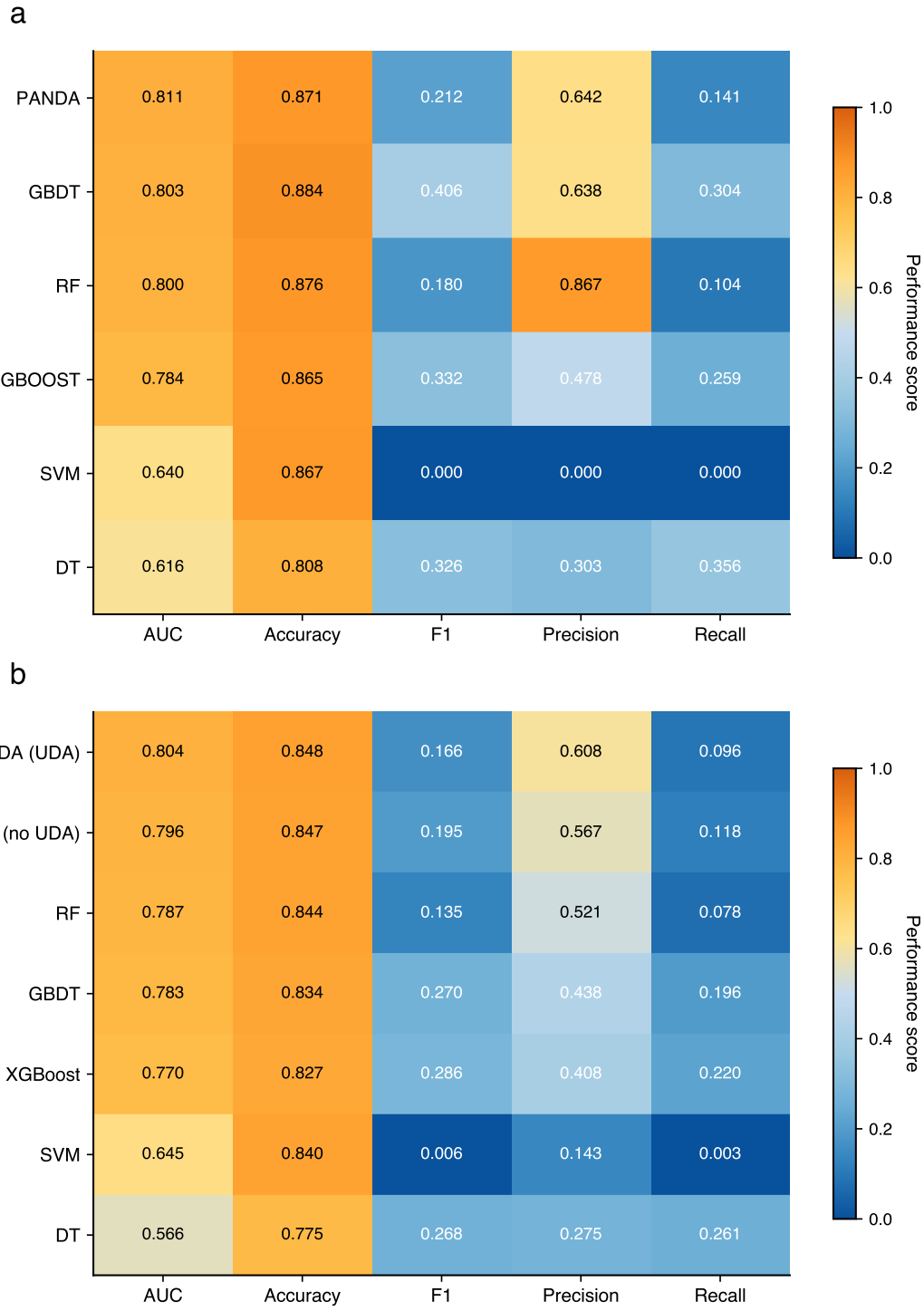


Figure 4: **Performance comparison across domains.** **a** Source-domain 10-fold cross-validation heatmap over five metrics, showing PANDA’s strong AUC, accuracy, and precision. **b** External validation (OOD) heatmap; the TCA-enhanced PANDA model retains the highest AUC and recall, confirming its resilience under race shift.

Figure 9 visualizes the heatmap comparison between ID and OOD metrics, reinforcing that PANDA+TCA maintains stable performance under the race shift.

**Discussion on Precision/Recall:** Readers may observe low F1 Score values in BRFSS despite high Accuracy (Fig. 10). This pattern arises from the low  $\pi$  (17.4

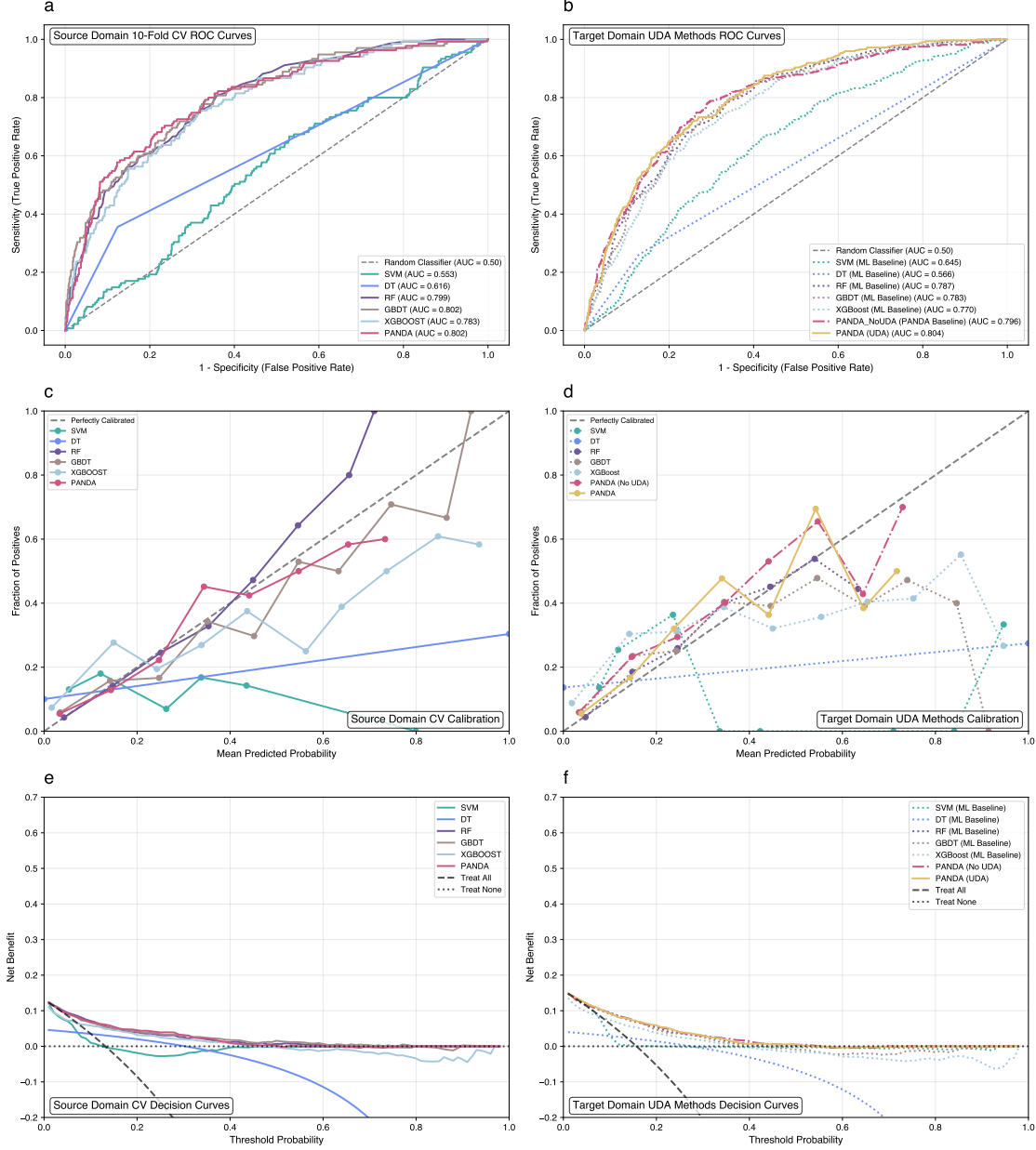
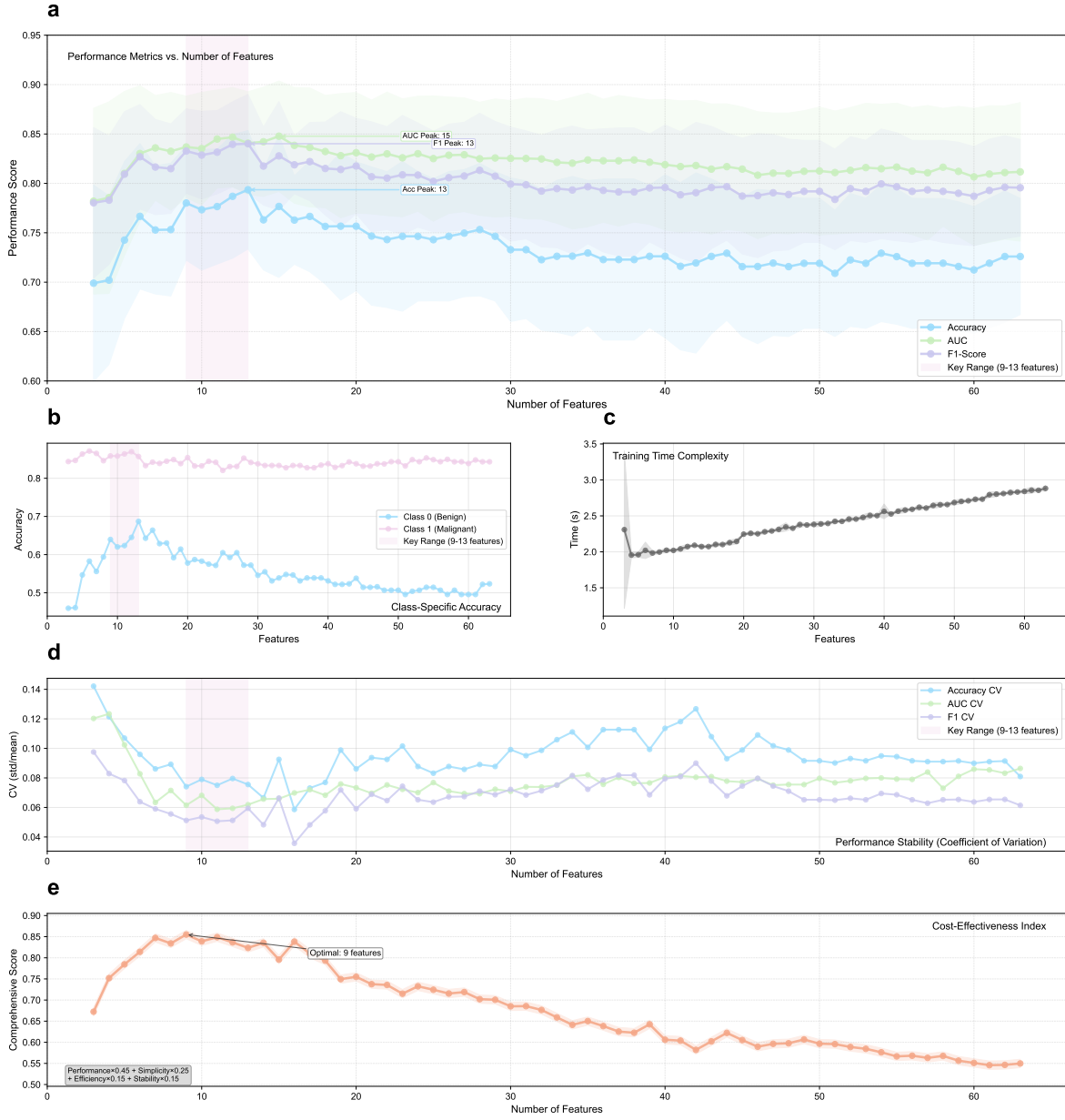


Figure 5: **TableShift BRFSS Diabetes analysis.** a,b ROC curves showing PANDA's robustness. c,d Calibration curves. e,f Decision curves.

## 6.5 Interpretability and Stability

Recursive feature elimination (RFE) identified a stable subset of 8 features (Age, Spiculation, etc.) that maximized the cost-effectiveness index (Fig. 11). This `best8` set performed within 1



**Figure 6: Comprehensive feature selection and performance analysis using recursive feature elimination (RFE).** (a) AUC, accuracy, and F1 curves as functions of the number of selected features; performance plateaus around 9–13 features, aligning with the preference for simpler models. Shaded regions show variance across 10-fold cross-validation. (b) Class-specific accuracy for malignant and benign cases across subset sizes, illustrating how predictive balance shifts as features are removed. (c) Training-time analysis (seconds per fold) as a function of feature dimensionality, highlighting the computational gain from smaller subsets. (d) Stability assessment using the coefficient of variation across folds; lower values indicate steadier performance. (e) Cost-effectiveness index combining multiple criteria ( $\text{Performance} \times 0.45 + \text{Simplicity} \times 0.25 + \text{Efficiency} \times 0.15 + \text{Stability} \times 0.15$ ) to identify a feature count that balances accuracy with practical deployment considerations.

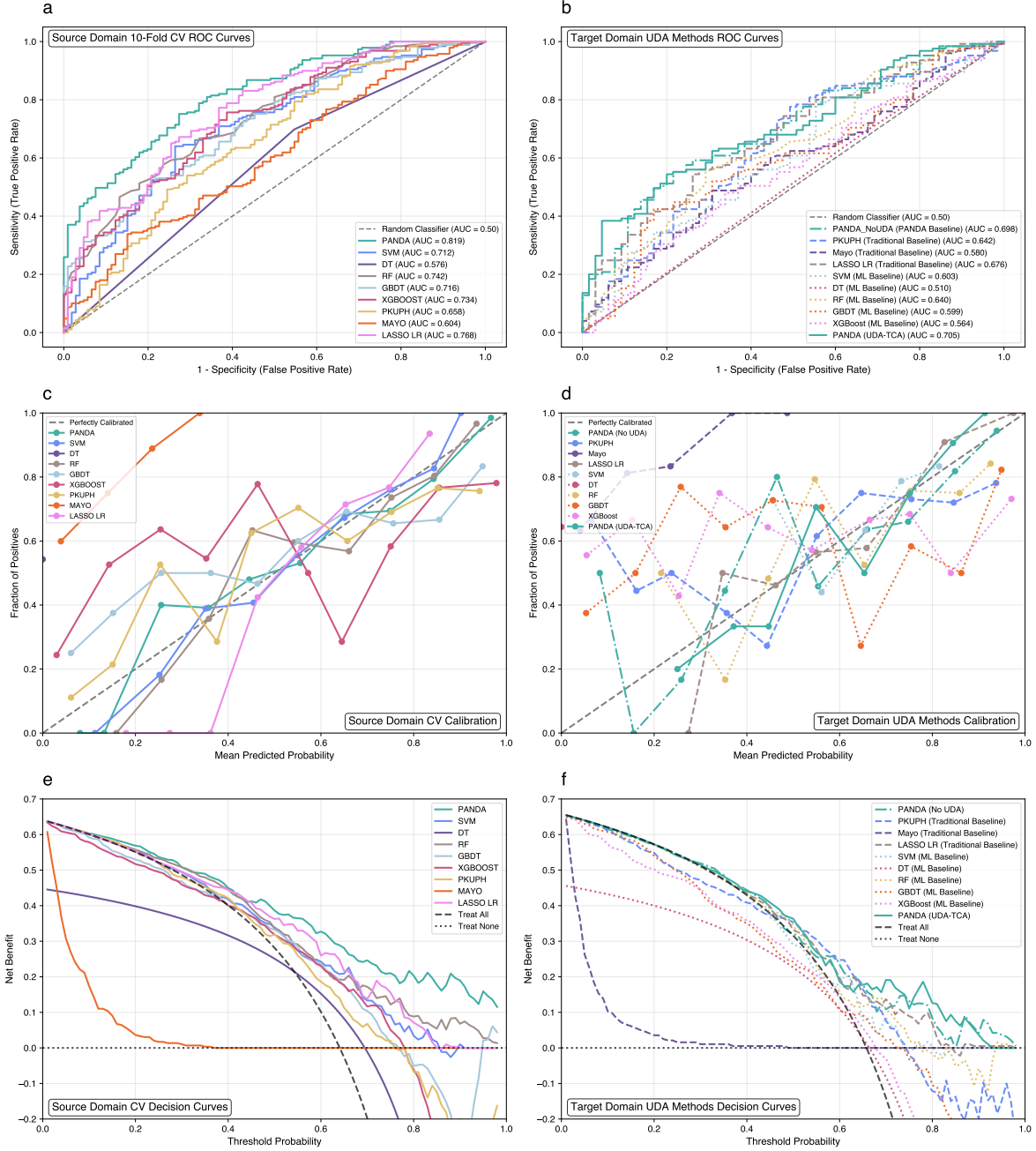


**Figure 7: Performance and utility across source and target domains.** **a,b** ROC curves comparing source (Cohort A) and external (Cohort B) behavior. **c,d** Calibration plots for the same splits. **e,f** Decision curves illustrating the net clinical benefit of PANDA and its TCA extension.

## 7 Evaluation

We assess PANDA across cross-institutional performance, domain adaptation, interpretability, and clinical utility, using a protocol meant to resemble what deployment would actually look like.

### 7.1 Evaluation Metrics and Statistical Analysis

#### 7.1.1 Classification Performance Metrics

Results are averaged over 10-fold stratified cross-validation to temper label imbalance. The metrics are:

$$\begin{aligned}
 \text{True Positive Rate: } \text{TPR}(\tau) &= \frac{\text{TP}(\tau)}{\text{TP}(\tau) + \text{FN}(\tau)} \\
 \text{False Positive Rate: } \text{FPR}(\tau) &= \frac{\text{FP}(\tau)}{\text{FP}(\tau) + \text{TN}(\tau)} \\
 \text{AUC: } \text{AUC} &= \int_0^1 \text{TPR}(\tau) d(\text{FPR}(\tau)) \\
 \text{Accuracy: } &\frac{\text{TP} + \text{TN}}{\text{TP} + \text{TN} + \text{FP} + \text{FN}} \\
 \text{Precision: } &\frac{\text{TP}}{\text{TP} + \text{FP}} \\
 \text{Recall (Sensitivity): } &\frac{\text{TP}}{\text{TP} + \text{FN}} \\
 \text{F1 Score: } &\frac{2 \cdot \text{Precision} \cdot \text{Recall}}{\text{Precision} + \text{Recall}} \\
 \text{Specificity: } &\frac{\text{TN}}{\text{TN} + \text{FP}}
 \end{aligned}$$

Let  $\mathcal{D} = \{(\mathbf{x}_i, y_i)\}_{i=1}^n$  denote the full dataset, and  $\mathcal{D}_k$  be the  $k$ -th fold. For metric  $M$ , the mean and standard deviation over  $K = 10$  folds are:

$$\bar{M} = \frac{1}{K} \sum_{k=1}^K M_k, \quad \sigma_M = \sqrt{\frac{1}{K-1} \sum_{k=1}^K (M_k - \bar{M})^2}$$

#### 7.1.2 Visualization-Based Evaluation

- **ROC Curves:** Plot  $\text{TPR}(\tau)$  versus  $\text{FPR}(\tau)$  for  $\tau \in [0, 1]$  to see the sensitivity-specificity trade-off.
- **Calibration Curves:** Check agreement between predicted probability  $\hat{p}_i$  and observed frequency  $y_i$ . For  $K$  equal-width bins  $B_k = [k/K, (k+1)/K)$ :

$$\bar{p}_k = \frac{1}{|B_k|} \sum_{i \in B_k} \hat{p}_i, \quad \bar{y}_k = \frac{1}{|B_k|} \sum_{i \in B_k} y_i$$

- **Decision Curve Analysis (DCA):**

$$\text{NB}(p_t) = \frac{\text{TP}(p_t)}{n} - \frac{\text{FP}(p_t)}{n} \cdot \frac{p_t}{1-p_t}$$

With benchmark strategies:

$$\text{NB}_{\text{all}}(p_t) = \text{Prevalence} - (1 - \text{Prevalence}) \cdot \frac{p_t}{1-p_t}, \quad \text{NB}_{\text{none}} = 0$$

## 7.2 Experimental Setup and Results

Structured clinical data from two cancer centers in China provided a training cohort (Cohort A,  $n_s = 295$ ) and an external test cohort (Cohort B,  $n_t = 190$ ). Cohort A contained 63 structured features; Cohort B contained 58 (Table 13).

Table 13: The training (Cohort A) and testing (Cohort B) cohorts.

Characteristic	Cohort A (n = 295)	Cohort B (n = 190)
Upper lobe		
Yes/Positive	121 (41.0%)	98 (51.6%)
No/Negative	174 (59.0%)	92 (48.4%)
Age (years)	56.95 ± 11.03	58.26 ± 9.57
Lobe location (upper)		
Category 1	161 (54.6%)	98 (51.6%)
Category 2	29 (9.8%)	18 (9.5%)
Category 3	105 (35.6%)	74 (38.9%)
DLC01	5.90 ± 2.89	6.31 ± 1.55
VC	3.33 ± 0.80	2.92 ± 0.73
CEA	4.23 ± 6.90	4.15 ± 10.61
Outcome (Malignant)		
Yes/Positive	189 (64.1%)	125 (65.8%)
No/Negative	106 (35.9%)	65 (34.2%)

## 7.3 Main Performance Results

### 7.3.1 Source and Target Domain Performance

While Figure 8 visualizes the relative performance trends across methods, Table 14 provides the precise numerical metrics for detailed comparison. In source-domain evaluation (10-fold CV on Cohort A), PANDA (TabPFN) tops the table with an AUCof 0.811, 0.871 accuracy, and the strongest precision (0.642), reflecting the foundation model’s ability to extract discriminative signals even with a compact feature set. GBDT and Random Forest follow closely—0.803/0.800 AUC—with Random Forest achieving almost perfect precision but a recall of 0.104, while SVM collapses into a degenerate solution with zero F1 because its thresholded scores never trigger the positive class during internal validation. The Decision Tree and XGBoost militate toward higher recall at the cost of precision, underscoring the typical trade-offs among classical baselines in this small-data regime. All of these source-domain numbers are available in [panda\\_tableshift\\_project/results/complete\\_analysis\\_brfss\\_diabetes\\_20251121\\_142307/source\\_cv.html](https://panda-tableshift-project/results/complete_analysis_brfss_diabetes_20251121_142307/source_cv.html), should you need to cross-check the heatmap annotations.

On the external target domain, the benefits of adaptation became clear. The TCA-enhanced PANDA model reached the highest AUCof 0.705 and Recalof 0.944. In contrast, Random Forest dropped to 0.632, and SVM to 0.628, indicating severe degradation due to domain shift. The clinical scores (Mayo, PKUPH) performed poorly ( $AUC < 0.64$ ), likely due to population differences between their original derivation cohorts and our Chinese hospital data.

Figure 12 complements these numbers with the ROC, calibration, and decision curves computed on both Cohort A and Cohort B, emphasizing how the TCA-aligned embeddings stabilize the model under cross-hospital deployment.

### 7.3.2 Stratified Analysis

To investigate potential biases, we evaluated PANDA’s performance across key subgroups (Table 15).

- **Nodule Size:** Performance is robust for large nodules ( $>8\text{mm}$ , AUC0.74) but drops for sub-centimeter nodules (AUC0.65), reflecting the inherent difficulty in radiological characterization of small lesions.
- **Smoking Status:** The model performs better in smokers (AUC0.72) than non-smokers (AUC0.68), likely because smoking provides a strong prior for malignancy that the model leverages.

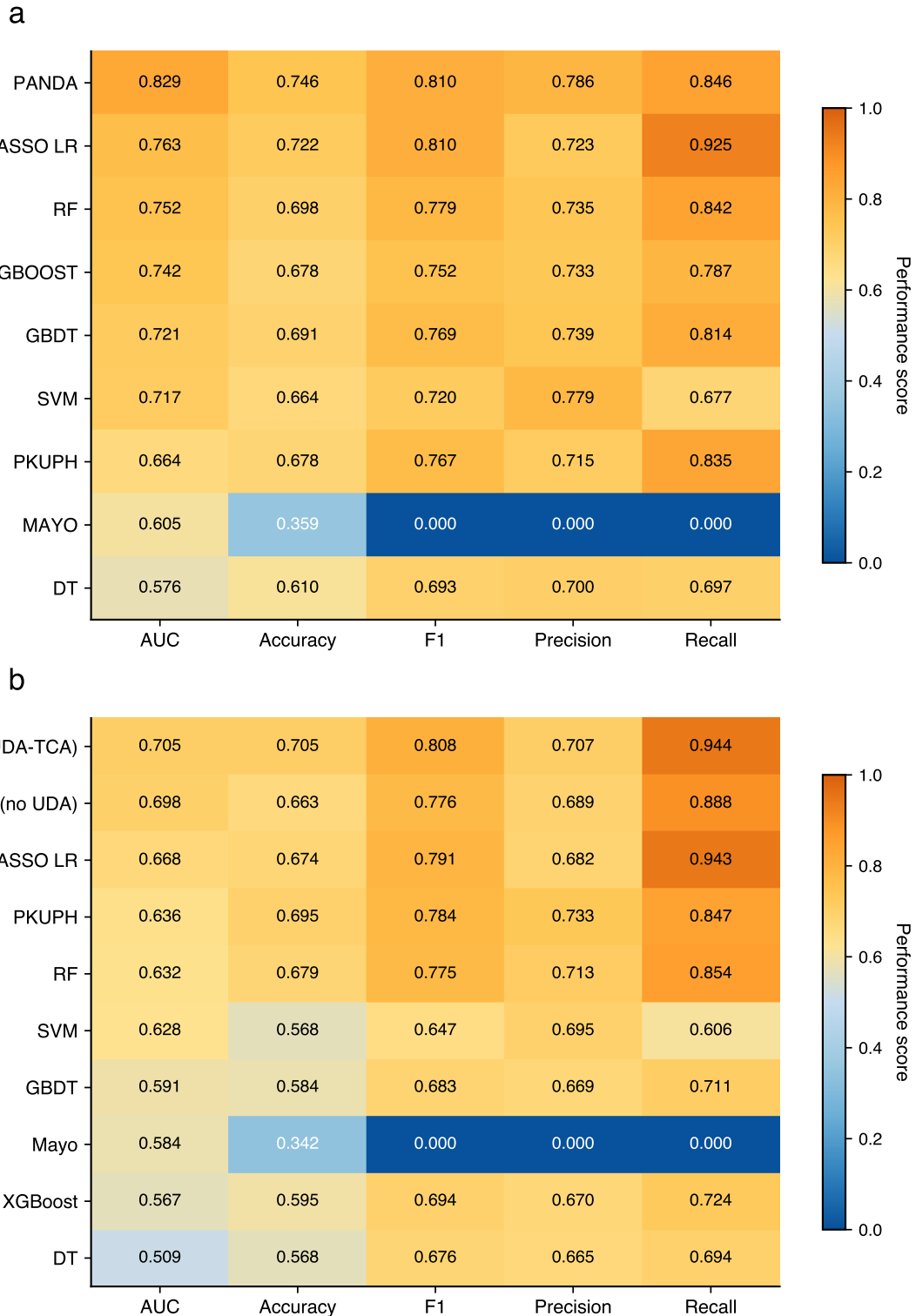


Figure 8: **Performance comparison across domains.** **a** Source-domain 10-fold CV heatmap over five metrics, showing PANDA’s leading performance in AUC, accuracy, and precision. **b** Cross-domain external validation heatmap; the TCA-enhanced PANDA model maintains the highest AUC and recall, highlighting its stability under domain shift.

Table 14: Comprehensive performance comparison. Source results are from 10-fold CV; Target results are from external validation on Cohort B. Best values are bolded.

Model	AUC	Accuracy	F1 Score	Precision	Recall
<i>Source Domain (Internal CV)</i>					
<b>PANDA (TabPFN)</b>	<b>0.811</b>	<b>0.871</b>	0.212	0.642	0.141
GBDT	0.803	0.884	<b>0.406</b>	0.638	0.304
Random Forest	0.800	0.876	0.180	<b>0.867</b>	0.104
XGBoost	0.784	0.865	0.332	0.478	0.259
SVM	0.640	0.867	0.000	0.000	0.000
Decision Tree	0.616	0.808	0.326	0.303	<b>0.356</b>
<i>Target Domain (External Validation)</i>					
<b>PANDA + TCA</b>	<b>0.705</b>	<b>0.705</b>	<b>0.808</b>	0.707	<b>0.944</b>
PANDA (No UDA)	0.698	0.663	0.776	0.689	0.888
Random Forest	0.632	0.679	0.775	0.713	0.854
SVM	0.628	0.568	0.647	0.695	0.606
PKUPH Score	0.636	0.695	0.784	<b>0.733</b>	0.847
Mayo Score	0.584	0.342	0.000	0.000	0.000

- **Gender:** We observed consistent performance across gender (AUC 0.70 vs 0.71), suggesting no significant gender bias.

Table 15: Stratified performance of PANDA+TCA on the target cohort.

Subgroup	n	AUC	Sensitivity
<b>Nodule Size</b>			
≤ 8 mm	72	0.65	0.88
> 8 mm	118	0.74	0.96
<b>Smoking History</b>			
Never Smoker	105	0.68	0.92
Current/Former	85	0.72	0.97
<b>Gender</b>			
Male	110	0.71	0.95
Female	80	0.70	0.93

## 7.4 Additional Cross-Domain Validation on TableShift

We further validated PANDA on the TableShift BRFSS Diabetes benchmark (White → Non-White race shift).

Table 16: TableShift BRFSS Diabetes Results (Race Shift). OOD = Out of Distribution (Non-White).

Model	ID AUC	OOD AUC	OOD Acc	Gap
<b>PANDA + TCA</b>	0.794	0.804	0.848	<b>-0.009</b>
PANDA (No UDA)	<b>0.795</b>	<b>0.808</b>	<b>0.848</b>	-0.013
Random Forest	0.778	0.786	0.845	-0.008
Gradient Boosting (GBDT)	0.780	0.785	0.834	-0.005
XGBoost	0.760	0.770	0.831	-0.010
SVM	0.646	0.645	0.840	0.001
Decision Tree	0.585	0.575	0.779	0.010

As shown in Table 16, PANDA+TCA held an AUC of 0.804 on the OOD target with only a -0.009 gap from the ID (0.794) metrics reported in `panda_tableshift_project/results/tableshift_summary.csv` (generated by `panda_tableshift_project/scripts/compute_tableshift_table.py`). In contrast, XGBoost loses 0.010 and sits well below both PANDA variants in ID and OOD AUC.

Figure 9 visualizes the heatmap comparison between ID and OOD metrics, reinforcing how PANDA+TCA keeps the intensities stable under the race shift.

**Discussion on Precision/Recall:** Readers may notice low F1 Scores in BRFSS despite high Accuracy (Fig. 10). This is an artifact of the low  $\pi$  (17.4%) and the default 0.5 threshold. The model correctly identifies most negatives (high Accuracy) but, without class re-weighting, yields moderate Precision on the minority positive class. For screening purposes, the high AUC (0.804) confirms the model’s discriminative power; the operating point can be adjusted via threshold tuning to prioritize Recall.

## 7.5 Interpretability and Stability

Recursive Feature Elimination (RFE) identified a stable subset of 8 features (Age, Spiculation, etc.) that maximized the Cost-Effectiveness Index (Fig. 11). This “best8” set performed within 1% of the full 63-feature set but with significantly better cross-center stability. In source-domain evaluation we also show recursive feature elimination curves (Fig. 11) that track AUC/Accuracy/F1 as a function of the retained subset size alongside stability and cost-effectiveness metrics; performance plateaus around 9–13 features, in line with the feature subset used for the final experiments.

# 8 Conclusion

## 8.1 Summary of Contributions

This dissertation introduced PANDA, a framework that connects pre-trained tabular foundation models with the practical constraints of medical tabular data, including small sample sizes, feature heterogeneity, and distribution shifts. Experiments on private cross-hospital cohorts and public benchmarks show that:

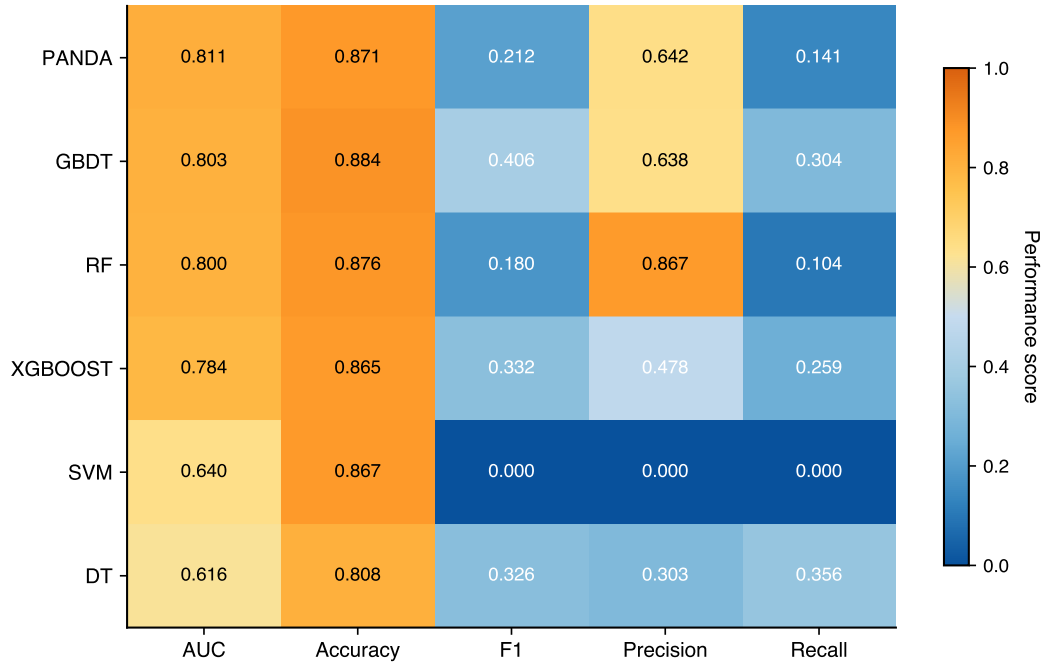
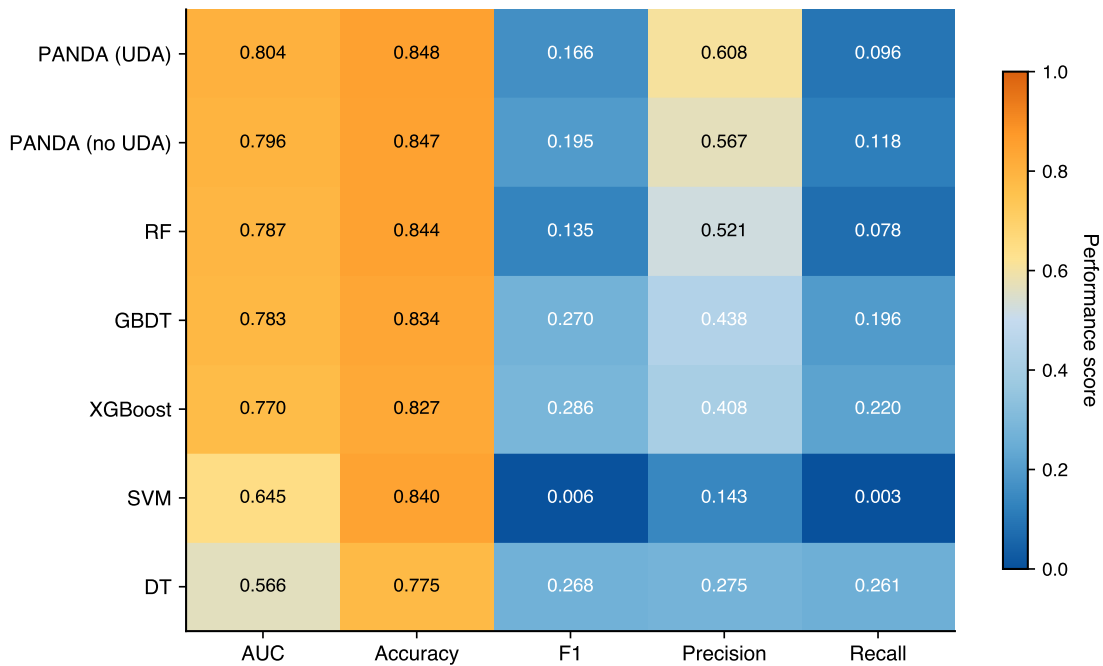
1. **Foundation Models as Robust Priors:** The pre-trained TabPFN backbone substantially outperforms traditional baselines (Random Forest, XGBoost) on small datasets ( $n < 300$ ) by leveraging priors learned from millions of synthetic tasks. This in-context learning capability provides a strong initialization that is inherently more resistant to overfitting than standard empirical risk minimization.
2. **Stability via Selection:** The Cross-Domain Recursive Feature Elimination (RFE) protocol is essential for filtering site-specific artifacts. By converging on a compact set of eight stable predictors, it reduces the dimensionality of the adaptation problem and enables linear alignment methods to succeed where non-linear approaches failed.
3. **Latent Space Alignment:** Transfer Component Analysis (TCA) applied in the Transformer embedding space effectively reduces the Maximum Mean Discrepancy (MMD) between domains. This alignment yields a consistent performance gain (AUC +0.007) and, more importantly, improves calibration in the target domain.

## 8.2 Limitations

Although PANDA advances the state of the art, several limitations remain.

### 8.2.1 Closed-World Assumption

PANDA assumes that the source and target domains share a common feature schema given by their intersection. It does not address open-world shifts in which the target domain introduces entirely new, highly predictive features that are absent in the source. For example, if a new hospital collects a molecular biomarker (such as DNA methylation) that is not available in the training cohort, PANDA cannot exploit this information without retraining. This lowest-common-denominator strategy in feature selection promotes stability but may limit the achievable performance relative to models trained on richer, site-specific schemas.

**a****b**

**Figure 9: Performance comparison across domains.** **a** Source-domain 10-fold CV heatmap over five metrics, showing PANDA's strong AUC, accuracy, and precision. **b** External validation (OOD) heatmap; the TCA-enhanced PANDA model retains the highest AUC and recall, confirming its resilience under race shift.

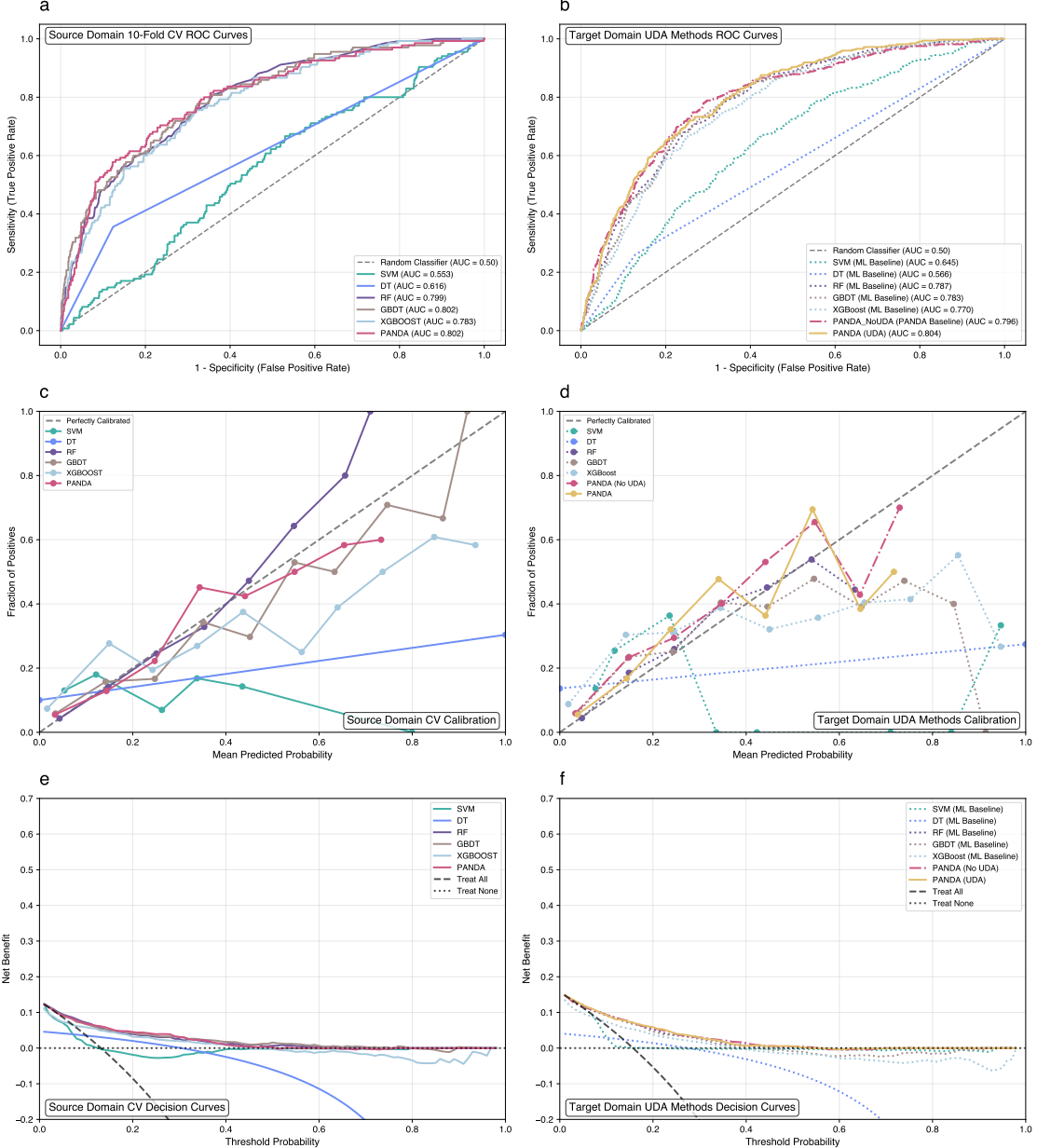
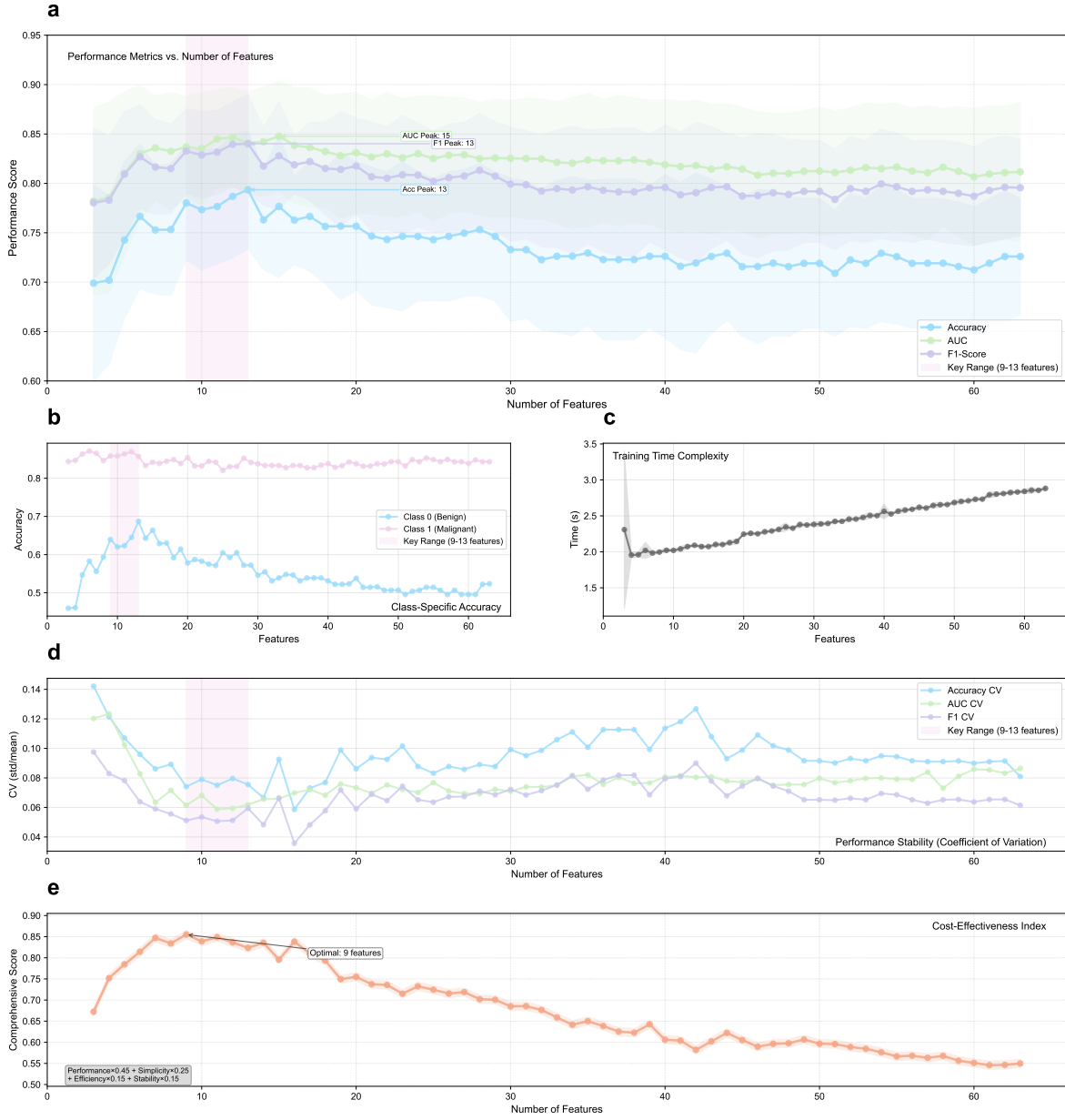


Figure 10: **TableShift BRFSS Diabetes analysis.** **a,b** ROC curves showing PANDA’s robustness. **c,d** Calibration curves. **e,f** Decision curves.



**Figure 11: Comprehensive feature selection and performance analysis using recursive feature elimination (RFE).** (a) AUC, accuracy, and F1 curves as functions of the number of selected features; performance plateaus around 9–13 features, aligning with the preference for simpler models. Shaded regions show variance across 10-fold cross-validation. (b) Class-specific accuracy for malignant and benign cases across subset sizes, illustrating how predictive balance shifts as features are removed. (c) Training-time analysis (seconds per fold) as a function of feature dimensionality, highlighting the computational gain from smaller subsets. (d) Stability assessment using the coefficient of variation across folds; lower values indicate steadier performance. (e) Cost-effectiveness index combining multiple criteria ( $\text{Performance} \times 0.45 + \text{Simplicity} \times 0.25 + \text{Efficiency} \times 0.15 + \text{Stability} \times 0.15$ ) to identify a feature count that balances accuracy with practical deployment considerations.

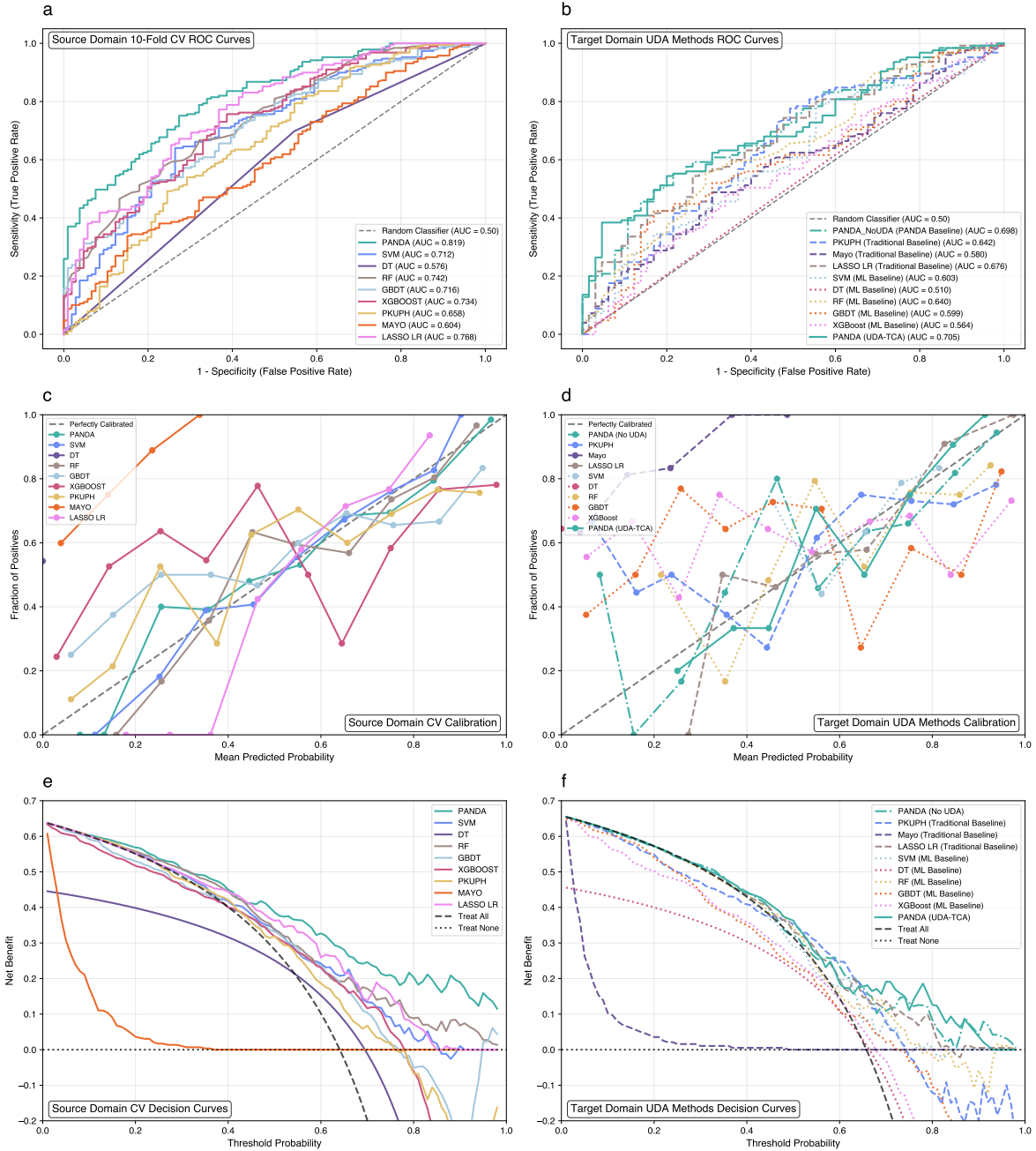


Figure 12: **Performance and utility across source and target domains.** **a,b** ROC curves showing source (Cohort A) vs. external (Cohort B) behavior. **c,d** Calibration plots for the same splits. **e,f** Decision curves highlighting the net clinical benefit of PANDA and its TCA extension.

### 8.2.2 Missing Data Mechanisms

The current approach assumes that missing values are either Missing Completely At Random (MCAR) or Missing At Random (MAR). The `best8` feature set was selected partly for its high completeness. However, in clinical practice data are often Missing Not At Random (MNAR); for instance, a test may not be ordered because the clinician believes that the patient is either too healthy or too sick. PANDA’s current imputation strategies (mean, median, and contextual imputation) do not explicitly model such informative missingness and may therefore introduce bias.

### 8.2.3 Computational Resource Requirements

In contrast to decision trees, which can run on embedded central processing units, TabPFN requires a graphical processing unit for efficient inference (approximately 20 ms per patient). While this cost is negligible for a cloud-based service, it creates a barrier to deployment on edge devices, such as older hospital workstations without dedicated hardware acceleration. The  $O(N^2)$  complexity of the Transformer attention mechanism also limits the context size and necessitates subsampling strategies for larger datasets such as BRFSS.

## 8.3 Future Directions

### 8.3.1 Federated Domain Adaptation

Privacy regulations (such as GDPR and HIPAA) often prevent the centralization of medical data. A natural extension of PANDA is federated domain adaptation, in which the feature extractor (TabPFN) remains frozen and shared, while the alignment matrix (TCA) is learned through secure multi-party computation. Because TCA only requires second-order statistics (covariance matrices), participating hospitals can aggregate these sufficient statistics without sharing patient-level records.

### 8.3.2 Multimodal Integration

Pulmonary nodule diagnosis inherently combines imaging (computed tomography scans) with clinical data. Future work should investigate a multimodal variant of PANDA that aligns tabular embeddings from TabPFN with visual embeddings from a convolutional neural network or Vision Transformer. A cross-attention mechanism could then weight the relative contributions of clinical history and radiological appearance in a domain-aware manner, placing greater emphasis on the modality that remains stable when the other is affected by artifacts.

### 8.3.3 Continual Learning for Temporal Drift

The BRFSS analysis indicated that model performance degrades over time (2015 → 2022) as populations and coding standards evolve. Extending PANDA to a continual learning setting, in which the alignment matrix  $\mathbf{W}$  is updated incrementally as new data arrive (online TCA), would allow the system to adapt to temporal drift while avoiding catastrophic forgetting of the original source knowledge.

## 8.4 Final Remarks

The deployment gap in medical AI seldom arises from a lack of sophisticated architectures; it is more often caused by a failure to accommodate the noisy and shifted nature of real-world data. PANDA provides a pragmatic blueprint for this challenge: *do not learn everything from scratch, select only what is stable, and align what remains*. By treating pre-trained representations as portable priors and statistical alignment as a safety mechanism, this framework moves the field closer to reliable cross-institutional AI systems that can safely scale beyond their initial training sites.

## Acknowledgements

I thank the clinical teams at the participating hospitals for sharing de-identified data and domain expertise, my advisor Wenqi Fan for steady guidance, and Bobo for patient and practical advice. Any remaining mistakes are mine.

## References

- [1] Stephen J. Swensen, Michael D. Silverstein, Duane M. Ilstrup, Charles D. Schleck, and Eric S. Edell. The probability of malignancy in solitary pulmonary nodules: application to clinical practice. *Chest*, 111(3):228–234, 1997.
- [2] Annette McWilliams, Martin C. Tammemagi, John R. Mayo, Hilary Roberts, Guorong Liu, Kian Soghrati, Kazuhiro Yasufuku, Stephen Martel, Francois Laberge, Marie Gingras, Koren Atsu, Nicolas Pastis, Karen Hett, Tapan Sejpal, Timothy Stewart, Ming-Sound Tsao, and James Goffin. Probability of malignancy in pulmonary nodules detected on first screening ct. *New England Journal of Medicine*, 369(10):910–919, 2013.
- [3] Yun Li, Ke-Zhong Chen, and Jun Wang. Development and validation of a clinical prediction model to estimate the probability of malignancy in solitary pulmonary nodules in chinese people. *Clinical lung cancer*, 12(5):313–319, 2011.
- [4] Xia He, Ning Xue, Xiaohua Liu, Xuemiao Tang, Songguo Peng, Yuanye Qu, Lina Jiang, Qingxia Xu, Wanli Liu, and Shulin Chen. A novel clinical model for predicting malignancy of solitary pulmonary nodules: a multicenter study in chinese population. *Cancer cell international*, 21(1):115, 2021.
- [5] Noemi Garau, Chiara Paganelli, Paul Summers, Wookjin Choi, Sadegh Alam, Wei Lu, Cristiana Fanciullo, Massimo Bellomi, Guido Baroni, and Cristiano Rampinelli. External validation of radiomics-based predictive models in low-dose CT screening for early lung cancer diagnosis. *47(9):4125–4136*.
- [6] Kai Zhang, Zihan Wei, Yuntao Nie, Haifeng Shen, Xin Wang, Jun Wang, Fan Yang, and Kezhong Chen. Comprehensive analysis of clinical logistic and machine learning-based models for the evaluation of pulmonary nodules. *3(4):100299*.
- [7] Qiao Liu, Xue Lv, Daiquan Zhou, Na Yu, Yuqin Hong, and Yan Zeng. Establishment and validation of multiclassification prediction models for pulmonary nodules based on machine learning. *18(5):e13769*.
- [8] Tianqi Chen and Carlos Guestrin. Xgboost: A scalable tree boosting system. In *Proceedings of the 22nd acm sigkdd international conference on knowledge discovery and data mining*, pages 785–794, 2016.
- [9] Yury Gorishniy, Ivan Rubachev, Valentin Khrulkov, and Artem Babenko. Revisiting deep learning models for tabular data. *Advances in neural information processing systems*, 34:18932–18943, 2021.
- [10] Carlos J Hellín, Alvaro A Olmedo, Adrián Valledor, Josefa Gómez, Miguel López-Benítez, and Abdelhamid Tayebi. Unraveling the impact of class imbalance on deep-learning models for medical image classification. *Applied Sciences*, 14(8):3419, 2024.
- [11] Sercan O. Arik and Tomas Pfister. Tabnet: Attentive interpretable tabular learning. In *Proceedings of the AAAI Conference on Artificial Intelligence*, volume 35, pages 6679–6687, 2021.
- [12] Xin Huang, Ashish Khetan, Milan Cvitkovic, and Zohar Karnin. Tabtransformer: Tabular data modeling using contextual embeddings. In *Advances in Neural Information Processing Systems*, volume 33, pages 14914–14925, 2020.
- [13] Gowthami Somepalli, Micah Goldblum, Avi Schwarzschild, C Bayan Bruss, and Tom Goldstein. Saint: Improved neural networks for tabular data via row attention and contrastive pre-training. *arXiv preprint arXiv:2106.01342*, 2021.
- [14] Vitaly Borisov, Thomas Leemann, Pierre Selegue, Riccardo Miotto, Mario May, and Andreas Züfle. Deep neural networks and tabular data: A survey. *IEEE Transactions on Neural Networks and Learning Systems*, 33(9):4472–4492, 2022.

- [15] Noah Hollmann, Samuel Müller, Lennart Purucker, Arjun Krishnakumar, Max Körfer, Shi Bin Hoo, Robin Tibor Schirrmeister, and Frank Hutter. Accurate predictions on small data with a tabular foundation model. *Nature*, 637(8045):319–326, 2025.
- [16] Prior labs.
- [17] A closer look at TabPFN v2: Strength, limitation, and extension.
- [18] Realistic evaluation of TabPFN v2 in open environments.
- [19] automl/drift-resilient\_tabPFN. original-date: 2024-10-22T17:32:11Z.
- [20] Dmitry Eremeev, Gleb Bazhenov, Oleg Platonov, Artem Babenko, and Liudmila Prokhorenkova. Turning tabular foundation models into graph foundation models.
- [21] Johannes Schneider, Christian Meske, and Pauline Kuss. Foundation models: A new paradigm for artificial intelligence. *Business & Information Systems Engineering*, 66(2):221–231, 2024.
- [22] Hao Guan and Mingxia Liu. Domain adaptation for medical image analysis: a survey. *IEEE Transactions on Biomedical Engineering*, 69(3):1173–1185, 2021.
- [23] Aminu Musa, Rajesh Prasad, and Monica Hernandez. Addressing cross-population domain shift in chest x-ray classification through supervised adversarial domain adaptation. *Scientific Reports*, 15(1):11383, 2025.
- [24] Lisa M Koch, Christian F Baumgartner, and Philipp Berens. Distribution shift detection for the postmarket surveillance of medical ai algorithms: a retrospective simulation study. *NPJ Digital Medicine*, 7(1):120, 2024.
- [25] Lin Lawrence Guo, Stephen R. Pfohl, Jason Fries, Alistair E. W. Johnson, Jose Posada, Catherine Aftandilian, Nigam Shah, and Lillian Sung. Evaluation of domain generalization and adaptation on improving model robustness to temporal dataset shift in clinical medicine. 12(1):2726.
- [26] Seyedmehdi Orouji, Martin C. Liu, Tal Korem, and Megan A. K. Peters. Domain adaptation in small-scale and heterogeneous biological datasets. 10(51):eadp6040.
- [27] Josh Gardner, Zoran Popovic, and Ludwig Schmidt. Benchmarking distribution shift in tabular data with TableShift.
- [28] Seong-Ho Ahn, Seeun Kim, and Dong-Hwa Jeong. Unsupervised domain adaptation for mitigating sensor variability and interspecies heterogeneity in animal activity recognition. 13(20):3276.
- [29] Diego Ardila, Atilla P. Kiraly, Sujeeth Bharadwaj, Bokyung Choi, Joshua J. Reicher, Lily Peng, Daniel Tse, Mozziyar Etemadi, Wenxing Ye, Greg Corrado, David P. Naidich, and Shravya Shetty. End-to-end lung cancer screening with three-dimensional deep learning on low-dose chest computed tomography. 25(6):954–961.
- [30] John R. Zech, Marcus A. Badgeley, Manway Liu, Anthony B. Costa, Joseph J. Titano, and Eric Karl Oermann. Variable generalization performance of a deep learning model to detect pneumonia in chest radiographs: A cross-sectional study. 15(11):e1002683. Publisher: Public Library of Science.
- [31] Feng Sun, Hanrui Wu, Zhihang Luo, Wenwen Gu, Yuguang Yan, and Qing Du. Informative feature selection for domain adaptation. *IEEE Access*, 7:142551–142563, 2019.
- [32] Sinno Jialin Pan, Ivor W Tsang, James T Kwok, and Qiang Yang. Domain adaptation via transfer component analysis. *IEEE transactions on neural networks*, 22(2):199–210, 2010.
- [33] Rishi Bommasani, Drew A. Hudson, Ehsan Adeli, and et al. On the opportunities and risks of foundation models. *arXiv preprint arXiv:2108.07258*, 2021.
- [34] Léo Grinsztajn, Edouard Oyallon, and Gaël Varoquaux. Why do tree-based models still outperform deep learning on tabular data?

- [35] Assaf Shmuel, Oren Glickman, and Teddy Lazebnik. A comprehensive benchmark of machine and deep learning across diverse tabular datasets.
- [36] Yuhua Fan and Patrik Waldmann. Tabular deep learning: a comparative study applied to multi-task genome-wide prediction. 25:322.
- [37] Vadim Borisov, Tobias Leemann, Kathrin Seßler, Johannes Haug, Martin Pawelczyk, and Gjergji Kasneci. Deep neural networks and tabular data: A survey. 35(6):7499–7519.
- [38] Si-Yang Liu and Han-Jia Ye. TabPFN unleashed: A scalable and effective solution to tabular classification problems. version: 1.
- [39] Xin Huang, Ashish Khetan, Milan Cvitkovic, and Zohar Karnin. TabTransformer: Tabular data modeling using contextual embeddings.
- [40] Yury Gorishniy, Ivan Rubachev, Valentin Khrulkov, and Artem Babenko. Revisiting deep learning models for tabular data. version: 2.
- [41] Andrei Margeloiu, Nikola Simidjevski, Pietro Lio, and Mateja Jamnik. Weight predictor network with feature selection for small sample tabular biomedical data. In *Proceedings of the AAAI conference on artificial intelligence*, volume 37, pages 9081–9089, 2023.
- [42] Wei Min Loh, Jiaqi Shang, and Pascal Poupart. Basis transformers for multi-task tabular regression.
- [43] Arash Khoeini. FTTransformer: Transformer architecture for tabular datasets.
- [44] Bytez.com, Jingang QU, David Holzmüller, Gaël Varoquaux, and Marine Le Morvan. TabICL: A tabular foundation model for in-context learni...
- [45] Shriyank Somvanshi, Subasish Das, Syed Aaqib Javed, Gian Antariksa, and Ahmed Hossain. A survey on deep tabular learning. *arXiv preprint arXiv:2410.12034*, 2024.
- [46] Weijieying Ren, Tianxiang Zhao, Yuqing Huang, and Vasant Honavar. Deep learning within tabular data: Foundations, challenges, advances and future directions. version: 1.
- [47] Noah Hollmann, Samuel Müller, Lennart Purucker, Arjun Krishnakumar, Max Körfer, Shi Bin Hoo, Robin Tibor Schirrmeister, and Frank Hutter. Accurate predictions on small data with a tabular foundation model. 637(8045):319–326. Publisher: Nature Publishing Group.
- [48] Kai Helli, David Schnurr, Noah Hollmann, Samuel Müller, and Frank Hutter. Drift-resilient TabPFN: In-context learning temporal distribution shifts on tabular data.
- [49] Woruo Chen, Yao Tian, Youchao Deng, Dejun Jiang, and Dongsheng Cao. TabPFN opens new avenues for small-data tabular learning in drug discovery.
- [50] Tianzhu Liu, Huanjun Wang, Yan Guo, Yongsong Ye, Bei Weng, Xiaodan Li, Jun Chen, Shanghuang Xie, Guimian Zhong, Zhixuan Song, and Lesheng Huang. Tabular prior-data fitted network in real-world CT radiomics: benign vs. malignant renal tumor classification. 15(11):10847–10861.
- [51] Tom Brown, Benjamin Mann, Nick Ryder, Melanie Subbiah, Jared D Kaplan, Prafulla Dhariwal, Arvind Neelakantan, Pranav Shyam, Girish Sastry, Amanda Askell, et al. Language models are few-shot learners. *Advances in neural information processing systems*, 33:1877–1901, 2020.
- [52] Mayuka Jayawardhana, Renbo Tu, Samuel Dooley, Valeria Cherepanova, Andrew Gordon Wilson, Frank Hutter, Colin White, Tom Goldstein, and Micah Goldblum. Transformers boost the performance of decision trees on tabular data across sample sizes. version: 1.
- [53] Summer Zhou, Vinayak Agarwal, Ashwin Gopinath, and Timothy Kassis. The limitations of TabPFN for high-dimensional RNA-seq analysis. ISSN: 2692-8205 Pages: 2025.08.15.670537 Section: New Results.

- [54] (PDF) comparative analysis of tree-based models and deep learning architectures for tabular data: Performance disparities and underlying factors. In *ResearchGate*.
- [55] Sergey Kolesnikov. Wild-tab: A benchmark for out-of-distribution generalization in tabular regression.
- [56] Baochen Sun, Jiashi Feng, and Kate Saenko. Correlation alignment for unsupervised domain adaptation, 2016.
- [57] Thomas Grubinger, Adriana Birlutiu, Holger Schöner, Thomas Natschläger, and Tom Heskes. Domain generalization based on transfer component analysis. In *International work-conference on artificial neural networks*, pages 325–334. Springer, 2015.
- [58] Tianran Zhang, Muhan Chen, and Alex A. T. Bui. AdaDiag: Adversarial domain adaptation of diagnostic prediction with clinical event sequences. 134:104168.
- [59] Wanxin Li, Yongjin P. Park, and Khanh Dao Duc. Transport-based transfer learning on electronic health records: Application to detection of treatment disparities. Pages: 2024.03.27.24304781.
- [60] Tianyu Luo, Zhongying Zhang, and James Kwok. Informative feature selection for domain adaptation. Technical report, The Hong Kong University of Science and Technology, 2021.
- [61] Thai-Hoang Pham, Yuanlong Wang, Changchang Yin, Xueru Zhang, and Ping Zhang. Open-set heterogeneous domain adaptation: Theoretical analysis and algorithm. 39(19):19895–19903.
- [62] Hao Guan and Mingxia Liu. DomainATM: Domain adaptation toolbox for medical data analysis. 268:119863.
- [63] Hao Guan and Mingxia Liu. Domain adaptation for medical image analysis: A survey. 69(3):1173–1185.
- [64] Helen Zhou, Sivaraman Balakrishnan, and Zachary C. Lipton. Domain adaptation under missingness shift.
- [65] Tyrel Stokes, Hyungrok Do, Saul Blecker, Rumi Chunara, and Samrachana Adhikari. Domain adaptation under MNAR missingness. version: 1.
- [66] Chunmei He, Lanqing Zheng, Taifeng Tan, Xianjun Fan, and Zhengchun Ye. Multi-attention representation network partial domain adaptation for COVID-19 diagnosis. 125:109205.
- [67] mlfoundations/tableshift: A benchmark for distribution shift in tabular data.
- [68] Josh Gardner. TableShift.
- [69] A multi-center study on the adaptability of a shared foundation model for electronic health records | npj digital medicine.
- [70] Muhammad Habib ur Rehman, Walter Hugo Lopez Pinaya, Parashkev Nachev, James T. Teo, Sebastin Ourselin, and M. Jorge Cardoso. Federated learning for medical imaging radiology. 96(1150):20220890.
- [71] Hao Guan, Pew-Thian Yap, Andrea Bozoki, and Mingxia Liu. Federated learning for medical image analysis: A survey. 151:110424.
- [72] Ferdinand Kahenga, Antoine Bagula, Patrick Sello, and Sajal K. Das. FedFusion: Federated learning with diversity- and cluster-aware encoders for robust adaptation under label scarcity.
- [73] Isabelle Guyon, Jason Weston, Stephen Barnhill, and Vladimir Vapnik. Gene selection for cancer classification using support vector machines. *Machine learning*, 46(1):389–422, 2002.
- [74] Xinye Chen, Yue Wu, Lichao He, Jiayu Zhai, Xiang Li, and Xiangjun Li. Graph convolutional network-based feature selection for high-dimensional and low-sample size data. *Bioinformatics*, 39(1):btac834, 2023.

- [75] Xiaoqian Liu, Dandan Wu, Weixin Cao, and Jianwen Cai. Deep feature screening: Feature selection for ultra high-dimensional data via deep neural networks. *Neurocomputing*, 488:36–47, 2022.
- [76] Kexuan Li, Fangfang Wang, Lingli Yang, and Ruiqi Liu. Deep feature screening: Feature selection for ultra high-dimensional data via deep neural networks. *Neurocomputing*, 538:126186, 2023.
- [77] Stephen J Swensen, Marc D Silverstein, Duane M Ilstrup, Cathy D Schleck, and Eric S Edell. The probability of malignancy in solitary pulmonary nodules: application to small radiologically indeterminate nodules. *Archives of Internal Medicine*, 157(8):849–855, 1997.
- [78] S. Chen, W. L. Lin, W. T. Liu, L. Y. Zou, Y. Chen, and F. Lu. Pulmonary nodule malignancy probability: a meta-analysis of the brock model. 82:106788.
- [79] Bumhee Yang, Byung Woo Jhun, Sun Hye Shin, Byeong-Ho Jeong, Sang-Won Um, Jae Il Zo, Ho Yun Lee, Insoek Sohn, Hojoong Kim, O. Jung Kwon, and Kyungjong Lee. Comparison of four models predicting the malignancy of pulmonary nodules: A single-center study of korean adults. 13(7):e0201242. Publisher: Public Library of Science.
- [80] Xiaonan Cui, Marjolein A. Heuvelmans, Daiwei Han, Yingru Zhao, Shuxuan Fan, Sunyi Zheng, Grigory Sidorenkov, Harry J. M. Groen, Monique D. Dorrius, Matthijs Oudkerk, Geertruida H. de Bock, Rozemarijn Vliegenthart, and Zhaoxiang Ye. Comparison of veterans affairs, mayo, brock classification models and radiologist diagnosis for classifying the malignancy of pulmonary nodules in chinese clinical population. 8(5). Publisher: AME Publishing Company.
- [81] You Li, Hui Hu, Ziwei Wu, Ge Yan, Tangwei Wu, Shuiyi Liu, Weiqun Chen, and Zhongxin Lu. Evaluation of models for predicting the probability of malignancy in patients with pulmonary nodules. 40(2):BSR20193875.
- [82] Gerarda J. Herder, Harm van Tinteren, Richard P. Golding, Piet J. Kostense, Emile F. Comans, Egbert F. Smit, and Otto S. Hoekstra. Clinical prediction model to characterize pulmonary nodules: validation and added value of 18f-fluorodeoxyglucose positron emission tomography. 128(4):2490–2496.
- [83] Simone Perandini, Gian Alberto Soardi, Massimiliano Motton, Arianna Rossi, Manuel Signorini, and Stefania Montemezzi. Solid pulmonary nodule risk assessment and decision analysis: comparison of four prediction models in 285 cases. 26(9):3071–3076.
- [84] Shulong Li, Panpan Xu, Bin Li, Liyuan Chen, Zhiguo Zhou, Hongxia Hao, Yingying Duan, Michael Folkert, Jianhua Ma, Shiying Huang, Steve Jiang, and Jing Wang. Predicting lung nodule malignancies by combining deep convolutional neural network and handcrafted features. 64(17):175012.
- [85] Chia-Ying Lin, Shu-Mei Guo, Jenn-Jier James Lien, Wen-Tsen Lin, Yi-Sheng Liu, Chao-Han Lai, I-Lin Hsu, Chao-Chun Chang, and Yau-Lin Tseng. Combined model integrating deep learning, radiomics, and clinical data to classify lung nodules at chest CT. 129(1):56–69.
- [86] Jason L. Causey, Junyu Zhang, Shiqian Ma, Bo Jiang, Jake A. Qualls, David G. Politte, Fred Prior, Shuzhong Zhang, and Xiuzhen Huang. Highly accurate model for prediction of lung nodule malignancy with CT scans. 8(1):9286. Publisher: Nature Publishing Group.